The Diffuse Supernova Neutrino Background

Diplomarbeit
von

Clemens Kießig

März 2005

TECHNISCHE
UNIVERSITÄT
MÜNCHEN

PHYSIK-DEPARTMENT

MAX-PLANCK-GESELLSCHAFT

Abstract

We study the diffuse supernova neutrino background (DSNB), in particular the $\bar{\nu}_e$-part in view of its detectability. We parameterize the *individual* supernova (SN) $\bar{\nu}_e$ spectrum *after* flavor oscillation in the SN envelope and the SN history by three parameters each. These are the total energy $E_{\rm tot}^{\rm SN}$, the mean energy $\overline{E}_{\rm SN}$ and the spectral pinching $a_{\rm SN}$ as effective parameters after oscillation, as well as the local SN rate $R_{\rm SN}^0$, the recent SN history β and the early SN history α. We adopt a baseline case for each of these parameters and study the influence of variations of the parameters, allowing rather extreme cases, which are, however, not excluded by observations. We fit the DSNB to an analytic function with three parameters. Moreover, we find that the dependence of these fit parameters on the six input parameters can be described with second-order polynomials to reasonable accuracy. We discuss the detectability at water Cherenkov detectors such as Super-Kamiokande (SK), taking into account backgrounds and the possible reduction of some backgrounds by the gadolinium trichloride ($GdCl_3$) detection technique. We find that a detection of the DSNB will only tell us about the total DSNB flux $F_{\rm tot}$ and the mean energy of the DSNB $\overline{E}$, but not about the spectral pinching a. We analyze the possible extraction of the *individual* SN neutrino spectra and the SN history by the DSNB detection. We find that $F_{\rm tot}$ can tell us about the degenerate parameters $R_{\rm SN}^0$, $E_{\rm tot}^{\rm SN}$ and β and that $\overline{E}$ can be directly related to $\overline{E}_{\rm SN}$. Moreover, we conclude that we cannnot determine $a_{\rm SN}$ and α from the DSNB.

Contents

Chapter 1

Introduction

The field of neutrino physics has received enormous attention in the last few years due to the discovery of neutrino oscillations and the neutrino mass by solar, atmospheric and reactor neutrino observations [1]. However, the most luminous neutrino sources of the universe are the death throes of very massive stars which end their lives in a core-collapse supernova[1] (SN), emitting about 3×10^{53} erg in neutrinos within a few seconds. In 1987, a handful of neutrinos from such an event has been detected for the first and only time [2, 3], leading to an enormous amount of analyses and conclusions both on neutrino properties, SN characteristics and general physics theories, going as far as probing the invariance of gravity under charge conjugation, to name just one example. Detectors were able to measure around 20 neutrino events from SN 1987A. Since that time, physicists have been waiting for a new SN in our galaxy, to obtain far more statistics with present-day detectors. Around 10,000 neutrino events are expected from such a SN in a detector like Super-Kamiokande (SK) and a variety of neutrino and SN properties could be determined. However, it is unclear how often these spectacular explosions occur in our vicinity. Estimates range from frequencies of one in 20 to one in 100 years.

Alternatively, it has been suggested that we might be able to detect neutrinos from SNe that occur much farther away, by detecting the superposition of the neutrino fluxes of all SNe in the universe [4, 5, 6, 7]. It has been recognized that there should be an energy window around 10–40 MeV where the neutrinos from this diffuse supernova neutrino background[2] (DSNB) dominate over all other sources and that sufficient detector efficiency should lead to a successful detection of this flux in the future.

The advantage of detecting the DSNB is not only that we would not have

[1]With supernova, we will always mean core-collapse supernova, if not noted otherwise.

[2]This flux is often referred to as *supernova relic neutrinos* in the literature. However, to avoid confusion with the *relic neutrino background* from the big bang, we prefer the more appropriate term "diffuse supernova neutrino background".

to wait for an uncertain time in order to gain data about SN neutrinos. The DSNB can also act as a probe of different physics to which a galactic SN signal would have no access. Since these neutrinos travel large distances, and essentially do not interact on their way to earth, they could provide a unique tool to probe physics and physical processes at the distances and redshifts of their origin. This makes them complementary to electromagnetic radiation which is much easier to detect, but also much easier to be absorbed or scattered on its way, providing a "smeared" image of the universe.

It has been stressed that one of the most interesting conclusions might be the evolution of the SN rate in the past, which again is closely related to the rate of star formation, a field that has attracted much attention in astrophysics ever since the presentation of a star-formation history up to very high redshifts by Madau et al. in 1996 [8]. Additionally, neutrino properties such as the lifetime of the neutrino and therefore neutrino decay scenarios could be analyzed and constrained [9].

There has been a considerable amount of literature on the DSNB with varying models and predictions, going as far as suggesting that the DSNB might already have been detected [10]. Two experiments have reported upper bounds on the DSNB, the Kamiokande Collaboration in 1988 [11], obtaining an upper limit of 226 $\bar{\nu}_e$ cm^{-2} s^{-1} above 19.3 MeV and recently the SK Collaboration, which reported an upper limit of 1.2 $\bar{\nu}_e$ cm^{-2} s^{-1} in the same energy region [12]. The latter result has revived interest in the DSNB, because it is close to most predictions of the DSNB and has actually excluded one of them. Thus we have good reason to hope that we might be able to detect this flux in the foreseeable future.

However, problems in the detection are not only due to detector sensitivity, but most importantly to background events from various sources. Notably these come from cosmic-ray muons, which hinder detection in such a way that there is currently no accessible energy window at all [7]. Recently and partly inspired by these difficulties, a new detection technique has been proposed by Beacom and Vagins [13], which uses Gadolinium Trichloride ($GdCl_3$) as a neutron absorber in order to identify electron antineutrinos via inverse beta-decay ($\bar{\nu}_e p \to n e^+$) with a coincident neutron detection. This would dramatically reduce the muon-induced background.

Models predicting the DSNB typically use input from simulations of neutrino spectra that exit SNe as well as from observations of the star-formation rate (SFR), which can be converted to a SN rate. However, these input parameters are themselves not very well constrained and thus predictions of the DSNB differ by up to one order of magnitude. This might prove to be a problem in interpreting the results of the DSNB in future, since the constraints which we can put on one parameter or its determination depend crucially on priors on other parameters. Thus, the analysis of a possible DSNB signal will be a difficult project.

Therefore it seems desirable to develop some analytic or semi-analytic tool with which we could specify in detail the influence of each input parameter and which will help us extract information about these parameters from the DSNB. This work aims at providing such a novel tool, using input parameters from representative works on SN simulations as well as SN and star-formation observations. For each of the two input disciplines, we choose one parameterization model and review the literature on possible choices of the corresponding parameters. We adopt a baseline case for each parameter and analyze an upper and a lower case, which are chosen not as tight as in the previous literature, but rather generously. However, our extreme cases are not excluded by experiments and in some cases even supported by observations. As an important step of our analysis we fit the resulting flux spectra to an analytic function, always taking into consideration the situation at the detector. This means that we actually fit to the event rate of the detector and that we only fit in the energy window that can become an actual detection window.

This thesis is structured as follows. In chapter 2 we derive the general expression of the DSNB and choose a cosmological model for our analysis. In chapter 3 we explain the difference between core-collapse SNe and type Ia SNe and review their explosion mechanism. We choose a parameterization model for the individual SN neutrino spectra and review the findings of different simulations. We choose our parameter ranges according to the literature, emphasizing the new picture that has emerged following the novel treatment of ν_μ- and ν_τ-transport inside the SN core by the Garching group [14, 15]. We apply these findings to neutrino oscillations. Moreover, we take into account the only observation of SN neutrino spectra that we have to date, SN 1987A. In chapter 4, we review measurements of the SN rate, including for the first time some recent results on high redshift rates by Dahlen et al. [16]. We discuss tracers of the SFR and review measurements thereof. We choose a SN rate model and adopt parameter ranges that take into account extreme cases. We emphasize the impact of direct SN observations for the determination of the local SN rate and the uncertainties connected to the conversion of a SFR to an SN rate. In chapter 5, we present flux calculations and fit the DSNB to an analytic function. In chapter 6 we discuss the possibility to measure the DSNB with different detectors. In chapter 7 we review the different detector backgrounds. We present a precise treatment of the high-energy flux from reactor neutrinos, which are an important background for future $GdCl_3$ detectors. In chapter 8 we discuss the results of our work. We analyze in detail the impact of different parameters on the DSNB which has been done for the SFR before, but not for the SN neutrino spectra and find that some previous conclusions will be altered, notably because of degenerate parameters (e.g. the local SN rate and the total neutrino luminosity). We discuss the possibility to put constraints on the magnetic moment of the neutrino by the already existing observations and by a future detection. We conclude this work with a summary in chapter 9, where we also give an outlook of possible combinations of future DSNB data with other observations.

Throughout this text, we will use natural units with $\hbar = c = k_{\mathrm{B}} = 1$. Moreover, we will always neglect neutrino masses, except in the context of flavor oscillations, and assume that neutrinos travel with the speed of light.

Chapter 2

General Expression

2.1 Derivation

In order to derive a general expression for the DSNB, the continuous flux that we receive from all past SNe, we start with the energy flux (given in energy per unit area and time) that we would receive from a hypothetical source emitting neutrinos of a single energy [17],

$$\mathcal{F} = \frac{\mathcal{L}}{4\pi R^2(t_0) r_1^2 (1+z)^2}. \tag{2.1}$$

Here, $R(t)$ is the cosmic scale factor, earth is at comoving coordinate $r = 0$ and time t_0, $\mathcal{L}$ is the luminosity of the source at comoving coordinate r_1 and z= $R(t_0)/R(t_1)$ is its redshift. The coordinate system is defined by the Robertson-Walker metric [17, 18]

$$ds^2 = dt^2 - R^2(t) \left\{ \frac{dr^2}{1-kr^2} + r^2 d\theta^2 + r^2 \sin^2\theta d\phi^2 \right\}, \tag{2.2}$$

where (t, r, θ, ϕ) are comoving coordinates and k is the curvature. In this framework, Eq. (2.1) follows from covariant energy conservation $T^{\mu\nu}{}_{;\nu} = 0$. However, it can be understood in an intuitive way. The initial energy of the neutrinos E_1 is redshifted to

$$E_0 = \frac{E_1}{1+z}, \tag{2.3}$$

thus, one factor $(1 + z)$ in the denominator results from the redshift of the energy. The other factor comes from the fact that the time interval dt between the detection of two neutrinos increases with respect to the time interval at the time of emission, again because of cosmic redshift.

In the following, however, we will not be interested in the energy flux $\mathcal{F}$, but rather in the number flux

$$F = \frac{\mathcal{F}}{E_0} = \frac{n}{4\pi R^2(t_0) r_1^2 (1+z)}. \tag{2.4}$$

Here, n is the particle emission rate of the source,

$$n = \frac{\mathcal{L}}{E_1}. \tag{2.5}$$

In the case of a continuous spectrum, it is more convenient to deal with the differential number flux,

$$\Phi(E_0) = \frac{dF(E_0)}{dE_0} = \frac{dn(E_1)}{dE_1}\frac{1}{4\pi R^2(t_0)r_1^2} = \frac{n'(E_1)}{4\pi R^2(t_0)r_1^2}, \tag{2.6}$$

where $n' = dn/dE_1$ is the differential particle emission rate.

If we take the sources to be SNe and single out a distance interval (r_1, $r_1 + dr_1$) and the corresponding time interval (t_1, $t_1 + dt_1$), then the number of SNe in this volume and time interval is

$$dV\,dt R_{\rm SN}^{\rm phys}(t_1) = dV\,dt R_{\rm SN}^{\rm com}(t_1)(1+z)^3, \tag{2.7}$$

where $R_{\rm SN}^{\rm phys}$ is the SN rate per time and volume in physical coordinates. It is often convenient to define the SN rate in SN per unit time and mass. The definition per mass is not proportional to the SN rate per physical volume but rather to an SN rate per comoving volume $R_{\rm SN}^{\rm com}$, given in units of present-day volume. In this case, the SN rate $R_{\rm SN}^{\rm com}(z)$ scales as $(1+z)^{-3}$. Henceforth, $R_{\rm SN}$ will from now on always denote $R_{\rm SN}^{\rm com}$. The volume element is

$$dV = 4\pi[R(t_1)r_1]^2\frac{R(t_1)dr}{\sqrt{1-kr^2}} = 4\pi R^2(t_1)r_1^2 dt. \tag{2.8}$$

It follows that

$$\begin{aligned}\Phi(E_0) &= n'(E_1)\frac{1}{4\pi R^2(t_0)r_1^2}4\pi R^2(t_1)r_1^2 dt^2 R_{\rm SN}(z)(z+1)^3 \\ &= N'(E_1)(z+1)R_{\rm SN}(z)\frac{dt}{dz}dz, \end{aligned}\tag{2.9}$$

where N is the total number of neutrinos emitted in the SN explosion and $N' = dN/dE$ is the differential neutrino number.

To obtain a general expression for all cosmological models, we have to take into account matter with an equation of state $p_{\rm m} = 0$, radiation with $p_{\rm r} = \frac{1}{3}\rho_{\rm r}$, vacuum energy with $p_\Lambda = -\rho_\Lambda$ and the curvature k, where p_i is the pressure of the corresponding component and ρ_i its energy density. The Friedmann equation yields

$$\left(\frac{dt}{dz}\right)^{-1} = -H_0(z+1)\sqrt{(z+1)^3\Omega_{\rm m} + (z+1)^4\Omega_{\rm r} + \Omega_\Lambda + (z+1)^2(1-\Omega_{\rm tot})}, \tag{2.10}$$

where $\Omega_i = \rho_i(t_0)/\rho_{\text{crit}}(t_0)$ is the present mass fraction of the matter component $i = m,\ r,\ \Lambda$ in terms of the critical density $\rho_{\text{crit}}(t_0) = 3H_0^2/8\pi G$, $\Omega_{\text{tot}} = \Omega_{\text{m}} + \Omega_{\text{r}} + \Omega_\Lambda$ is the total energy content of the universe and $H_0 = \dot{R}(t_0)/R(t_0)$ is the Hubble parameter today.

If we now combine Eqs. (2.9) and (2.10) and integrate over redshift from $z = 0$ to z_{max}, when SN explosions (and also star formation) started, we get

$$\Phi(E_0) = \int_0^{z_{\text{max}}} \frac{N'(E_1) R_{\text{SN}}(z) dz}{H_0 \sqrt{(z+1)^3 \Omega_{\text{m}} + (z+1)^4 \Omega_{\text{r}} + \Omega_\Lambda + (z+1)^2 (1 - \Omega_{\text{tot}})}}. \tag{2.11}$$

The input information that enters Eq. (2.11) are the SN rate, the SN neutrino spectra and the cosmological parameters H_0 and Ω_i.

2.2 Cosmological Parameters

A number of recent observations have constrained the cosmological parameters to such an extent that cosmologists nowadays talk about a "standard cosmological model", or "concordance model". Particularly the Wilkinson Microwave Anisotropy Probe (WMAP) experiment has measured the anisotropies of the Cosmic Microwave Background and determined several cosmological parameters by combining their data with other experiments [19]. By assuming a running spectral index model and including the two other CMB experiments ACBAR [20] and CBI [21], measurements of the 2 degree Field Galaxy Redshift Survey [22, 23] and observations of the Lyman-α forest [24, 25], they determined the best fits of H_0 and Ω_{m} as

$$\begin{aligned} H_0 &= 71^{+0.04}_{-0.03} \text{ km s}^{-1} \text{ Mpc}^{-1}, \\ \Omega_{\text{m}} &= 0.27 \pm 0.04. \end{aligned} \tag{2.12}$$

Using data from SN Ia observations [26, 27] and the HST key project measurements of the Hubble parameter [28], WMAP constrains the geometry of the universe,

$$\Omega_{\text{tot}} = 1.02 \pm 0.02. \tag{2.13}$$

The dark energy equation of state, defined as $w_\Lambda = p_\Lambda/\rho_\Lambda$, is found to be constrained by

$$w_\Lambda < -0.78. \tag{2.14}$$

Based on these results, we will from now on assume

$$\begin{aligned} \Omega_{\text{tot}} &= 1, \\ w &= -1, \\ \Omega_{\text{m}} &= 0.26, \\ \Omega_\Lambda &= \Omega_{\text{tot}} - \Omega_{\text{m}} = 0.74 \end{aligned} \tag{2.15}$$

for our background cosmological model. Star formation is believed to have started somewhere between $z = 100$ and $z = 5$, which is long after radiation dominance (beyond $z = 1000$). Thus we can neglect the radiation content of the universe in our calculations,

$$\Omega_{\mathrm{r}} = 0. \tag{2.16}$$

With these assumptions, Eq. (2.11) reduces to

$$\Phi(E) = \int_0^{z_{\max}} \frac{N'(E(z+1))R_{\mathrm{SN}}(z)dz}{H_0\sqrt{(z+1)^3\Omega_{\mathrm{m}} + \Omega_\Lambda}}, \tag{2.17}$$

our reference espression for the DSNB, where from now on we us E instead of E_0 for the present-day energy measured at earth.

Chapter 3

Individual Supernova Neutrino Spectrum

3.1 Classification of Supernovae

The classification of SNe follows the properties of their spectra. More specifically, the presence of certain emission lines is the defining factor in the categorization of SN observations. The corresponding SN types and emission lines are [29]:

- Type II: hydrogen.
- Type I: no hydrogen.
  - Type Ia: silicon II.
  - Type Ib: no silicon II, helium I.
  - Type Ic: no silicon II, no helium I.

The light curves of type Ia SNe are empirically a one-parameter family and have a universal shape up to a stretch factor [30]. This empirical feature makes them excellent standard candles for determining the distance of their host galaxy. Combined with their redshift, one can learn about the geometry of the universe, since these SNe are observed up to redshift $z = 1$ and even beyond [31, 32]. The light curves of type II as well as type Ib and Ic, however, are not as homogeneous, their maxima and shapes differ widely. While a more detailed description of the different SN types and their spectra and light curves can be found in Ref. [29], we will concentrate on their *explosion mechanism*, which is the most interesting aspect for our purposes.

Type Ia SNe are believed to be connected to the thermo-nuclear explosion of an accreting white dwarf in a binary system [33]. Their neutrino production is large, but orders of magnitude lower than that of core collapse SN. Henceforth type Ia can be neglected for our purposes and do not contribute to the DSNB. Type II SNe, as well as type Ib/c emit enormous amounts of neutrinos during their explosion, around 3×10^{53} erg within a time of a few seconds. They are believed to result from the core-collapse of very massive stars with $M \geq 8M_\odot$. Their explosion mechanism makes them the most luminous neutrino sources of the universe.

3.2 Explosion Mechanism of Core-Collapse Supernovae[1]

Massive stars ($M > 8M_\odot$), after their H and He-burning phase, have a sufficiently high density to ignite carbon and subsequently start burning heavier elements (Ne and so on) until a degenerate iron core forms. No more energy can be released by nuclear fusion at this point. The core ($M \approx 1.5M_\odot$) reaches its Chandrasekhar limit. Photons begin to dissociate iron, a process which consumes energy and thus reduces thermal pressure. Electrons are absorbed by protons and nuclei and are converted into neutrinos,

$$\begin{aligned} e^- + {}^{Z}_{A}X &\rightarrow \nu_e + {}^{Z-1}_{A}X, \\ e^- + p &\rightarrow \nu_e + n. \end{aligned} \tag{3.1}$$

The neutrinos will eventually escape the star, lowering the pressure. Thus the core becomes unstable and collapses. At the densities that are reached inside the core during collapse (10^{12} g cm^{-3}), neutrino scattering cross sections get so high that their diffusion time is of the order of the dynamical collapse time-scale. Therefore neutrinos are trapped inside the core.

As the collapse continues, nuclear densities (3×10^{14} g cm^{-3}) are reached in the core. At these densities, the matter equation of state stiffens drastically. The inner core contracts only little beyond the new equilibrium and then reexpands, usually referred to as “core bounce”. As the outer part of the core falls inwards with supersonic velocities, a shock wave forms at the core bounce, traveling outwards into the supersonic part, as displayed in Fig. 3.1. The shock wave disintegrates the infalling nuclei and thereby loses energy. Once the shock wave passes the neutrino trapping sphere R_ν, neutrinos are no longer scattered mainly by heavy nuclei, but by nucleons and light nuclei, which have much smaller scattering cross sections. Thus the outer material suddenly becomes neutrino-transparent and ν_e are released in the so-called “prompt neutrino burst”, or “deleptonization burst”(phase 2 in Fig. 3.1).

After about a few 100 ms after bounce, at a radius of a few 100 km, the shock wave comes to a halt, because it loses energy by disintegrating nuclei. However, matter is still falling inwards and thus energy is deposited behind the shock wave. Neutrinos that are emitted by the proto-neutron star can be

[1]Our presentation closely follows Ref. [14].

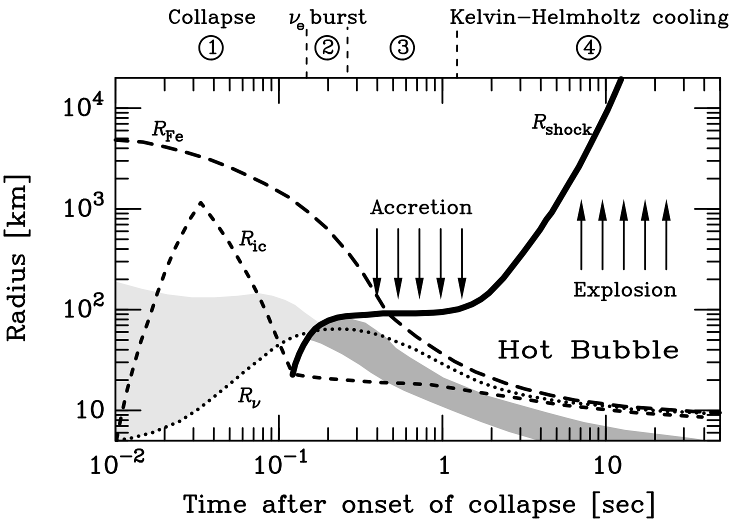

Figure 3.1: Time evolution of different regions inside the SN. Four phases can be distinguished. 1. Collapse of the iron core. 2. Prompt ν_e burst. 3. Accretion phase. 4. Kelvin-Helmholtz cooling of the proto-neutron star. The radius of the iron core is denoted as $R_{\rm Fe}$. The inner core $R_{\rm ic}$ describes the region of subsonic collapse for $t \lesssim 0.1$ s and later the inner region of the proto-neutron star. Neutrinos are trapped inside the "neutrino sphere" R_ν. The shock wave is denoted by $R_{\rm shock}$. The grey area is the region where most neutrinos are produced. Figure from Ref. [34], chapter 11.

absorbed by nuclei in the shock wave. This phase is commonly referred to as "accretion phase" and corresponds to phase 3 in Fig. 3.1. If enough energy is absorbed from neutrinos (i.e. a few percent of the total energy released in neutrinos), the shock will move outwards again and blow off the entire envelope. The new born proto-neutron star cools by emitting neutrinos of all flavors during the Kelvin-Helmholtz cooling phase (phase 4 in Fig. 3.1).

Since the explosion takes place after a period of shock-wave stagnation, this mechanism is referred to as "delayed explosion". It was first suggested by Bethe and Wilson [35]. Their numerical collapse simulations obtained an explosion and a number of more sophisticated simulations in the last two decades also succeeded in this. However, the most recent and elaborate simulations fail to produce an explosion [36, 37, 38, 39, 40].

There are also scenarios where a black hole is born instead of a neutron star [41]. This happens in the case of a very massive star (say, $M = 20M_\odot$) when the proto-neutron star accretes too much matter, reaches its Chandrasekhar limit and collapses. However, this scenario is still being examined and details are not yet settled.

Of the groups that are performing SN simulations, only the Livermore group obtains robust explosions [42]. They include "neutron finger" convection inside the proto neutron star that leads to a sufficiently high neutrino luminosity for a short time, in order to revive the shock wave. However, it is unclear whether neutron finger convection actually takes place in SNe [43, 44, 45, 46, 47]. Instead, groups that use Boltzmann solvers for their calculation of the neutrino transport, which is generally accepted as the state-of-the-art method, do not obtain explosions [37, 38, 39, 40, 48]. The reasons for this failure are yet unknown. It has been suggested that some important effect might not have been accounted for [36].

Despite these difficulties, we have some observational evidence that the delayed explosion mechanism is—at least to some degree—what is realized in nature. We have seen neutrinos from SN 1987A [2, 3], which are a clear sign for a core-collapse, and the progenitor star was a blue super giant, so the notion that SNe occur after the final burning stages of a star seems to be confirmed. For other SNe, neutron stars have been observed as remnants of the explosion. Since the basic features of this mechanism are substantiated, we will assume that it is the right way to understand core-collapse SNe throughout this thesis. More specifically we assume that simulations obtain reasonable predictions of SN neutrino spectra even though they fail to produce an explosion.

3.3 Flavor-Dependent Neutrino Spectra

In order to determine the DSNB, we need the spectral shape of the neutrinos that exit the SN. However, it seems appropriate to explain the rough features of the spectra that we expect by some simple physical arguments before going into a detailed discussion of simulation results. The total energy that is liberated in a SN collapse equals the binding energy of the neutron star that forms after collapse,

$$E_{\mathrm{b}} \approx \frac{3}{5}\frac{G_{\mathrm{N}}\mathcal{M}^2}{R} \approx 3 \times 10^{53}\ \mathrm{erg}. \tag{3.2}$$

It is reasonable to assume that the total energy is approximately equipartitioned between the six neutrino and antineutrino species. Temperatures at the neutrino trapping sphere are typically of the order of 10–20 MeV, so we expect the neutrino energies to be of the same order. The time that neutrinos of that energy need to diffuse through the inner core and reach a neutrino-transparent zone is of the order of a second, hence we expect the emission time of neutrinos to be of the same order.

In addition to these broad spectral characteristics, certain differences between the neutrino species have to be kept in mind. First, ν_μ, ν_τ, $\bar{\nu}_\mu$ and $\bar{\nu}_\tau$ (hereafter collectively referred to as ν_x) do not interact with ordinary matter via charged current interactions at these energies. Therefore, the core

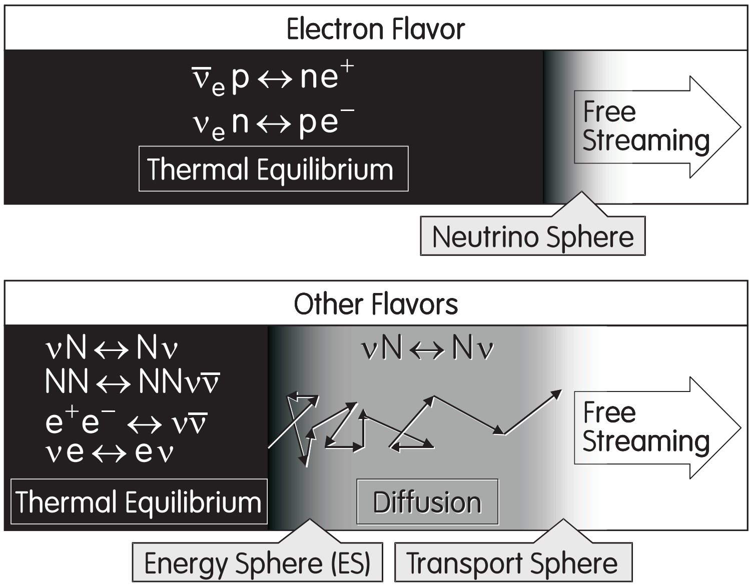

Figure 3.2: Transport of neutrinos inside the SN. *Upper panel:* the $\bar{\nu}_e$ and ν_e-spheres. *Lower panel:* the same for ν_x, except for the number sphere. Figure after Ref. [14].

is more transparent for them than for electron neutrinos and antineutrinos. Their last scattering happens deeper inside the core at higher temperatures, so they have higher energies in general. Likewise, since neutrons are more numerous than protons, ν_e have lower energies than $\bar{\nu}_e$. Typically simulations find [15, 40, 42, 49, 50, 51, 52, 53, 54]

- $\langle E_\nu \rangle$ = 10–14 MeV for ν_e,
- $\langle E_\nu \rangle$ = 11–20 MeV for $\bar{\nu}_e$,
- $\langle E_\nu \rangle$ = 15–27 MeV for ν_x,

to name the rough tendencies.

In order to understand the evolution of the different spectra more deeply, it is necessary to look at the dominant reactions that neutrinos have with ordinary matter. For ν_e and $\bar{\nu}_e$, the emission is displayed schematically in Fig. 3.2. The beta processes $\nu_e n \leftrightarrow pe^-$ and $\bar{\nu}_e p \leftrightarrow ne^+$ keep the neutrinos in local thermal equilibrium (LTE). These reactions become inefficient at a certain radius and neutrinos start streaming freely. However, the position of this neutrino sphere depends on the energy of the neutrinos, since the beta-reactions are also energy-dependent. Thus, neutrinos of different energies decouple at different radii and at different temperatures. Moreover, the number of emitted neutrinos is proportional to the surface of the neutrino sphere of corresponding energy. Therefore it is easy to see that the neutrinos that exit the SN will not be thermal. Their distribution will rather be a convolution of several thermal spectra and thus effectively display a distorted thermal shape. Because of the abundance of neutrons in the proto-neutron star, the neutrino spheres for ν_e are at larger radii, thus they have a lower mean energy compared to $\bar{\nu}_e$. Neutral-current reactions are subdominant for ν_e and $\bar{\nu}_e$, because of the smaller coupling constants.

Tau- and muon-neutrinos do not interact via charged current with ordinary matter since tau leptons are not present at all and muons are not abundant enough to contribute significantly. Neutral current interactions play the dominant role for these neutrino species, as schematically displayed in Fig. 3.2. However, the transport mechanisms are more complicated for ν_x than for ν_e and $\bar{\nu}_e$, since there is a variety of qualitatively different NC interactions which are of comparable importance for the transport process. In the innermost region, ν_x are created and kept in LTE by three reactions,

- Bremsstrahlung $NN \leftrightarrow NN\nu_x\bar{\nu}_x$,
- Neutrino-pair annihilation $\nu_e\bar{\nu}_e \leftrightarrow \nu_x\bar{\nu}_x$,
- Electron-positron pair annihilation $e^+e^- \leftrightarrow \nu_x\bar{\nu}_x$.

No particle creation or annihilation takes place outside the radius at which these reactions cease to be efficient. We call the corresponding sphere the "number sphere". Beyond this region, ν_x are no longer in LTE, but scattering reactions still take place,

- $N\nu_x \rightarrow N\nu_x$,
- $e^{\pm}\nu_x \rightarrow e^{\pm}\nu_x$,

so energy is still exchanged between the neutrinos and the medium. In principle, also scattering on electron neutrinos or antineutrinos $\nu_e\nu_x \rightarrow \nu_e\nu_x$ contributes to energy exchange, but scattering rates are much lower for this process than for the other two. However, these processes differ from each other qualitatively. Scattering on $e^{\pm}$ happens less frequently, since there are less $e^{\pm}$ than nucleons, but more energy is exchanged due to the large recoil of the electrons compared to the nucleons. Electron/positron-scattering freezes out earlier, so there is a region where only nucleon scattering takes place, while little energy is exchanged in each reaction. Therefore, we call the $e^{\pm}$-scattering radius "energy sphere" and the nucleon-scattering radius the "transport sphere". Neutrino diffusion stops at the transport sphere and free streaming starts. The energy and transport sphere are displayed in Fig. 3.2.

The number sphere of ν_x lies deeper inside the star than the neutrino sphere corresponding to ν_e, because neutral-current interaction rates are generally lower. Thus, from a first estimate, one would expect the ν_x to have higher energies. However, energy is still exchanged outside the number sphere, where the number flux is conserved, so neutrinos are scattered down to lower energies. Simulations which take into account $e^{\pm}$ and nucleon scattering therefore obtain lower energies for ν_x than traditional simpler simulations, which contrarily observe a strong hierarchy of ν_x, $\bar{\nu}_e$ and ν_e mean energies. The flattening of energy hierarchies goes so far that mean energies of ν_x and $\bar{\nu}_e$ might actually cross over at late times [14]. Because of the complexity of the involved processes, analytical predictions of the spectra are not feasible. Simulations are therefore the means of choice to obtain useful predictions of the fluxes.

3.4 Characterizing Non-Thermal Neutrino Spectra

For interpreting the results of SN simulations, it is necessary to characterize the non-thermal neutrino spectra with a few physically meaningful parameters. There are numerous possibilities to characterize such spectra, for example by energy momenta. For many applications, notably the calculation of the DSNB, it is useful to have such an analytic expression of the spectra. We will therefore present two common possibilities to fit SN neutrino spectra. Traditionally, a Fermi-Dirac spectrum for a temperature T has been used, where the deviation from the thermal shape is described by a degeneracy parameter η, which is connected to a chemical potential $\mu = \eta T$ [55],

$$f_\eta(E) = \frac{E^2}{1 + \exp(\frac{E}{T} - \eta)}, \tag{3.3}$$

However, physically, there is no such chemical potential that would correspond to ηT and also T does not correspond to a temperature at a physically meaningful radius, but rather to a weighted convolution of neutrino sphere temperatures.

Recently, Keil et al. have therefore introduced a simpler parameterization, which uses a distorted Maxwell-Boltzmann-distribution and has a number of practical advantages [14],

$$f_a(E) = \frac{1}{c_a} \left(\frac{E}{\overline{E}} \right)^a \exp \left[-(a+1) \frac{E}{\overline{E}} \right], \tag{3.4}$$

where c_a is chosen such that $\int_0^\infty dE \ f_a(E) = 1$. More specifically,

$$c_a = (a+1)^{-(a+1)} \Gamma(a+1) \overline{E}. \tag{3.5}$$

Here, $\overline{E}$ equals the first energy moment $\langle E \rangle$, whereas a is a measure for the spectral distortion. For values of $a > 2$, the high energy tail is suppressed

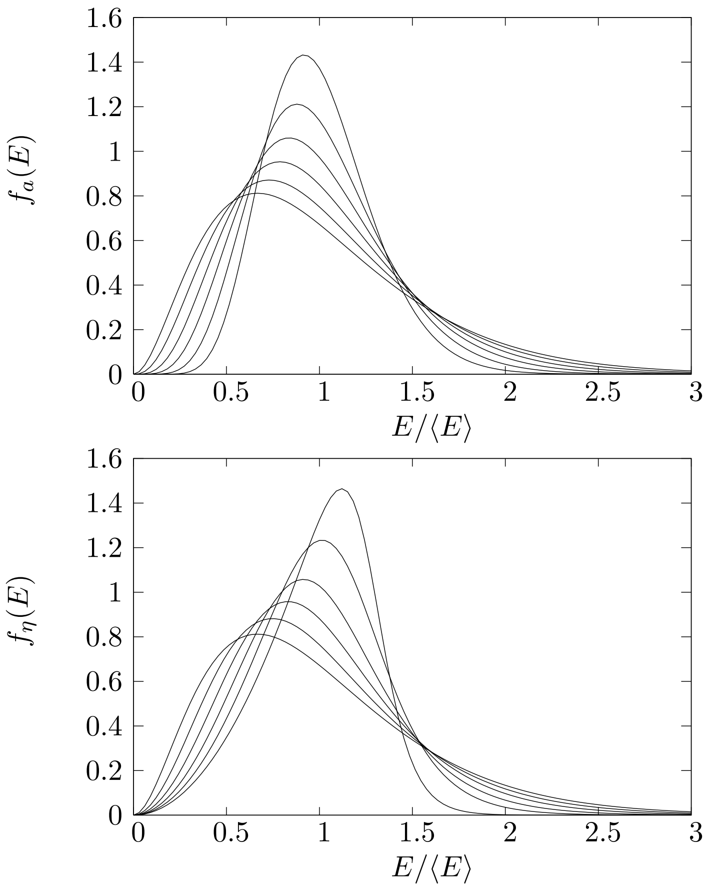

Figure 3.3: Normalized fit functions. *Upper panel:* a-fit according to Eq. (3.4). *Lower panel:* η-fit according to Eq. (3.3). In both panels, the broadest curve corresponds to a Maxwell-Boltzman-distribution, i.e. to $a = 2$ and $\eta = -\infty$, respectively. For the other curves, the width was decreased in steps of 10%. Figure adapted from Ref. [14].

relative to a thermal spectrum (pinched spectrum). For $a < 2$, the high energy tail is enhanced and the peak suppressed (anti-pinched spectrum). Simulations find values of a typically in the range of 2–5, so the spectra are generally pinched. We emphasize that the parameters $\overline{E}$ and a of this fit can be related more directly to the spectral shape of the distribution than the η-fit. In Fig. 3.3, we compare the η and a-parameterization. It can be seen that a and η have essentially the same effect of suppressing or enhancing the high- and low-energy parts of the spectrum. However, the mean energy $\langle E\rangle$ as a physically meaningful parameter naturally stays constant while we vary a. Contrarily, varying η and keeping T constant will change $\langle E\rangle$. Since the a-fit has such practical advantages, we will rather adopt this fit in order to calculate the DSNB.

3.5 Simulations of Different Groups

Now that we have collected the tools to analyze the spectra, we look at some significant recent SN core-collapse simulations and their results concerning neutrino spectra. There have been quite a number of SN simulations in the past [37, 38, 42, 54, 56, 57, 58, 59, 60, 61, 62] which use different numerical codes for their core-collapse simulations and also differ in their result as to how the neutrino spectra evolve with time. It would go beyond the scope of this thesis to list all of them and compare their inputs as well as their results. However, we will present two of them which we hold to be representative and we will choose our parameter range for the neutrino spectra based on these two and a brief discussion of other simulation results.

3.5.1 Livermore

An important class of simulations are the ones obtained by the Livermore group, since they are the only ones that get robust explosions. As mentioned in chapter 3.2, they have to include "neutron-finger" convection inside the proto-neutron star in order to enhance the neutrino luminosities at early times [63, 64]. Thus they observe a delayed explosion, even though the existence of this type of convection is controversial. The numerical codes were developed by Wilson and Mayle [56, 65, 66] and use a multigroup flux-limited diffusion approximation. The latest published Livermore simulation [42] starts from a progenitor star of $20 M_\odot$. It covered the time from the onset of collapse until about the end of the Kelvin-Helmholtz cooling, 18 s after the core bounce. The neutrino luminosities are almost exactly equipartitioned between the species at early times. From about three seconds after bounce on, the ν_x luminosity starts to fall more slowly than the others. The mean energies show a pronounced hierarchy of $\langle E_{\nu_e}\rangle : \langle E_{\bar\nu_e}\rangle : \langle E_{\nu_x}\rangle = 0.8 : 1 : 1.26$ at 300 ms and $0.55 : 1 : 1.25$ at 10 s after bounce.

3.5.2 Garching

Using a different method, Keil, Raffelt and Janka have conducted SN simulations with a novel model of ν_x transport inside the SN core [15]. They find that, contrary to traditional treatments such as the Livermore group, electron neutrino annihilation $\bar\nu_e \nu_e \to \nu\bar\nu$ and bremsstrahlung $NN \to NN\bar\nu\nu$ are the dominant processes for ν_x production, whereas electron-positron annihilation $e^+e^- \to \nu\bar\nu$ is not as important as previously assumed. Moreover, they point out that recoil on nucleons $\nu N \to \nu N$ is an important process for energy exchange between ν_x and the environment, which has not been included in most simulations. They conducted several Monte Carlo simulations for different SN models and found that the hierarchy of mean energies, notably between $\bar{\nu}_e$ and ν_x is not as pronounced as is traditionally assumed. The ν_x and $\bar{\nu}_e$ energies obtained by their simulations typically differ by only 10–20%. Moreover they observe that luminosities of $\bar{\nu}_e$ and ν_e are approximately equal, while they allow for the $\bar{\nu}_e$ and ν_x luminosities to differ by up to a factor of two in either direction. Other simulations, such as the Livermore group, typically find luminosity equipartition. A full-scale simulation using a Boltzmann solver has been conducted by the Garching group [54], which basically confirms the results obtained by the Monte Carlo codes. However, they do not obtain an explosion, and therefore trigger it artificially. Moreover, they limit their simulation to 650 ms after bounce. Thus it is unclear how the observed trends in mean energies and luminosities up to this time would evolve over the full time scale of a SN.

3.5.3 General Tendencies

Taking into account the results of the above mentioned simulations and also searching the literature for other studies, we find the following rough features. The total luminosity liberated in neutrinos will be approximately 3×10^{53} erg, as already described in section 3.3. However, observations of neutron stars typically give masses of $1.2\mathcal{M}_\odot - 1.6\mathcal{M}_\odot$ [67], which places an uncertainty on the binding energy E_b. Moreover, the equation of state for neutron stars is not very well known, notably in the inner core, causing an additional uncertainty in E_b. Thus, it does not seem exaggerated to allow for variations in E_b from 2–5 $\times$ 10^{53} erg, as a rough estimate.

Traditionally, simulations find luminosities of the different neutrino flavors to be approximately equipartitioned [42, 56, 60, 61]. However, more recent simulations still observe $L_{\nu_e} \approx L_{\bar{\nu}_e}$ over the time of neutrino emission, but L_{ν_x} seems to be up to a factor 2 larger or smaller than that, depending on the evolutionary phase. The authors of Refs. [15, 37, 48, 54] find $L_{\nu_x} \approx \frac{1}{2} L_{\nu_e}$ during the accretion phase, while they observe that later luminosities cross over and L_{ν_x} becomes larger than L_{ν_e}, except for Liebendörfer et al. [37], who find L_{ν_x} to stay small. Thompson et al. [40] observe $L_{\nu_x} : L_{\nu_e}$ to be larger than one already during accretion and also at later times. Thus it seems reasonable to assume that after time-integration, $L_{\nu_e} \approx L_{\bar{\nu}_e}$, while one should allow for L_{ν_x} to differ from the latter by up to a factor of two in either direction, because of the different results from simulations. While differences in flavor-dependent luminosities seem to become larger with more sophisticated codes, differences in mean energies appear to become smaller. Traditionally, a strong hierarchy of energies with differences of $\langle E_{\nu_e} \rangle : \langle E_{\bar{\nu}_e} \rangle : \langle E_{\nu_x} \rangle$ about 0.8 : 1 : 1.8 [57, 58] has been assumed. More recent simulations, especially with more appropriate treatment of ν_μ and ν_τ transport, find the energy difference between $\bar{\nu}_e$ and ν_x to be of the order 1 : 1.0–1.3 [15, 37, 38, 40, 42, 60, 61]. The absolute values of energies differ more drastically. Looking for extremes, one can easily find ranges of $\langle E_{\nu_e} \rangle$ = 7–15 MeV, $\langle E_{\bar{\nu}_e} \rangle$ = 8–24 MeV and $\langle E_{\nu_x} \rangle$ = 8–27 MeV, again depending on the evolutionary phase. While most simulations, including many recent ones, find energies to increase or stay constant during accretion, the simulations conducted by Suzuki [60, 61, 62] find decreasing energies at late times, this contributes to the broad range of mean energies. However, the majority of the simulations get time-integrated values that center around $\langle E_{\bar{\nu}_e} \rangle = 16(\pm 4)$ MeV. Since the absolute values differ considerably more than the ratios of mean energies, it is more reasonable to vary the absolute energy range, represented by one reference energy, for example $\langle E_{\bar{\nu}_e} \rangle$, while keeping the energy ratios constant, at about $\langle E_{\nu_x} \rangle : \langle E_{\bar{\nu}_e} \rangle \approx 1.1 : 1$.

While most simulations concentrate on quantifying the luminosities and energies, only few of them give explicit numbers for the spectral pinching, as do the authors of Refs. [15, 54, 59]. All of these works imply a hierarchy of pinching: $a_{\nu_e} > a_{\bar{\nu}_e} > a_{\nu_x}$. One can summarize the ranges that these works get as $a_{\nu_e} = 4.0 \pm 1.0$, $a_{\bar{\nu}_e} = 3.4 \pm 1.1$, $a_{\nu_x} = 2.5 \pm 0.7$. The spectral shapes of other simulations are similar.

Neutrinos exit SNe with approximately equal luminosities, therefore we expect the same amounts of different flavors for the DSNB. An observation of SN neutrinos with different flavors would yield unique information about SN and neutrino properties as has often been pointed out [14]. However, in the case of the DSNB we can only hope to detect the $\bar{\nu}_e$-part of the flux, due to the large cross section for $\bar{\nu}_e p \rightarrow n e^+$, as explained in more detail in chapter 6. Therefore, we reduce our discussion to the $\bar{\nu}_e$-part of the SN spectrum from now on.

In Fig. 3.4 we display typical flavor-dependent spectra from a SN. To illustrate the uncertainty of the ratio of total energies for $\bar{\nu}_e$ and ν_x, we display the three cases $E_{\mathrm{tot},\bar{\nu}_\mathrm{e}} : E_{\mathrm{tot},\nu_\mathrm{x}} = 2$, 1 and $\frac{1}{2}$. One can see that the $\bar{\nu}_e$ and ν_x spectra do not look very different, except for a possible difference in total energies. Electron neutrinos have lower $\langle E \rangle$ in general and therefore a higher flux.

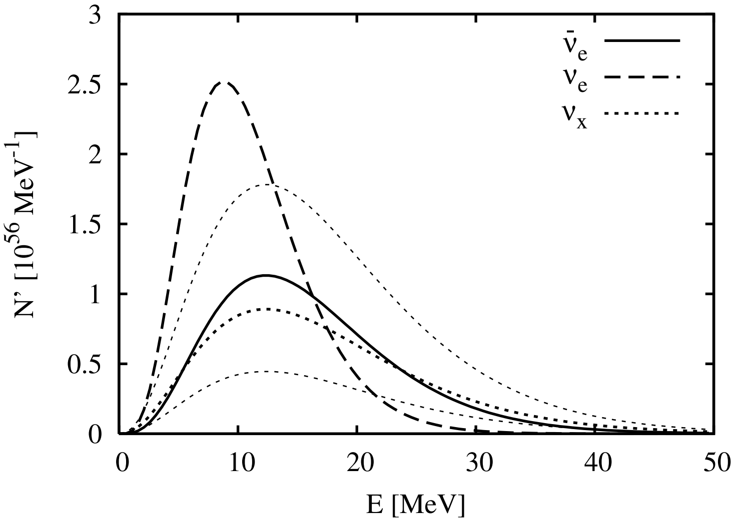

Figure 3.4: Normalized SN neutrino spectra. The dashed curve corresponds to ν_e, the solid curve to $\bar{\nu}_e$. The dotted curves correspond to ν_x, where the three cases $E_{\mathrm{tot},\nu_\mathrm{x}}/E_{\mathrm{tot},\bar{\nu}_\mathrm{e}} = 2$, 1 and $\frac{1}{2}$ are displayed, top to bottom. The spectra are taken to be $\overline{E}_{\nu_e} = 11$ MeV, $\overline{E}_{\bar{\nu}_e} = 16$ MeV, $\overline{E}_{\nu_x} = 17.3$ MeV, $a_{\nu_e} = 4.0$, $a_{\bar{\nu}_e} = 3.4$, $a_{\nu_x} = 2.5$ and $E_{\mathrm{tot}}, \nu_e = E_{\mathrm{tot},\bar{\nu}_\mathrm{e}}$.

3.6 Influence of Oscillations Inside the Supernova

Due to neutrino oscillation, the flavor-dependent neutrino spectra which are produced inside the proto-neutron star will not be the spectra that we will detect on earth. The flavor eigenstates of neutrinos are not mass eigenstates and therefore they mix with other flavors. The phenomenology of neutrino oscillations is well understood, since the mixing angles as well as the mass square differences are fairly well determined by recent solar [68, 69], atmospheric [70] and reactor neutrino experiments [71]. The remaining ambiguities are the value of θ_{13} which is weakly constrained ($\sin^2\theta_{13} \lesssim 0.1$ [72]), and whether the mass hierarchy is normal ($m_1 \ll m_3$) or inverted ($m_1 \gg m_3$). Neutrino oscillations in the SN envelope actually depend to a great extent on the value of θ_{13} and on the type of mass hierarchy. However, we will argue that oscillations do not have a large influence on the resulting effective $\bar{\nu}_e$-spectra for our purpose, even though they are extremely important for neutrinos from a galactic SN. Therefore, we do not repeat the details of the oscillation mechanism, but just recall the implications of the various oscillation cases for the detectable neutrino spectrum.

Dighe and Smirnov [73] have extensively analyzed the effect of neutrino oscillations in the SN envelope. For the case of normal hierarchy, they find that all $\bar{\nu}_e$ at production will after oscillation in the envelope arrive at the stellar surface as the mass eigenstate $\bar{\nu}_1$. This is mainly due to the large matter potentials inside the core of the SN. Thus the effective $\bar{\nu}_e$ spectrum observed on earth will be

$$\begin{aligned} N'_{\bar{\nu}_e} &= |U_{e1}|^2 N'_{\bar{\nu}_1} + |U_{e2}|^2 N'_{\bar{\nu}_2} + |U_{e3}|^2 N'_{\bar{\nu}_3} \\ &= |U_{e1}|^2 {N^0_{\bar{\nu}_e}}' + |U_{e2}|^2 {N^0_{\bar{\nu}_\mu}}' + |U_{e3}|^2 {N^0_{\bar{\nu}_\tau}}' \\ &= |U_{e1}|^2 {N^0_{\bar{\nu}_e}}' + (1 - |U_{e1}|^2) {N^0_{\nu_x}}', \end{aligned} \tag{3.6}$$

where the fluxes with superscript 0 denote the fluxes at production inside the core, $U_{\alpha i}$ is the mixing matrix element between the α-flavor state and the i-th mass eigenstate. The mixing matrix obeys $\sum_{i=1}^{3} |U_{\alpha i}|^2 = 1$. Observationally, $|U_{e1}|^2 = 0.7^{+0.07}_{-0.08}$ [1].

For the case of inverted hierarchy, the value of $\sin^2 2\theta_{13}$ is important. It is connected to the adiabaticity parameter γ, which describes how adiabatic resonance occurs inside the SN. For the case of inverted hierarchy there is one resonance region inside the SN, which can have the effect that neutrinos will be converted to different mass eigenstates, depending on γ and the value of $\sin^2 2\theta_{13}$. For $\sin^2 2\theta_{13} \lesssim 10^{-3}$, $\bar{\nu}_e$ at production will be completely converted to $\bar{\nu}_1$ at the SN surface. Thus the situation will be the same as for normal hierarchy in Eq. (3.6). For simplicity, we will from now on imply this case as well when we talk about "normal hierarchy". For $\sin^2 2\theta_{13} \gtrsim 10^{-3}$, $\bar{\nu}_e$ will exit the SN as $\bar{\nu}_3$, thus the spectrum on earth will be

$$\begin{aligned} N'_{\bar{\nu}_e} &= |U_{e1}|^2 N'_{\bar{\nu}_1} + |U_{e2}|^2 N'_{\bar{\nu}_2} + |U_{e3}|^2 N'_{\bar{\nu}_3} \\ &= (1 - |U_{e3}|^2) {N^0_{\nu_x}}' + |U_{e3}|^2 {N^0_{\bar{\nu}_e}}' \simeq {N^0_{\bar{\nu}_x}}', \end{aligned} \tag{3.7}$$

because $|U_{e3}|^2 \ll 1$ from reactor experiments [72].

It makes sense to fit the spectra *after* oscillation with the a-fit of chapter 3.4, leading to some effective parameters $(L_{\bar{\nu}_e,\mathrm{eff}}, \overline{E}_{\bar{\nu}_e,\mathrm{eff}}, a_{\bar{\nu}_e,\mathrm{eff}})$. We observe that in the normal hierarchy case, the effective parameters follow

$$\begin{aligned} L_{\bar{\nu}_e,\mathrm{eff}} &= p L_{\bar{\nu}_e} + (1-p) L_{\nu_x} \\ \overline{E}_{\bar{\nu}_e,\mathrm{eff}} &\approx p' \overline{E}_{\bar{\nu}_e} + (1-p') \overline{E}_{\nu_x}, \\ a_{\bar{\nu}_e,\mathrm{eff}} &\approx p' a_{\bar{\nu}_e} + (1-p') a_{\nu_x}, \end{aligned} \tag{3.8}$$

where $p = |U_{e1}|^2 = 0.7$ is the probability to find the initial $\bar{\nu}_e$ as $\bar{\nu}_e$ at the detector, $p' = p/(p + (1-p)r)$ is some effective probability, while $r = L_{\bar{\nu}_e}/L_{\nu_x}$ is the ratio of luminosities. For an inverted hierarchy with large $\sin^2\theta_{13}$, the effective parameters are naturally the same as for ν_x.

The uncertainties due to the oscillation scenario are due to the difference between the $\bar{\nu}_e$ and ν_x spectra. However, the uncertainties in the total range

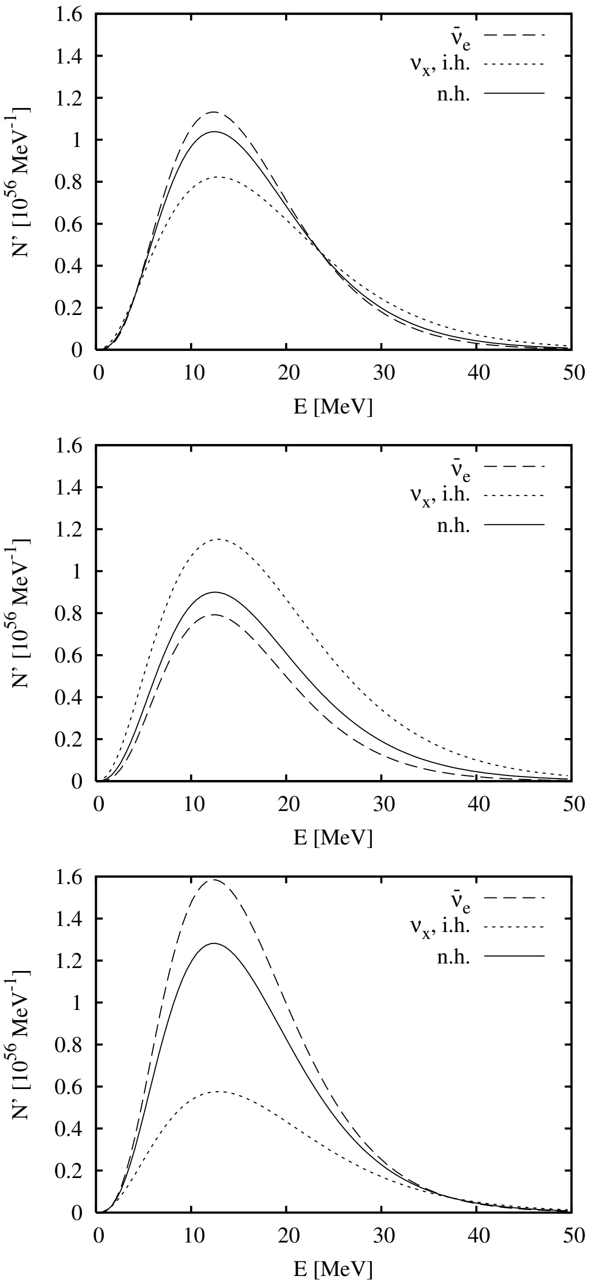

Figure 3.5: Influence of oscillations. The ν_x-spectra also illustrate the case of inverted hierarchy (i.h.) with large θ_{13}. Normal hierarchy is denoted by (n.h.). We vary the ratio of total energies of the $\bar{\nu}_e$ and ν_x-spectrum. The spectral shapes are $\overline{E}_{\bar{\nu}_e} = 16$ MeV, $\overline{E}_{\nu_x} = 18.4$ MeV, $a_{\bar{\nu}_e} = 3.4$, $a_{\nu_x} = 2.5$. *Upper panel*: $E_{\mathrm{tot},\nu_\mathrm{x}} = E_{\mathrm{tot},\bar{\nu}_e} = 50 \times 10^{51}$ erg. *Middle panel*: $E_{\mathrm{tot},\nu_\mathrm{x}} = 35 \times 10^{51}$ erg, $E_{\mathrm{tot},\bar{\nu}_e} = 70 \times 10^{51}$ erg. *Lower panel*: $E_{\mathrm{tot},\nu_\mathrm{x}} = 70 \times 10^{51}$ erg, $E_{\mathrm{tot},\bar{\nu}_e} = 35 \times 10^{51}$ erg.

of parameters are typically larger than the differences in the flavor spectra. For the total luminosity, we do not even know whether $L_{\bar{\nu}_e}$ is larger than L_{ν_x} or smaller. For the mean energies, the difference between the flavors is small, typically 1–3 MeV, while the uncertainty in absolute energies is maybe 10–15 MeV. For the spectral pinching, $a_{\bar{\nu}_e} - a_{\nu_x} \approx 1$ typically, while the total uncertainty is ± 1 as well. Therefore, we conclude that it does not make sense to list the two oscillation scenarios separately. We simply do not know enough about the initial spectra. It seems more appropriate to include the oscillation scenarios in the total uncertainties and to choose values that are compatible with the $\bar{\nu}_e$ and ν_x spectra.

In Fig. 3.5, we display the different oscillation scenarios for $\overline{E}_{\bar{\nu}_e} = 16$ MeV, $\overline{E}_{\nu_x} = 18.4$ MeV, $a_{\bar{\nu}_e} = 3.4$ and $a_{\nu_x} = 2.5$. Here, the $\bar{\nu}_e$-spectrum is motivated by typical values from simulations, while the ν_x-spectrum is based on the ratios $\overline{E}_{\bar{\nu}_e}/\overline{E}_{\nu_x}$ and the observation that $a_{\bar{\nu}_e} - a_{\nu_x}$ is typically about one. We vary the ratio of luminosities in the three panels by a factor of two in either direction. The difference in the normal and inverted hierarchy is pronounced in each case, but the uncertainties in the initial spectra make it impossible to distinguish the two cases with the detection of the DSNB.

3.7 Supernova 1987A

The observation of a SN in the Large Magellanic Cloud in 1987 coincided with a number of neutrino events at the Kamiokande [3], Irvine-Michigan-Brookhaven (IMB) [2] and Baksan [74] detectors. These events have been attributed to the expected neutrino spectrum from such an event and are currently the only observation of SN neutrinos that we have. More specifically, Kamiokande related 12 events to the SN, IMB 8 and Baksan 5. There have been quite a number of analyses of the energy and time distribution of these neutrinos. Probably the most significant work is that of Loredo and Lamb [75, 76], who performed a maximum-likelihood analysis. In their study, they use a simple exponential cooling model for the $\bar{\nu}_e$-temperature as

$$T(t) = T_0 e^{-t/4\tau}, \tag{3.9}$$

where τ is a decay time scale parameter. For this model, their best fit of the energy is $\langle E_{\bar{\nu}_e} \rangle = 9 \pm 1.5$ MeV, where the error corresponds to 68% confidence level (C.L.). Moreover, they find the total luminosity to be $E_{\mathrm{tot},\bar{\nu}_e} = 84 \times 10^{51}$ erg. In addition, they also consider a more complex two-component cooling model, where one component accounts for Kelvin-Helmholtz cooling and the other for neutrinos emitted during the accretion phase. Using this description, they find $\langle E_{\bar{\nu}_e} \rangle = 10 \pm 2$ MeV. Naturally, these results apply only to the effective $\bar{\nu}_e$ spectrum after oscillation inside the SN, and thus they can be directly related to our effective spectrum.

The SN 1987A result for $E_{\mathrm{tot},\bar{\nu}_\mathrm{e}}$ is within the range 30–100 $\times$ 10^{51} erg, which is implied by our discussion of E_b and oscillation effects. However, the findings for the neutrino mean energy imply that we need to extend our parameter range down to lower energies of about $\sim$ 9 MeV. Only very few simulations find energies as low as that [62], but SN 1987A is the only measurement of SN neutrinos that we have up to date, therefore it seems necessary to take the results seriously and allow for such a low mean energy. After all, SN simulations fail to produce an explosion in most cases, hence it might well be that some important effect is missing which could also alter the mean energies.

In summary, we conclude our discussion with the choice of a baseline case for the effective SN neutrino spectrum after oscillations, motivated by simulations, oscillation calculations and SN 1987A observations as

$$\begin{aligned} E_{\mathrm{tot},\bar{\nu}_\mathrm{e}} &= 50 \times 10^{51}\ \mathrm{erg}, \\ \overline{E}_{\bar{\nu}_\mathrm{e}} &= 17\ \mathrm{MeV}, \\ a_{\bar{\nu}_\mathrm{e}} &= 3.1. \end{aligned} \tag{3.10}$$

We allow parameters to vary in the ranges

$$\begin{aligned} E_{\mathrm{tot},\bar{\nu}_\mathrm{e}} &= 30\text{–}100 \times 10^{51}\ \mathrm{erg}, \\ \overline{E}_{\bar{\nu}_\mathrm{e}} &= 9\text{–}22\ \mathrm{MeV}, \\ a_{\bar{\nu}_\mathrm{e}} &= 1.9\text{–}4.3. \end{aligned} \tag{3.11}$$

These ranges are compatible with the predictions of simulations for both the $\bar{\nu}_e$ as well as the ν_x spectrum and are therefore appropriate effective parameters, even though we do not know the oscillation scenario. In Fig. 3.6, we show our baseline case for the $\bar{\nu}_e$ spectrum and the effect that the assumed variations of $\overline{E}_{\bar{\nu}_e}$ and $a_{\bar{\nu}_e}$ have on its shape. A lower mean energy naturally leads to a higher flux, the cases for different energies are well distinguishable. The pinching does not show as much influence in the ranges we chose. We do not display the variation of $E_{\mathrm{tot},\bar{\nu}_\mathrm{e}}$ since it is only a global factor. Summarizing, we admit that the presented range of parameters may be somewhat extreme, but by no means implausible in view of the different uncertainties discussed in this chapter.

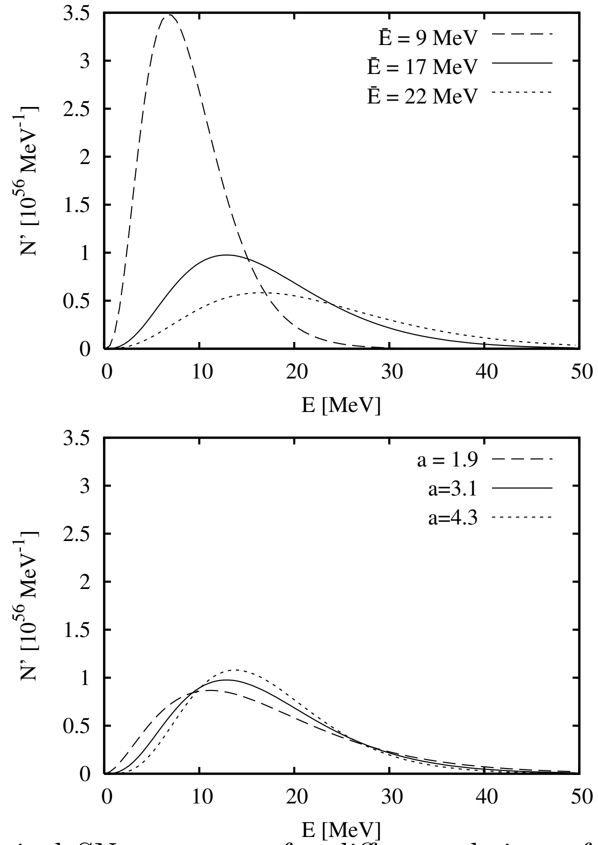

Figure 3.6: Typical SN $\bar{\nu}_e$ spectra for different choices of parameters. We change one parameter and keep the others fixed, according to our baseline case Eq. (3.11)(solid line in both panels). *Upper panel*: we vary the mean energy $\overline{E}$, given in MeV. *Lower panel*: we vary the pinching parameter a.

Chapter 4

Supernova Rate

4.1 Direct Observations

4.1.1 Local Supernova Rate

The most straightforward approach to measuring the SN rate is the direct search for SNe. Statistics have been increasing in the last few years so that now more than 2500 SNe have been detected [77], with a few hundred discoveries per year[1]. Usually, these SNe are discovered in the context of SN searches, such as Asiago [78], Evans' optical search, Calan/Tololo [79], or more recently the Lick Observatory Supernova Search [80], Nearby Supernova Factory Prototype Search [81] and Nearby Galaxies Supernova Search Project [82]. The difficulty in obtaining SN rates from the observations lies in estimating the biases of the corresponding SN search, i.e. *i)* the selection of the observed galaxies, *ii)* the limiting magnitude of observations, and other restrictions that the used instruments and techniques might imply. One of these limiations is the resolution of the telescopes. Distant galaxies have smaller angular size and therefore some SN cannot be resolved from their background. Moreover, in inclined spiral galaxies, SN appear to be fainter than in face-on galaxies because of the increased optical thickness of the galaxy. These limitations are different for each search and therefore the best strategy is to analyze the searches and their biases separately and combine their results in order to obtain higher statistics, since low statistics is another major problem in obtaining accurate results.

Cappellaro et al. [83] have determined local SN rates, using the highest number of SNe so far. They took into account the results of four long-term photometric searches and one visual search (266 SNe total). Following Tammann [84], rates are usually normalized to the galaxy's blue-band luminosity. This is convenient because the SN rate has been found to be proportional

[1] See http://www.pd.astro.it/suprn/snean.txt for a reasonably up-to-date version of *The Asiago SN Catalogue* [78].

to $L_\odot^{\mathrm{B}}$ [85] and the luminosity is relatively easy to measure for large samples of galaxies. After empirically taking into account search biases, Cappellaro et al. [83] obtain an estimate of

$$\begin{aligned} &0.08 \pm 0.04\, h_{75}^2\, \mathrm{SNu} \qquad \text{for type Ib/c,} \\ &0.40 \pm 0.19\, h_{75}^2\, \mathrm{SNu} \qquad \text{for type II,} \end{aligned} \tag{4.1}$$

where $h_{75} = H_0/(75\ \mathrm{km\ s^{-1}\ Mpc^{-1}})$ and $1\ \mathrm{SNu} \equiv 1\ \mathrm{SN\ unit} \equiv 1/(10^{10} L_\odot^{\mathrm{B}} \times 100\ \mathrm{yr})$. These values are in good agreement with previous results [79, 86]. More recently, Strolger has determined local SN rates from three years of data of the CCD-based Nearby Galaxies Supernova Search [82] and found the values

$$\begin{aligned} &0.68 \pm 0.16(\text{stat.}) \pm 0.28(\text{syst.})\ \mathrm{SNu}\ \text{for low dust extinction,} \\ &1.2\ \ \pm 0.3(\text{stat.})\ \ \pm 0.5(\text{syst.})\ \ \mathrm{SNu}\ \text{for large dust extinction,} \end{aligned} \tag{4.2}$$

corresponding to type II SNe.

We can convert the above values, assuming a cosmic blue-band luminosity density $2.0 \times 10^8 h_{100}\ L_\odot\ \mathrm{Mpc^{-3}}$ [82] and get $0.65 \pm 0.25 \times 10^{-4}\ \mathrm{yr^{-1}\ Mpc^{-3}}$ for Cappellaro's (type II/Ib/c) and $0.9 \pm 0.4 \times 10^{-4}\ \mathrm{yr^{-1}\ Mpc^{-3}}$, $1.7 \pm 0.9 \times 10^{-4}\ \mathrm{yr^{-1}\ Mpc^{-3}}$ for Strolger's values (recall that we have taken $h = 0.71$). Strolger gets higher uncertainties due to the smaller statistics of one search. Future results of the new CCD-based SN searches [80, 81] will certainly clarify the issue and an increasing accuracy is to be expected due to the better statistics.

4.1.2 Evolution of the Supernova Rate with Redshift

While the local SN rate is thus relatively well defined by direct observations, the evolution with redshift is hard to assess. However, recently first results of some high-z SN searches have been published [16, 87]. Cappellaro et al. [87] have used data of the European Southern Observatory Supernova Search at Intermediate Redshifts and obtained a SN rate of $1.45^{+0.55}_{-0.45}\ h_{75}^2$ SNu at redshift $z = 0.26$. Dahlen et al. [16] analyzed data taken from the Advanced Camera for Surveys on-board the Hubble Space Telescope as part of the Great Observatories Origins Deep Survey and found rates of $2.51^{+0.88\,+0.75}_{-0.75\,-1.86}$ for $0.1 \leq z < 0.5$ and $3.96^{+1.03\,+1.92}_{-1.06\,-2.60}$ for $0.5 \leq z < 0.9$, where rates are given in $10^{-4}\ h_{70}^3\ \mathrm{yr^{-1}\ Mpc^{-3}}$ and first and second errors denote statistical and systematic errors, respectively. Seventeen core-collapse SNe have been used, thus the systematic errors result from possible misclassification of SNe, as well as the correction for dust extinction. Without correction for dust extinction, rates are lower by a factor of ~ 2. In summary, Cappellaro et al.'s rate is higher by a factor ~ 3 compared to the local SN rate and Dahlen et al.'s by factors ~ 4 and ~ 7, respectively. Within errors, these results agree with each other.

4.2 Connection of the Supernova and the Star-Formation Rate

Even though direct observations of SNe seem to be the best way to measure the SN rate both presently and in the past, there exist indirect tracers of the SN rate as well, the most prominent of them being the star formation rate (SFR). There is an obvious connection between the SFR and the SN rate since the progenitor of any SN must have formed at some point in time. For core-collapse SNe, this connection is even simpler since compared to cosmic timescales, their progenitors live for very short times, typically $\mathcal{O}(10^7\text{yr})$ [88]. If we assume that all stars with $M > M_{\rm crit}$ end as core-collapse SNe and that stellar births and deaths happen simultaneously compared to cosmic time scales for these stars, we obtain a SN rate of

$$R_{\rm SN}(z) = \frac{\int_{M_{\rm crit}}^{\infty} \phi(m,z)\ dm}{\int_{M_{\rm cutoff}}^{\infty} m\ \phi(m,z)\ dm} \psi_*(z), \tag{4.3}$$

where $\phi(m,z)$ is the initial mass function (IMF), $\psi_*(z)$ denotes the SFR at redshift z and $M_{\rm cutoff}$ is the cutoff of the IMF at low energies. Generally, we would have to integrate from $m = 0$, but the IMF is not very well known at small masses. We still know that $\phi(m,z)$ does not diverge at $m = 0$, but rather assumes a constant value. Therefore, the product $m\ \phi(m,z)$ will be sufficiently small at low energies such that introducing an $M_{\rm cutoff}$, if low enough, will not change the integral in the denominator significantly. It has been pointed out, that assuming a constant IMF over redshift seems to be a good approximation, at least for small redshifts ($z \lesssim 2$) [89]. We will only be interested in low redshifts, therefore keeping the IMF constant will not change the resulting DSNB.

If we assume a Salpeter IMF, $\phi(m) \propto m^{-2.35}$, with a lower cutoff at $0.5 M_\odot$ and $M_{\rm crit} = 8 M_\odot$, then

$$R_{\rm SN}(z) = 0.0122\ M_\odot^{-1}\ \psi_*(z). \tag{4.4}$$

However, this conversion factor depends crucially on $M_{\rm crit}$ which is in the range 7–10 $M_\odot$. It will not depend much on the lower cutoff since the slope of the IMF gets shallower towards low m and the product $m\ \phi(m)$ will not contribute much to the denominator of Eq. (4.3) for small m.

4.3 Estimators of the Star-Formation Rate

The advantage of determining SN rates via the SFR is that there exist a variety of observables that are suitable tracers of the SFR [90]. The statistics for stellar births are also about two orders of magnitude better, that is about two orders of magnitude more stars are born with $M > 8M_\odot$ than explode as core collapse SNe, as Eq. (4.4) illustrates. These tracers can be measured up to redshifts as high as $z \sim 6$ [91, 92, 93]. We will review the different estimators, listed according to the corresponding photon frequencies. A complete review can be found in Ref. [90], while Refs. [94, 95, 96] present comparisons of different tracers.

4.3.1 Radio Estimators

It is possible to obtain an indirect estimate of the SFR via observations of the 1.4 GHz radio band. The emission of the observed non-thermal radiation at this frequency is believed to originate mainly from synchrotron radiation by SN remnants [97]. The advantage of such an estimator is that it is not affected by dust extinction and for our purposes, it can be directly related to the SN rate. The most recent and accurate calibration of this estimator is by Sullivan et al. [95].

4.3.2 Far-Infrared Estimators

One of the main characteristics of young stars compared to older stars is that they emit most of their light in the blue-to-ultraviolet part of the spectrum, whereas older populations emit almost exclusively in the red, at wavelengths well over 4000 Å [98]. Figure 4.1 shows the integrated spectra for galaxies of different type in the Hubble sequence and illustrates that an increase in star-formation activity corresponds to an increase in the UV luminosity, since late-type spirals and irregular galaxies are known to have higher SFRs. However, the UV luminosity is heavily affected by dust extinction and therefore problematic to measure. If one assumes an optically thick, dusty environment in which all UV radiation emitted by young stars is absorbed by dust and reemitted in the IR, at wavelengths of roughly 10–300 μm, then it is also possible to obtain a measurement of the SFR by measuring the IR part of the galaxy spectrum [90, 100]. This is feasible because young stars are far more luminous than long-lived stars. Thus the IR-luminosity by older stars does not contribute significantly. However, in reality not all galaxies are that optically thick and the specific dust distribution will alter the absorption and emission process.

4.3.3 Emission Line Estimators

The Hα line is a star-formation indicator because only short-lived stars produce significant luminosity in photons with energies above the hydrogen ionization energy of 13.6 eV, so that ionization and recombination can occur.

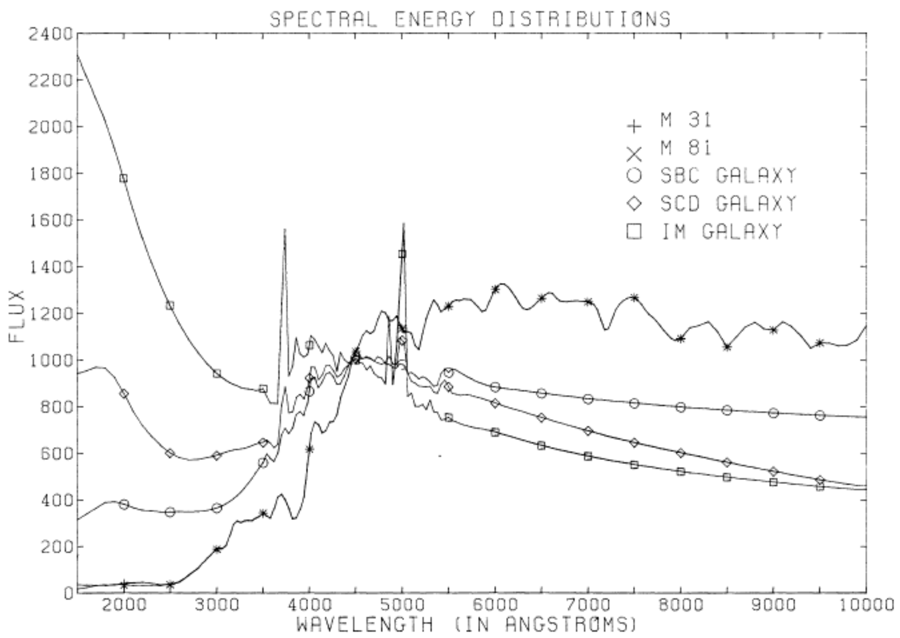

Figure 4.1: Spectral energy distributions, bottom to top: Elliptical, Sbc, Scd and Irregular galaxies. The blue-to-UV luminosity (1500–4000 Å) rises for late-type spirals and irregular galaxies). Figure adapted from Ref. [99].

It is to some extent affected by dust extinction, but far less than the UV-continuum. A calibration can be found in Ref. [90]. Other emission lines can be used to infer the SFR. The most widely used is the [OII] emission line. It has been empirically calibrated using Hα and found to behave sufficiently well to work as a valid tracer [90, 101].

4.3.4 Ultraviolet Estimators

Short-lived stars tend to have high temperatures, so the UV continuum of galaxies is an indicator of recent star formation. As in the other tracers, some modeling of the star-formation process via population synthesis and a chosen IMF is necessary. In this way Madau et al. [102] derived their calibration between 1500 and 2800 Å. These UV estimators are most sensitive to the presence of dust in the environment of the emitting galaxies, and extinction can be as high as a factor of 5–10, although these values are difficult to quantify. The distribution of dust over the galaxy can also alter the spectrum significantly [103].

4.3.5 X-rays and Indirect Tracers

Diffuse X-ray emission in normal galaxies can also act as a tracer of the star-formation history [104], if it is driven mostly by the evolution of the X-ray binary population. However, the work on this method is still very recent and the predicted X-ray emission is very small [105, 106]. Of course it is also possible to study star-formation history not by looking at the emitted radiation but rather at the products and effects of the star-formation process. Efforts in these directions have measured the decrement of the universal gas content measured in damped Lyman-α systems [107].

4.4 Observations of the Star-Formation Rate

Since the mid-90s, there has been an increasing release of star formation history measurements, in the UV [8, 91, 102, 108, 109, 110, 111, 112, 113], as well as in the far IR [114, 115] and Hα [116, 117, 118, 119]. Basically the measurements agree with each other in the observation of a rise in the SFR up to a redshift $z \approx 0.8$–2. However, the agreement in *ratios* of the SFR at different redshifts is much better than the agreement on the *absolute values* of SFRs, notably estimates of the local SFR differ widely. Star formation has been measured beyond $z = 2$, but the measurements show large scatter and it is not clear whether star formation continues to rise (though at a lower rate) at very high redshifts or decreases. However, we will see that the DSNB is insensitive to star formation beyond $z \sim 2$–3 in the energy range accessible to detectors, therefore the onset of star formation is not important for our purposes, since it is believed to be sometime before $z \sim 6$. The scatter in the observations originates from different problems, naturally from the fact that tracers are indirect measurements. An even more important difficulty are the uncertainties due to dust extinction, which are especially important for the UV-measurement at high z. Because of these uncertainties, it makes sense to choose a rough parameterization of the SFR, which can easily be converted to a parameterization of the SN rate, fix some parameter ranges and analyze the dependence of the DSNB on the different parameters.

Hogg [120] and Baldry et al. [121] have introduced a parameterization of the star-formation history,

$$\psi_*(z) = \psi_*^0 \begin{cases} (z+1)^\beta & \text{for} \quad z < 1 \\ 2^{\beta-\alpha}(z+1)^\alpha & \text{for} \quad 1 \le z < z_{\max} \\ 0 & \text{for} \quad z > z_{\max}, \end{cases} \tag{4.5}$$

where $z_{\max}$ is the assumed onset of star formation, ψ_*^0 the local SFR and α and β parameters. This step is motivated on the one hand by the large amount of data for the SFR at $z \lesssim 1$ compared to higher redshifts, where star-formation tracers display large uncertainties. On the other hand it stems

Table 4.1: Parameter β from different SFR studies, compiled by Hogg [120]

Authors	References	β
Lilly et al. (1996)	[108]	3.93 ± 1.07
Hammer et al. (1997)	[122]	7.22 ± 1.03
Rowan-Robinson et al. (1997)	[100]	6.93 ± 4.16
Hogg et al. (1998)	[123]	2.88 ± 0.61
Cowie et al. (1999)	[124]	1.09 ± 1.35
Flores et al. (1999)	[115]	4.47 ± 3.02
Mobasher et al. (1999)	[125]	-4.05 ± 1.18
Haarsma et al. (2000)	[126]	3.61 ± 1.48
Jones and Bland-Hawthorn (2001)	[127]	2.21 ± 2.76
Lanzetta et al. (2002)	[128]	0.67 ± 0.68
combined Hα	[116, 118, 119]	3.75 ± 0.51
Hogg's mean	[120]	2.7 ± 0.7

from the observation that the SFR seems to change its behavior above $z \sim 2$, which implies that a description of the SFR can be divided into two regimes, low and high redshift.

Hogg [120] has compiled a meta-analysis of ten studies, including UV [108, 124, 128], Hα and [OII] emission line [116, 118, 119, 122, 123, 127], far IR [100, 115] and 1.4 GHz radio estimators [125, 126]. He compared the best-fit β-parameters from these studies and found the values summarized in Tab. 4.1. He compiled these measurements into an overall best-fit value of $\beta = 2.7 \pm 0.7$. Baldry et al. [121] have developed a novel method to infer the star-formation history not from total luminosities measured at a certain redshift, but rather by fitting the volume-averaged, luminosity-weighted, stellar absorption line spectrum of present day galaxies, the so-called cosmic spectrum, to models of population synthesis. They emphasize that their method gives reliable results, even though there is some degeneracy between low-redshift and high-redshift star formation. They use data from the 2dFGRS and find results corresponding to constraints of about $\beta = 1$–4.5 and $\alpha \lesssim 1$. Glazebrook et al. [129] applied the same method to data from the Sloan Digital Sky Survey (SDSS), as well as from the 2dFGRS and found that their models agree with ranges of $2 < \beta < 3$ and $0 < \alpha < 1$. Lanzetta et al. [128] have claimed that observations are missing a large part of the high redshift star formation due to unaccounted-for dust extinction and presented a new method of correction for this bias. Thus they obtained a rise in the star formation rate at high redshifts, which would correspond to $\alpha \approx 1$–3. However, Glazebrook et al. [129] find a rejection of these observations with their analysis of the cosmic spectrum.

4.5 Discussion

We have assembled some major observations and specified the main means to estimate the SN rate and also the main uncertainties. Based on these results, we will proceed to make some reasonable assumptions concerning the choice of our parameters, in order to implement them into the calculation of the DSNB. There are not many measurements of the local SN rate and existing observations deal with small statistics (266 SNe used by Cappellaro). Despite this, it seems likely that these direct results will give a more accurate parameter range than the local SFR, due to the high uncertainties both in the local SFR and also in the conversion factor between the SN rate and the SFR. Baldry and Glazebrook [130] obtain values for $\psi_*(t_0)$ ranging from 0.7 to $4.1 \times 10^{-2}h\ M_\odot\ \mathrm{yr}^{-1}\ \mathrm{Mpc}^{-3}$. If we take Baldry and Glazebrook's best-fit IMF, $\phi(m) \propto m^\Gamma$ with $\Gamma = -0.5$ for $0.1\ M_\odot \leq m < 0.5\ M_\odot$ and $\Gamma = -1.15 \pm 0.2$ for $0.5\ M_\odot \leq m < 120\ M_\odot$, the conversion factor in Eq. (4.3) yields 0.0130. However, if we change the slope Γ for $m > 0.5\ M_\odot$ to -0.95 (-1.35), we get a conversion factor of 0.0086 (0.0178) which is 34% lower (37% higher). If we change the lower mass end for SN progenitors to 6 $M_\odot$ [131] or $11 M_\odot$ [132], then the value changes to 0.0141 or 0.0068, respectively, which is 40% higher or 32% lower. Taking into account these uncertainties and converting them to errors on the SN rate, Baldry and Glazebrook's local SFR yields $R_{\mathrm{SN}}(0) = 2.2 \pm 2.0$, where the large error displays the uncertainties in the IMF and the critical lower mass. However, even Strolger's [82] relatively high SN rate of 1.2 SNu for high dust extinction is lower than this value. It is likely that Cappellaro's [83] relatively low result displays reality better because of higher SN statistics. Thus it makes sense to assume a local SN rate ranging from 0.4 to $2.6 \times 10^{-4}\ \mathrm{yr}^{-1}\ \mathrm{Mpc}^{-3}$, to allow for the high values of Strolger [82].

Considering the parameter β which describes the recent star-formation history, there is overwhelming evidence for a rise of the SFR to $z = 1$ from a variety of indicators [100, 108, 126, 122]. In Hogg's compilation(Table 4.1), most groups find β between 0.5 and 4.5, except for two outliers. Hogg discusses these outliers and suspects that Hammer et al.'s [122] uncertainties might be estimated too small and are better to be treated as lower limits. He finds the other outlier, Mobasher et al. [125], to be a more serious problem and settles the issue by referring to the small statistics of this group (25 galaxies with about 25% of them excluded). In our study, we will allow $\beta = 1$–4, in order to include on the one hand the possibility of a relatively steeply evolving SFR from $z = 1$ to present, like Lilly et al. [108], for who Hogg finds $\beta = 3.9 \pm 1.0$, on the other hand the possibility of a shallow SFR evolution like Cowie et al. [124] or Lanzetta et al. [128] who find $\beta = 0.5$–1.5.

Concerning the high-redshift star-formation evolution ($z > 1$), the situation is even less clear. The extremes range from a steep decline after $z \approx 1.5$ as obtained by the pioneering Madau-study [8], over a constant SFR at high z by Steidel et al. [91] to a significant rise by Lanzetta et al. [128]. We also note that the chosen parameterization for α and β is not suitable to fit some star-formation scenarios very accurately. For example the Madau plot [8] can only be fitted very poorly and there is either a large discrepancy for $z = 1$–2 or at $z > 2$, simply because Madau's maximum does not occur at $z = 1$, but rather at $z \approx 1.5$. However, it is only important to choose α to account *approximately* for star formation up to $z = 1.5$ or $z = 2$, since we will see that in a typical scenario, assuming an optimistic detection window, only 7% of the detected DSNB flux will be from redshift $1 < z < 1.5$, 2% will be from $1.5 < z < 2$ and only 1% will be from $z > 3$. In fact the importance of the SFR for the DSNB decreases approximately as $(1 + z)^{-1}$ in the accessible detection window (7–40 MeV). Thus we will choose α to lie between -1 and 1 in order to allow for both low and high star formation at high redshifts ($1 < z < 2$).

Concerning the onset of star formation $z_{\rm max}$, there are several observations for star formation at $z \approx 6$ [92, 93] and some searches report star formation at even higher redshifts [128]. However, we will argue that a variation of $z_{\rm max}$ does not change the detectable DSNB at all as long as $z_{\rm max} > 5$. It does change the low-energy part of the flux, therefore we will include it for now as a parameter to study its influence on the DSNB. We choose a rather high onset of star formation $z_{\rm max} = 20$ for our calculations and examine cases of other choices.

Summarizing the discussion in this chapter, we choose a baseline estimate for the parameterization of the SN rate,

$$\begin{aligned} R^0_{\rm SN} &= 0.7 \times 10^{-4}\ {\rm yr}^{-1}\ {\rm Mpc}^{-3}, \\ \beta &= 2.5, \\ \alpha &= 0, \\ z_{\rm max} &= 20, \end{aligned} \tag{4.6}$$

which works well for our purposes. Taking into account the discussed uncertainties, we allow these parameters to vary in the ranges

$$\begin{aligned} R^0_{\rm SN} &= 0.4\text{–}2.6 \times 10^{-4}\ {\rm yr}^{-1}\ {\rm Mpc}^{-3}, \\ \beta &= 1.0\text{–}4.0, \\ \alpha &= -1\ \text{to}\ +1, \\ z_{\rm max} &= 5\text{–}100. \end{aligned} \tag{4.7}$$

Again, the chosen ranges for these parameters may be somewhat extreme, but they represent possible scenarios that are not excluded by observations.

Chapter 5

Diffuse Supernova Neutrino Background Fluxes

5.1 Analytic Fit

We have now assembled all the pieces required to calculate the DSNB. Summarizing the results of the previous chapters, we recall that the flux is given by Eq. (2.17),

$$\Phi(E) = \int_0^{z_{\max}} \frac{N'_{\rm SN}(E(z+1))R_{\rm SN}(z)dz}{H_0\sqrt{(z+1)^3\Omega_{\rm m}+\Omega_\Lambda}}. \tag{5.1}$$

Here, the SN rate is taken to be

$$R_{\rm SN} = R^0_{\rm SN} \times \begin{cases} (z+1)^\beta & \text{for} \quad z<1, \\ 2^{\beta-\alpha}(z+1)^\alpha & \text{for} \quad 1 \le z < z_{\max}, \\ 0 & \text{for} \quad z > z_{\max}. \end{cases} \tag{5.2}$$

$$\tag{5.3}$$

The $\bar\nu_e$ spectrum of an individual SN is assumed to be of the form

$$N'_{\rm SN}(E) = \frac{E^{\rm SN}_{\rm tot}}{\overline{E}_{\rm SN}}\frac{1}{c_{\rm SN}}\left(\frac{E}{\overline{E}_{\rm SN}}\right)^{a_{\rm SN}} \exp\left[-(a_{\rm SN}+1)\frac{E}{\overline{E}_{\rm SN}}\right], \tag{5.4}$$

where $c_{\rm SN}$ is chosen such that $\int_0^\infty dE\ N'_{\rm SN}(E) = E^{\rm SN}_{\rm tot}/EmSN$. We have found that the SN $\bar\nu_e$ spectrum after oscillation can be described well by three parameters, the total neutrino energy $E^{\rm SN}_{\rm tot}$, the mean energy $\overline{E}_{\rm SN}$ and the spectral pinching $a_{\rm SN}$. From now on, we will denote these parameters with the subscript "SN". Moreover, the SN history can be parametrized by four parameters, the local SN rate $R^0_{\rm SN}$, the recent SN history β, the early SN history α, and the onset of SN explosions $z_{\max}$. One has to keep in mind however, that the SN history parameterization does not fit all theoretical curves very well, but is rather an approximation that tries to describe the SN rate by some intuitive quantities. It works rather well for our purposes.

It seems desirable to adopt a baseline case for these seven parameters. Founded on our discussion in the previous chapters, we choose our baseline case as

$$\begin{aligned} R^0_{\rm SN} &= 0.7 \times 10^{-4}\ \mathrm{yr}^{-1}\ \mathrm{Mpc}^{-3}, \\ \beta &= 2.5, \\ \alpha &= 0, \\ z_{\rm max} &= 20, \\ E_{\rm tot} &= 50 \times 10^{51}\ \mathrm{erg}, \\ \overline{E} &= 17\ \mathrm{MeV}, \\ a &= 3.1, \end{aligned} \tag{5.5}$$

where we allow the parameters to vary in the broad ranges

$$\begin{aligned} R^0_{\rm SN} &= 0.4\text{–}2.6 \times 10^{-4}\ \mathrm{yr}^{-1}\ \mathrm{Mpc}^{-3}, \\ \beta &= 1.0\text{–}4.0, \\ \alpha &= -1 \text{ to } 1, \\ z_{\rm max} &= 5\text{–}100, \\ E_{\rm tot} &= 30\text{–}100 \times 10^{51}\ \mathrm{erg}, \\ \overline{E} &= 9\text{–}22\ \mathrm{MeV}, \\ a &= 1.9\text{–}4.3. \end{aligned} \tag{5.6}$$

For our further discussion, we will always take $R^0_{\rm SN}$ to be given in units of $10^{-4}\ \mathrm{yr}^{-1}\ \mathrm{Mpc}^{-3}$, $E^{\rm SN}_{\rm tot}$ in units of 10^{51} erg and $\overline{E}_{\rm SN}$ in units of MeV.

Since the DSNB itself emerges as a convolution of distorted thermal spectra and the SN history, its shape will resemble a distorted thermal spectrum as well. Therefore, it is an obvious step to try and fit the *resulting* DSNB to a distorted thermal spectrum as well. Such a fit would not only give us an understanding of the main features of the DSNB spectral shape, but would also be extremely useful for further calculations, especially if an analytic description for the dependence of the DSNB fit parameters on the seven input parameters can be found. It appears reasonable to assume that the DSNB can be fitted well by the a-fit and we choose this method because of the practical advantages discussed in chapter 3. The DSNB then reads

$$\Phi(E) = F_{\rm tot}\frac{1}{c_a}\left(\frac{E}{\overline{E}}\right)^a \exp\left[-(a+1)\frac{E}{\overline{E}}\right], \tag{5.7}$$

where the quantities a and $\overline{E}$ will from now on denote the parameters for the DSNB. Moreover, c_a is defined according to Eq. (3.5) and $F_{\rm tot} = \int dE\, \Phi(E)$

denotes the total DSNB flux. The detection of the DSNB is based on charged-current interactions with protons $\bar{\nu}_e p \to n e^+$, thus the flux has to be multiplied by the cross section for this process in order to get the event rate. The cross section for inverse beta decay scales $\propto E_e p_e$, where $E_e = E_\nu - 1.3$ MeV. Moreover, the DSNB can only be detected in an approximate window of 10–40 MeV because of the backgrounds from reactor and atmospheric neutrinos. Motivated by these considerations, we perform a least mean square fit for $E^2\Phi(E)$ and fit only in the energy range 8–40 MeV.

We express the fit in terms of parameters for the flux. However, if one prefers to have the spectral shape of the flux multiplied with the energy squared, $E^2\Phi(E)$, which is essentially the eventrate at a detector, one can use following expressions

$$\begin{aligned} a_{\text{events}} &= 2 + a, \\ \overline{E}_{\text{events}} &= \overline{E}\,\frac{3+a}{1+a}, \\ C_{\text{tot,events}} &= \frac{2+a}{1+a} F_{\text{tot}} \overline{E}^2, \end{aligned} \tag{5.8}$$

where we have chosen the index "events" to denote the connection to the positron event rate. The normalizing factor $C_{\text{tot,events}}$ corresponds to F_{tot} in Eq. (5.7). Multiplied with the cross section, the number of target protons and the detection efficiency, it corresponds to the total rate of positron events N_e. Equation (5.8) can be used to infer the event rate from the flux, even though the relation is not exact, since $E_e = E_\nu - 1.3$ MeV. However, it is still a useful approximation.

Concerning the quality of the fit, it turns out that the functional form of the a-spectrum fits reaonably well in the energy range 10–30 MeV. The deviation of $E^2\Phi_{\text{fit}}(E)$ from $E^2\Phi_{\text{DSNB}}(E)$ is less than ten percent in this regime for most input parameters. It is only larger than ten percent in a few cases and only at energies where the flux is very low. In Figure 5.1, we display the quality of the fit for our baseline case and an additional case with high recent star formation $\beta = 4$, where the fit is not very good above 30 MeV. However, at 30 MeV, $E^2\Phi$ is very low, so that the fit still works well for our purposes. Naturally, the fit does not work as well at energies below 8 MeV. In fact, there are discrepancies of up to 30% in the low energy regime. Because the detection window is above 8 MeV, these discrepancies are not important. However, the parameters F_{tot} and $\overline{E}$ differ from the total DSNB flux and the DSNB mean energy. More specifically, the total flux is generally larger than F_{tot}, a typical value being 20%. The DSNB mean energy $\langle E \rangle$ is lower than $\overline{E}$ by typically 10%. This has to be kept in mind when intrepreting the results of our fit.

Table 5.1 shows fits for various DSNB scenarios. We have hereby varied one parameter and kept the others fixed according to our baseline case. We

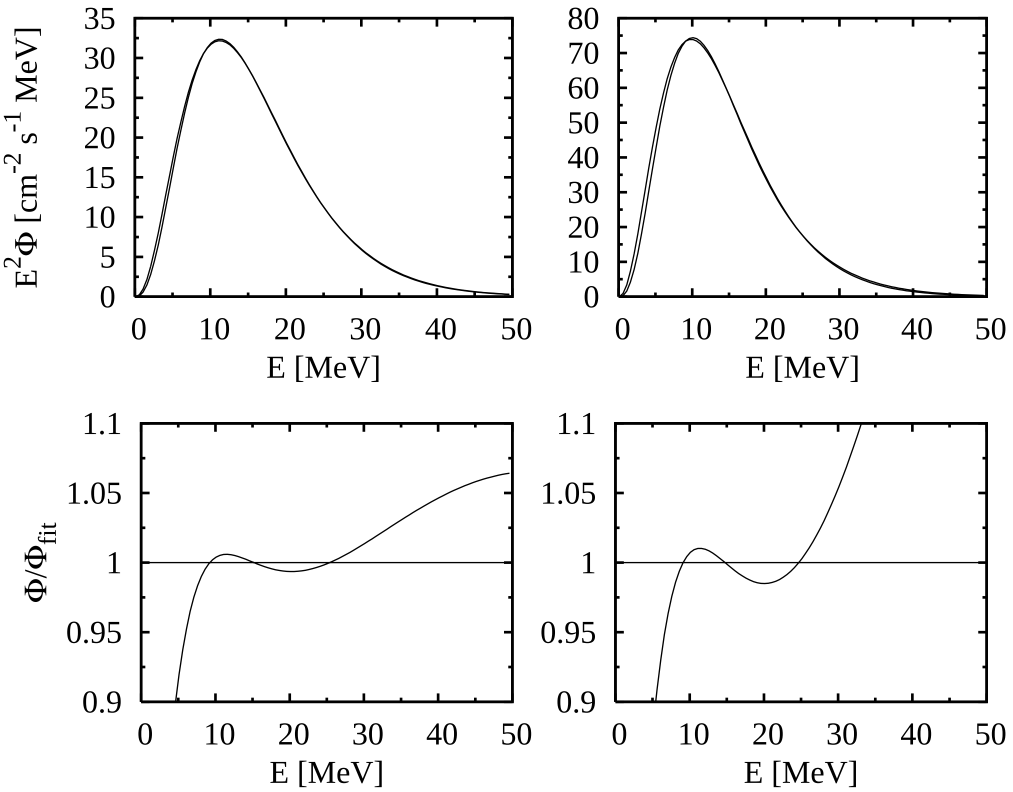

Figure 5.1: The predicted DSNB compared with the analytic fit. The upper panels show the calculated DSNB and the fit, both as a solid line. The lower panel shows the ratio of calculation and fit. The left panels are for our baseline case. In the right panel, $\beta = 4$, all other parameters follow the baseline estimate.

include the variation of $R^0_{\rm SN}$ and $E^{\rm SN}_{\rm tot}$, even though these parameters have only a linear influence on the DSNB,

$$\begin{aligned} F_{\rm tot}(R^0_{\rm SN}) &= F_{\rm tot}(0.7)\frac{R^0_{\rm SN}}{0.7}, \\ F_{\rm tot}(E^{\rm SN}_{\rm tot}) &= F_{\rm tot}(50)\frac{E^{\rm SN}_{\rm tot}}{50}. \end{aligned} \tag{5.9}$$

We do not show the influence of the variation of $z_{\rm max}$. Neutrinos that come from $z > 5$ will only alter the very low-energy part of the DSNB, below 8 MeV. However, this region is inaccessible for observations because of the reactor neutrino background. Thus $z_{\rm max}$ does not alter the detectable part of the spectrum.

Figures 5.2 and 5.3 show the dependence of each fit parameter on each input parameter, keeping the others fixed according to the baseline case. Here, we do not show the linear influence of $R^0_{\rm SN}$ and $E^{\rm SN}_{\rm tot}$. The total DSNB is

Table 5.1: Fit of different DSNB fluxes. The left column shows the parameter that we vary, while we keep the others fixed according to our baseline case.

Varied parameter	Fit parameters		
	F_{tot} [cm^2 s MeV]$^{-1}$	$\overline{E}$ [MeV]	a
Baseline Eq. (5.5)	7.94	6.69	0.469
$R^0_{\mathrm{SN}} = 0.4$	4.53	6.69	0.469
$R^0_{\mathrm{SN}} = 2.6$	29.48	6.69	0.469
$E^{\mathrm{SN}}_{\mathrm{tot}} = 30$	4.76	6.69	0.469
$E^{\mathrm{SN}}_{\mathrm{tot}} = 100$	15.87	6.69	0.469
$\beta = 1$	2.91	8.52	0.836
$\beta = 4$	21.93	5.69	0.368
$\alpha = -1$	6.17	7.61	0.765
$\alpha = +1$	12.44	5.20	0.049
$\overline{E}_{\mathrm{SN}} = 9$	17.38	3.24	0.290
$\overline{E}_{\mathrm{SN}} = 22$	5.81	8.96	0.559
$a_{\mathrm{SN}} = 1.9$	8.80	6.12	0.048
$a_{\mathrm{SN}} = 4.3$	7.38	7.08	0.855

mainly dependent on the late SN history and the local SN rate, which is partly due to the large parameter range we chose for β and R^0_{SN}. Thus the total flux seems to be a good tool to infer the SN history and SFR, even though there is a degeneracy in R^0_{SN} and β and F_{tot} might be slightly influenced by variations in $E^{\mathrm{SN}}_{\mathrm{tot}}$, α and $\overline{E}_{\mathrm{SN}}$ as well. The mean energy $\overline{E}$ is most strongly affected by a change in the spectral mean energy $\overline{E}_{\mathrm{SN}}$, and therefore we will be able to constrain this parameter by analyzing $\overline{E}$. Other influences come from the early and recent star formation α and β. The detectable spectral pinching a will be influenced by β, α and a_{SN} to about equal amounts, therefore it seems hard to constrain one of these parameters. This is especially true since the detectors cannot infer the ratio of the peak to the low-energy rise and high-energy tail, due to background. All parameters depend approximately linearly on each other in the parameter range of interest, with the exception of the recent star formation history β which shows at least quadratic influence on F_{tot} and a.

It seems worthwhile to try to fit the dependence of the fit parameters on the input parameters, as displayed in Figs. 5.2 and 5.3, by some analytic expression. A simple approximation is to fit the input parameters according to the way we already displayed them, which is to catch only the dependence on one input parameter and keep the others fixed. Considering the shape of the curves in Figs. 5.2 and 5.3, a quadratic fit seems to be sufficient. More specifically, we assume that each of the fit parameters depends on each of

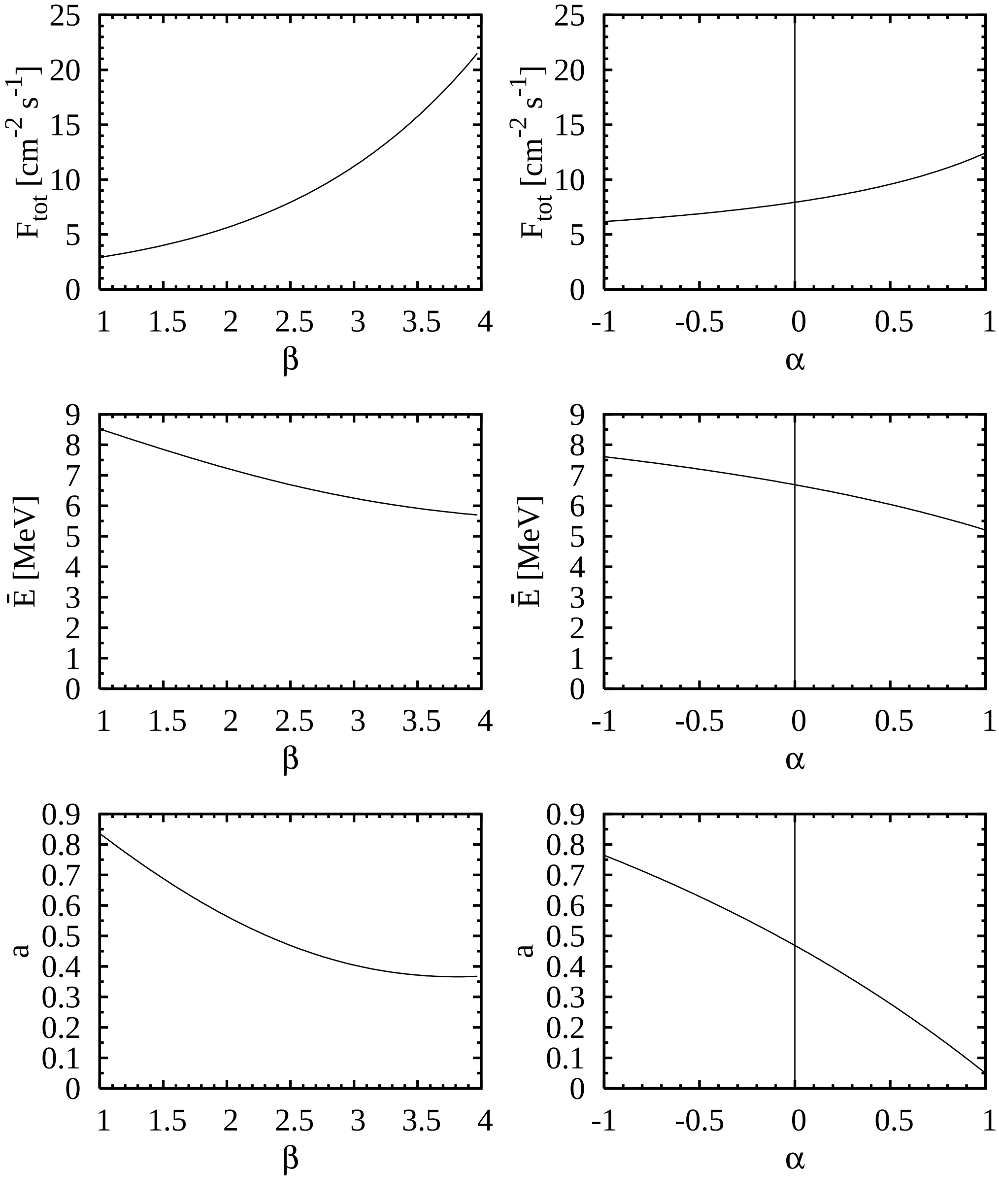

Figure 5.2: Dependence of the fit parameters on the recent SN history β and the early SN history α.

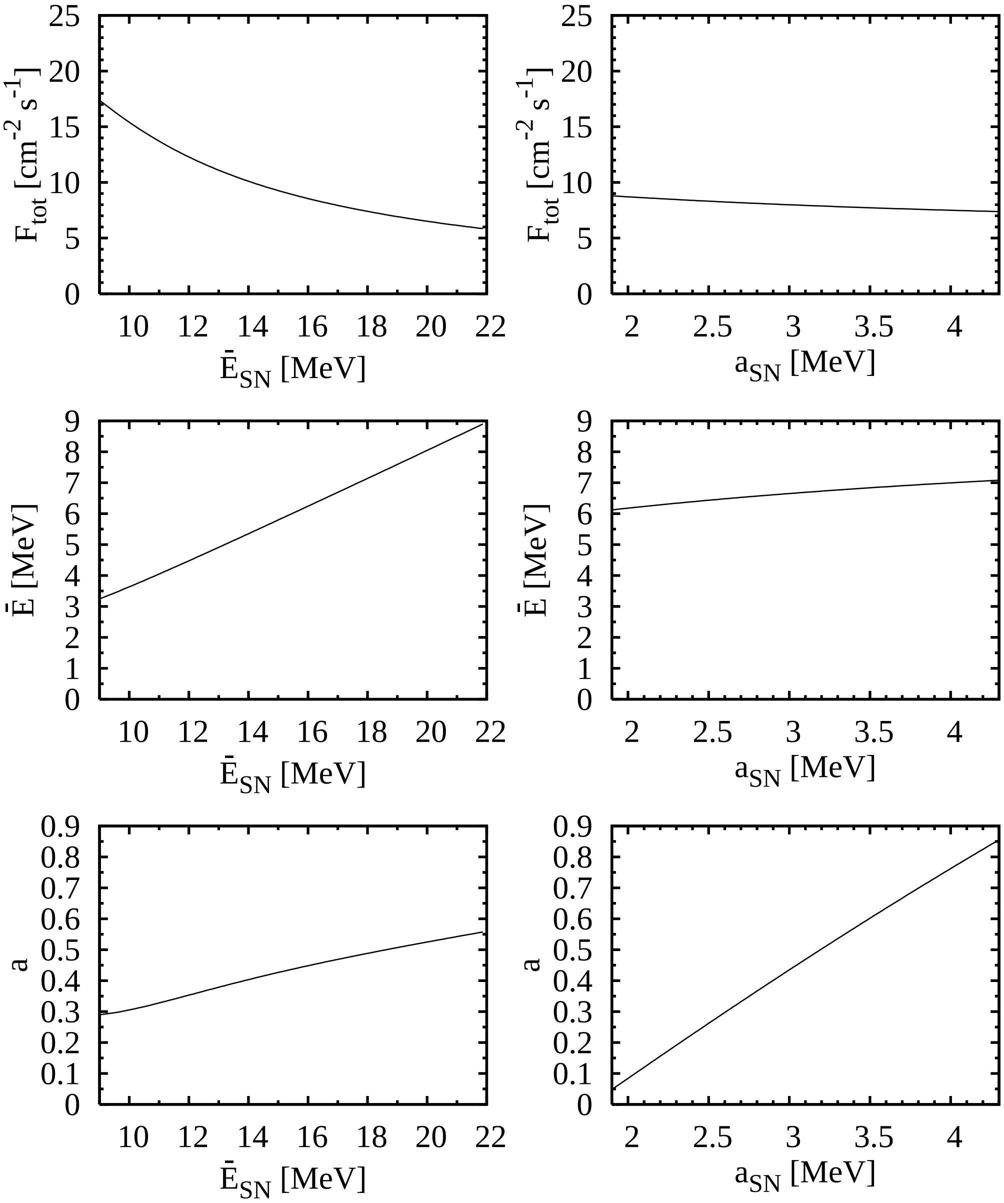

Figure 5.3: Same as Fig. 5.2, but for the mean energy $\overline{E}_{\rm SN}$ and pinching $a_{\rm SN}$.

Table 5.2: Dependence of DSNB fit parameters on input parameters.

	b_0	b_1	b_2
		β	
$F_{\mathrm{tot}}(\beta)$	7.919	6.034	1.986
$\overline{E}(\beta)$	6.693	-0.958	0.186
$a(\beta)$	0.469	-0.158	0.059
		α	
$F_{\mathrm{tot}}(\alpha)$	7.912	2.909	1.347
$\overline{E}(\alpha)$	6.691	-1.180	-0.282
$a(\alpha)$	0.469	-0.355	-0.062
		$\overline{E}_{\mathrm{SN}}$	
$F_{\mathrm{tot}}(\overline{E}_{\mathrm{SN}})$	7.762	-0.6367	0.06344
$\overline{E}(\overline{E}_{\mathrm{SN}})$	6.682	0.4481	0.00183
$a(\overline{E}_{\mathrm{SN}})$	0.467	0.0204	-0.00036
		a_{SN}	
$F_{\mathrm{tot}}(a_{\mathrm{SN}})$	7.935	-0.580	0.106
$\overline{E}(a_{\mathrm{SN}})$	6.690	0.395	-0.061
$a(a_{\mathrm{SN}})$	0.469	0.337	-0.012

the input parameters as

$$f_x(x) = b_0 + b_1(x - x_{\mathrm{b}}) + b_2(x - x_{\mathrm{b}})^2, \tag{5.10}$$

where f_x denotes F_{tot}, $\overline{E}$ or a and x is for β, α, $\overline{E}_{\mathrm{SN}}$ or a_{SN}. Moreover, x_{b} denotes the value of the parameter x for our baseline estimate. An approximation of the dependence of a function f on all parameters would then be

$$f(\beta, \alpha, \overline{E}_{\mathrm{SN}}, a_{\mathrm{SN}}) = \frac{1}{f_{\mathrm{b}}^3} f_\beta(\beta) f_\alpha(\alpha) f_{\overline{E}_{\mathrm{SN}}}(\overline{E}_{\mathrm{SN}}) f_{a_{\mathrm{SN}}}(a_{\mathrm{SN}}), \tag{5.11}$$

where f_{b} is the value of f for the baseline case. Equation (5.11) is based on the assumption that the function f factorizes in this way. However, this description has only nine coefficients, f_{b} and the linear and quadratic term for each input parameter. A full quadratic description, which allosw all mixed coefficients to assume any value, would have $3^4 = 81$ coefficients for each of the functions f. Some of these mixed coefficients might be different than the ones of Eq. (5.11). However, Eq. (5.11) is still a useful approximation.

The results of such a fit are displayed in Table 5.2. In order to estimate the importance of each coefficient more accurately, we can multiply it by half of the range in which the corresponding parameter varies. Doing so, the coefficients from $\Delta\overline{E}_{\rm SN}$ increase by a factor of about 6 in relation to the other coefficients, the ones from $(\Delta\overline{E}_{\rm SN})^2$ by a factor of about 6^2. The other input parameters vary by about the same amount, $\sim \pm 1$. It can be seen that the linear approximation is already meaningful. However, in some cases we observe a stronger quadratic dependence as in $F_{\rm tot}(\beta)$, $F_{\rm tot}(\alpha)$, $F_{\rm tot}(\overline{E}_{\rm SN})$, $\overline{E}(\alpha)$ and $a(\beta)$. It is especially remarkable that the dependence of $\overline{E}$ on the corresponding $\overline{E}_{\rm SN}$ is nicely linear as is the dependence of a on $a_{\rm SN}$. The convolution with the SN history does not affect these two parameters.

5.2 Discussion

As a further step, it seems desirable to display the dependence of the DSNB on the seven parameters, as is done in Figs. 5.4–5.5. We see that the DSNB peaks at about 5 MeV, while the spectral form is at least roughly thermal. If we use the SN 1987A best-fit mean energy of 9 MeV, as is displayed in Fig. 5.4, the high energy tail of the DSNB gets reduced drastically. Likewise, a large early SFR $\alpha = 1$ will greatly enhance the low energy flux of the DSNB, as shown in Fig. 5.5. This does not come as a surprise, since we assumed star formation to have started as early as $z_{\rm max} = 20$, such that the SFR will have been two orders of magnitude higher at $z = 20$ according to this parameterization. It seems natural to expect a high number of redshifted neutrinos from this scenario. If star formation started later, e.g. at $z = 5$, the low-energy part of the DSNB will be reduced as displayed in Fig. 5.5. However, the part of the spectrum that we will be able to observe (from $E \approx 9$ MeV on in the best case), is insensitive to the choice of $z_{\rm max}$ as long as $z_{\rm max} > 5$. The spectral pinching $a_{\rm SN}$ does not have a considerable influence on the DSNB, only the shape is altered a little, as in Fig. 5.5.

In summary, we can group some parameters together, according to their influence on the DSNB. There are parameters that show a dominant influence on the DSNB. These are the total energy emitted by a SN in $\bar{\nu}_e$ $E_{\rm tot}^{\rm SN}$, the local SN rate $R_{\rm SN}^0$, the recent SN history β and the mean energy of SN spectra $\overline{E}_{\rm SN}$. Two of them, $R_{\rm SN}^0$ and $E_{\rm tot}^{\rm SN}$ are naturally completely degenerate and might as well be treated as a single parameter, $E_{\rm tot}^{\rm SN} \times R_{\rm SN}^0$. Concerning the other two, β has a similar effect as $E_{\rm tot}^{\rm SN} \times R_{\rm SN}^0$, but also alters the DSNB mean energy $\overline{E}$, whereas $\overline{E}_{\rm SN}$ has a strong, linear impact on $\overline{E}$ and also alters $F_{\rm tot}$. In addition to these crucial parameters, there are also unimportant ones that have very little influence on the detectable DSNB. These are the early SN rate α and the spectral pinching $a_{\rm SN}$. The parameter α does change $F_{\rm tot}$ considerably, but this change is only due to the flux below 10 MeV, where the DSNB cannot be detected. Other than that, it has little influence on the detectable part of the DSNB. The a-parameter does not alter $F_{\rm tot}$ nor $\overline{E}$ considerably, only a to some extent. However, this impact is not very strong.

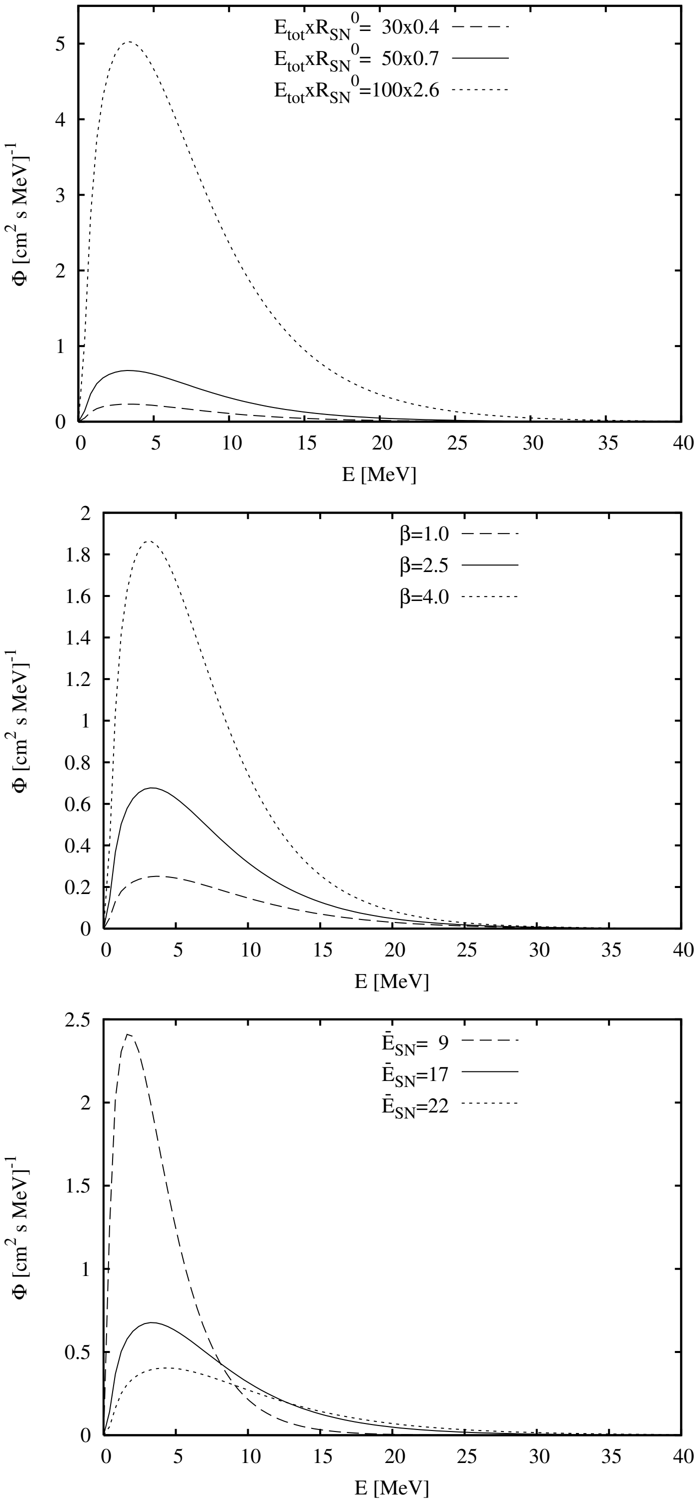

Figure 5.4: The DSNB for the indicated values of $R^0_{\rm SN}\times E^{\rm SN}_{\rm tot}$, β and $\overline{E}_{\rm SN}$. The solid line displays our baseline case defined in Eq. (5.5). Only the indicated parameter is varied in each panel.

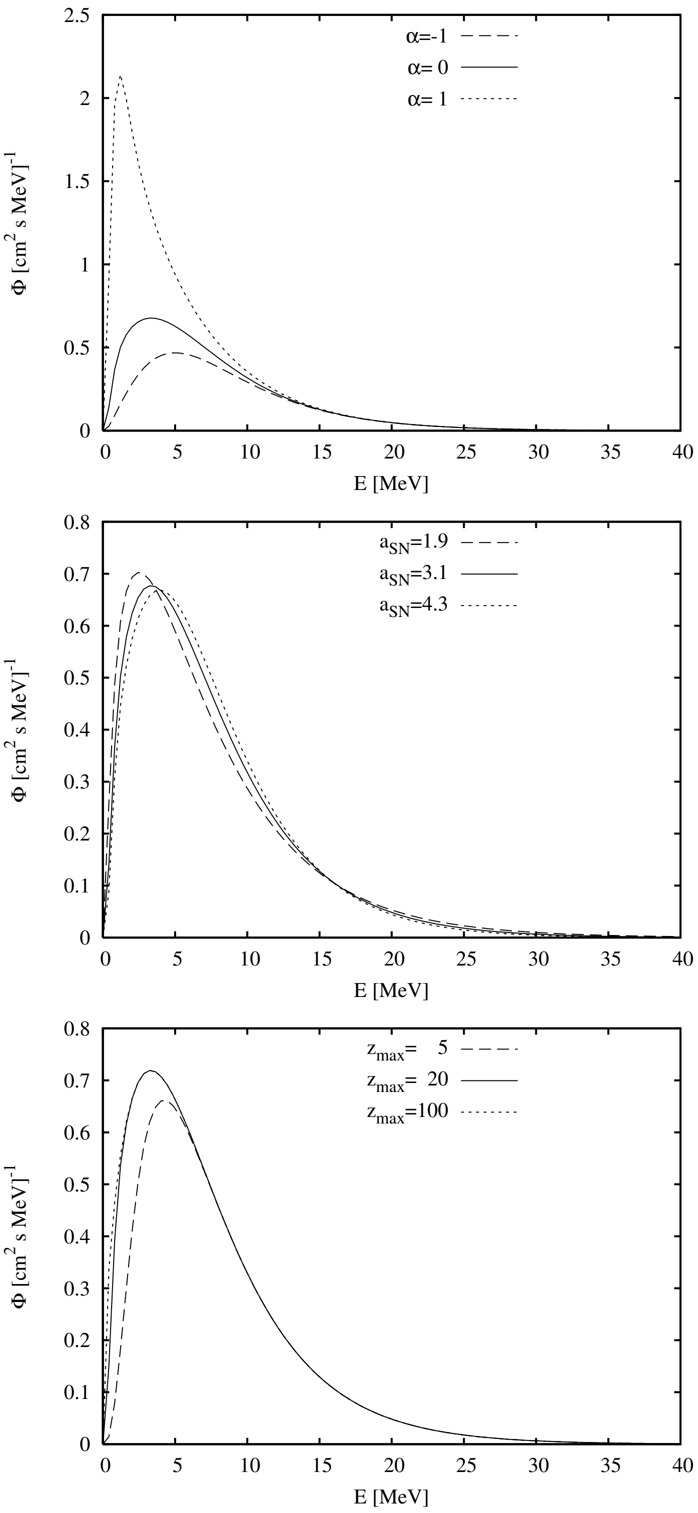

Figure 5.5: The DSNB for the indicated values of α, a and $z_{\max}$. The solid line displays our baseline case defined in Eq. (5.5). Only the indicated parameter is varied in each panel.

Finally there is one parameter which is completely unimportant, the onset of star formation $z_{\max}$. An unrealistically broad variation of $z_{\max}$ from 5–100 does not have any influence whatsoever on the DSNB above 8 MeV, which is the accessible energy range. Therefore we conclude that the detectable DSNB is completely insensitive to $z_{\max}$ and more generally to SNe at very high redshifts $z > 5$. We will not examine the influence of $z_{\max}$ any further but keep it fixed to $z_{\max} = 20$, a rather large value, but of no importance for our conclusions.

Chapter 6

Detectors

There exists a large variety of detectors for detecting both neutrinos and antineutrinos of all flavors. However, not all of them are and will be suitable to measure the DSNB, and this is mainly due to the fact that the expected flux is too low for most detectors and is also shielded by backgrounds. In fact, currently only the SK-detector expects a reasonable number of events per year (about 1–2 [7]), but these are shadowed by background from spallation and muon-induced electron events (Ref. [7] and also chapter 7 of this work). The detectability of the DSNB has been estimated for other detectors as well, such as the Sudbury Neutrino Observatory (SNO) [133] and the KamLAND experiment [6, 133]. The estimates are about 0.03 events in 17 MeV $\lesssim E_e \lesssim$ 23 MeV for SNO and 0.1 events per year in 10 MeV $\lesssim E_e \lesssim$ 23 MeV for KamLAND [133]. Recently, it has been pointed out that liquid argon detectors might be able to detect the DSNB in ν_e in the future [134]. The ICARUS detector which is currently under construction expects about 0.3 events per year in 16 MeV $< E_e <$ 40 MeV. However, since the backgrounds are very large and the expected event rates at SNO, KamLAND and the future ICARUS are extremely low, about one order of magnitude lower than at SK, we will concentrate our discussion on the detection at SK and future larger water Cherenkov detectors. Finally, we will present the recently proposed gadolinium trichloride ($GdCl_3$) detection technique.

6.1 Detection Reactions

The dominant neutrino interaction processes in water the charged-current reactions $\bar{\nu}_e p \to n e^+$, $\nu_e {}^{16}\mathrm{O} \to \mathrm{X}e^-$ and $\bar{\nu}_e {}^{16}\mathrm{O} \to \mathrm{X}e^+$ and elastic scattering $\nu_e e \to \nu_e e$. The inverse beta decay $\bar{\nu}_e p \to n e^+$ has been calculated accurately by Strumia and Vissani [135]. They give an analytic fit with energies in MeV,

$$\sigma(\bar{\nu}_e p) \approx 10^{-43} \times \mathrm{cm}^2 \; p_e E_e \; E_\nu^{-0.07056+0.02018 \ln E_\nu - 0.001953 (\ln E_\nu)^3}, \tag{6.1}$$

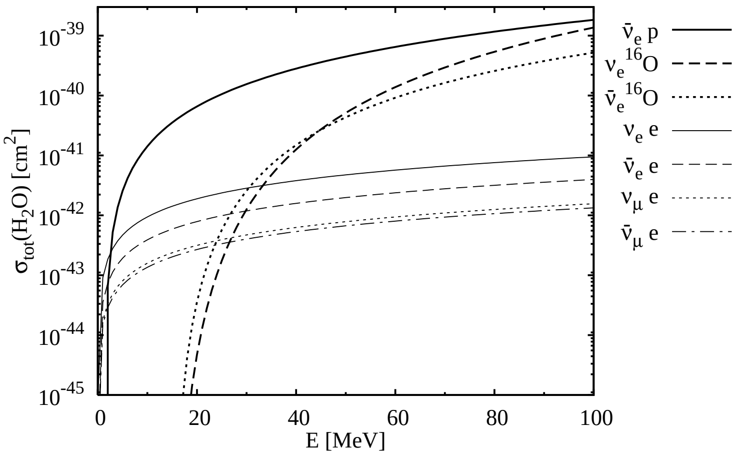

Figure 6.1: Cross sections for the detection of neutrinos in a water Cherenkov detector, according to Eqs. (6.1)–(6.3) and according to Eq. (10.17) in Ref. [34]. The curves are normalized to the situation in water, so that $\bar{\nu}_e p \to ne^+$ is multiplied by a factor 2 and the scattering on electrons by a factor 10.

which represents their calculation with deviations of a few per-mille for $E_\nu <$ 300 MeV. The energy of the outcoming positron is $E_e = E_\nu - (m_n - m_p) \approx E_\nu - 1.3$ MeV. Notably at high energies ($E_e > 50$ MeV), this cross section behaves differently from the simpler approximation $\sigma \approx 9.52 \times 10^{-43}$ cm^2 $p_e E_e$, which has often been used, for example in Ref. [136]. At $E_e = 100$ MeV, the simple approximation overestimates the cross section by a factor of about two. The cross sections for charged-current absorption of neutrinos and antineutrinos on oxygen have been tabulated by Kolbe, Langanke and Vogel [137]. The cross section is distributed among different final states X, notably ^{16}F for ν_e and ^{16}N for $\bar{\nu}_e$, but also two-particle states occur, like $\bar{\nu}_e{}^{16}\mathrm{O} \to \mathrm{X}e^+n$. Tomàs et al. [138] have fitted the total cross section for $\nu_e{}^{16}\mathrm{O} \to \mathrm{X}e^-$ as

$$\sigma(\nu_e{}^{16}\mathrm{O}) \approx 4.7 \times 10^{-40}\ \mathrm{cm}^2\ \left(E_\nu^{1/4} - 15^{1/4}\right)^6 , \tag{6.2}$$

where energies are in MeV. The fit agrees well with the tables for 25 MeV $< E_\nu <$ 100 MeV. We can use a similar fit for Kolbe et al. 's data on $\bar{\nu}_e{}^{16}\mathrm{O} \to \mathrm{X}e^+$ [139],

$$\sigma(\bar{\nu}_e^{16}\mathrm{O}) \approx 4.99 \times 10^{-40}\ \mathrm{cm}^2\ \left(E_\nu^{0.228657} - 15^{0.228657}\right)^{4.61335} , \tag{6.3}$$

where energies are in MeV. Cross sections for elastic scattering on electrons have been calculated and can be found in Ref. [34], chapter 10, for example.

Figure 6.1 shows the total cross sections for the different reactions. The curves are normalized to the cross section per water molecule H_2O, so scattering on protons has been multiplied by a factor of two and scattering on electrons by a factor of ten. We see that inverse beta decay is the dominant reaction in the relevant energy regime, while absorption on oxygen becomes comparable at higher energies $E > 50$ MeV. We conclude that in water, inverse beta decay is the only reaction that is sensitive to the DSNB, since expected events at SK are of the order of a few per year at most and backgrounds are high. Therefore scattering on oxygen is negligible for the DSNB, since it is more than one order of magnitude lower than inverse beta decay in the 0–50 MeV regime. However, for the calculation of backgrounds, notably atmospheric neutrinos which have a large flux at higher energies, scattering of both neutrinos and antineutrinos on oxygen has to be included, as is discussed in chapter 7.

6.2 Water Cherenkov Detectors

In water Cherenkov detectors, photomultiplier tubes detect the Cherenkov light of charged particles, notably electrons, positrons and muons. The position, direction and energy of the particle can be reconstructed to a certain accuracy by an analysis of the signal. In the case of the DSNB, positrons from $\bar{\nu}_e p$ can be detected.

The largest currently active detector of this kind is SK with a total volume of 50 kt pure water and a fiducial volume of 22.5 kt, located in the Kamioka Mine in Gifu, Japan. The energy resolution is 16% at 10 MeV and slightly better in the relevant range 10–40 MeV, whereas the triggering threshold is at 5 MeV. The SK-collaboration has recently analyzed 1496 days of data in the energy range 18 MeV $< E_e <$ 82 MeV and searched for DSNB candidates [12]. They found an upper limit of 2.8–3.5 events per year above the triggering threshold of 5 MeV, depending on different theoretical models of the DSNB. Moreover, they found an upper limit of 20–130 $\bar{\nu}_e$ cm^{-2} s^{-1} for the total DSNB and an upper limit of 1.2 $\bar{\nu}_e$ cm^{-2} s^{-1} for the DSNB above $E_\nu = 19.3$ MeV.

Future water Cherenkov detectors with fiducial volumes of the order of one megaton are planned, which might eventually detect the DSNB. An upgrade of SK, called Hyper-Kamiokande, is discussed at the Kamioka site with a fiducial volume of 1.150 Mton [140]. A new Underground Nucleon decay and Neutrino Observatory (UNO) has been proposed in the United States with a fiducial volume of 445 kton [141]. The UNO collaboration has not decided on a site yet, but several possibilities have been suggested and are examined. There are also efforts to build a megaton water Cherenkov detector in the Frejús tunnel close to the border between France and Italy [142]. Optimistic schedules for the three detectors foresee that they could be completed and start taking data in about 10 to 20 years.

6.3 Event Rates

The number of electron or positron events in a time interval τ and an energy window $E_1 < E_e < E_2$ is

$$N_e = N_p \tau \int_{E_1+\Delta}^{E_2+\Delta} \Phi(E_\nu)\sigma(E_\nu)\epsilon(E_\nu)dE_\nu, \tag{6.4}$$

where $N_p = n_p V_{\rm fid}$ is the number of protons in the detector, 1.5×10^{33} in SK, $\Delta = E_\nu - E_p$ is the energy difference between the incident neutrino and the outgoing lepton. We have assumed that Δ is fixed, which is a good assumption for inverse beta decay, where $\Delta = m_n - m_p = 1.3$ MeV. Moreover, $\epsilon(E_\nu)$ is the detection efficiency.

In order to make predictions about event rates at detectors, it seems to be a good approach to define a maximal and a minimal DSNB flux, restricted both by observations and theory. We assume all parameters of our model to be such that they give a maximal DSNB flux above 19.3 MeV, $R^0_{\rm SN} = 2.6\,10^{-4}\,{\rm yr}^{-1}\,{\rm Mpc}^{-3}$, $\beta = 4$, $E^{\rm SN}_{\rm tot} = 100\times10^{51}$ erg, $\overline{E}_{\rm SN} = 22$ MeV, $a_{\rm SN} = 4.3$. We can leave $\alpha = 0$ and $z_{\rm max} = 20$ since they do not influence the high-energy flux. Throughout this chapter, we will therefore keep $\alpha = 0$ and $z_{\rm max} = 20$. Using these somewhat extreme parameters, we obtain a flux of $5.9\ \bar{\nu}_e\ {\rm cm}^{-2}\ {\rm s}^{-1}$ above 19.3 MeV, which is a factor five higher than the SK limit in this energy range. It is not surprising that the SK observation already places constraints on our model, since we chose fairly broad parameter ranges. It has been pointed out before that the SK result can be used to constrain the local SFR and the slope of the SFR up to $z \approx 1$ [7, 143, 144]. However, these works did not allow for uncertainties in the SN neutrino spectrum. Notably the total neutrino energy $E^{\rm SN}_{\rm tot}$ is degenerate to the two SFR parameters and the constraints on $R^0_{\rm SN}$ and β only apply if $E^{\rm SN}_{\rm tot}$ is known.

A maximal DSNB flux of our model is thus constrained by the SK experiment. For a maximal case, we choose the relevant parameters to be between the baseline case and the maximally allowed value of the parameter, $R^0_{\rm SN} = 1.3 \times 10^{-4}\ {\rm yr}^{-1}\ {\rm Mpc}^{-3}$, $\beta = 3$, $E^{\rm SN}_{\rm tot} = 65 \times 10^{51}$ erg, $\overline{E}_{\rm SN} = 19$ MeV and $a = 2.5$. We obtain a flux of $1.17\ \bar{\nu}_e\ {\rm cm}^{-2}\ {\rm s}^{-1}$ which is compatible with the SK observation and can be viewed as the maximally allowed flux. On the other hand, the minimally allowed flux is not constrained by observations, only by the minimal values of our parameters $R^0_{\rm SN} = 0.4\ 10^{-4}\ {\rm yr}^{-1}\ {\rm Mpc}^{-3}$, $\beta = 1$, $E^{\rm SN}_{\rm tot} = 30 \times 10^{51}$ erg, $\overline{E}_{\rm SN} = 9$ MeV and $a_{\rm SN} = 4.3$. In Fig 6.2, we show the expected positron event rates for these minimum and maximum cases, along with the baseline case. The event rates differ considerably, by

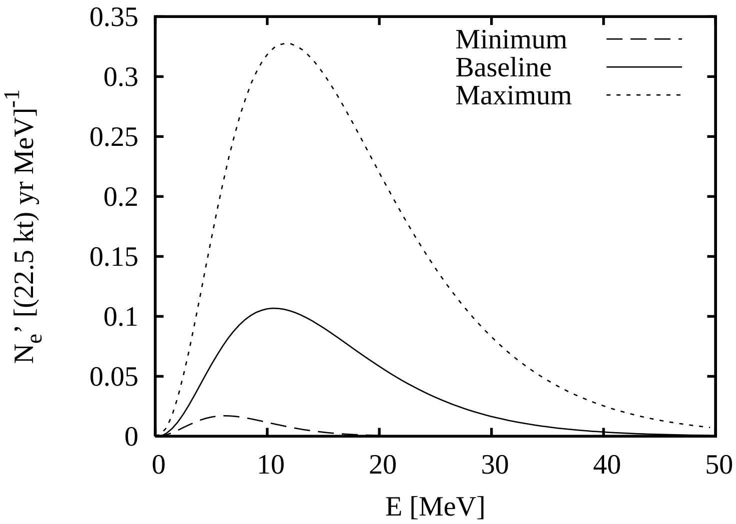

Figure 6.2: Event rates for extreme DSNB predictions. We show the minimally as well as the maximally allowed DSNB, along with the baseline case.

about one order of magnitude. This is due to the large range for our parameters and also to the very unlikely minimum case. The maximum case, however, is not as unlikely as the minimum case, since we do not exploit our full parameter range, but choose values between the baseline case and the maximum values. However, a low flux somewhere in between the baseline estimate and the minimum flux seems perfectly possible as well.

Table 6.1 shows fluxes and event rates for the different models, different energy windows and different detector volumes. Motivated by the SK search for the DSNB, we display positron events per year for this experiment, in particular we assume the same detection efficiency which SK obtained after applying several background reduction cuts. The efficiency was determined as 47% below 34 MeV and 79% above. The low efficiency at lower energies is due to the solar direction cut which removed events within a certain angle from the sun in order to reduce backgrounds from solar neutrinos. Moreover, we use the same lower energy threshold of 18 MeV as the SK search, which was determined by the ability to remove backgrounds from beta-unstable muon spallation products. To display an optimistic detection scenario, we also choose a megaton water Cherenkov detector with a fiducial volume of 445 kt (as UNO), full detection efficiency and an optimistic detection window of 8–40 MeV, which might be obtained by a detector that is far from nuclear reactors, like some UNO candidate sites imply. Total fluxes and positron events are also shown for comparison, even though they are not detectable. Below ~ 8 MeV, reactor $\bar{\nu}_e$ rise quickly and above ~ 40 MeV atmospheric ν_e and $\bar{\nu}_e$ become dominant so that at these energies the DSNB cannot be

Table 6.1: Fluxes and positron events for different models, different energy windows and detector volumes.

Energy window	Maximum case	Baseline case	Minimum case
Flux F [$\mathrm{cm}^{-2}\mathrm{s}^{-1}$]			
19.3–40 MeV	1.1	0.27	0.0022
9.3–40 MeV	6.3	1.9	0.15
Total	20.0	6.8	1.9
e^+ events for 1 yr SK			
18–40 MeV	2.1	0.33	0.0019
Total	4.6	1.0	0.079
e^+ events for 5 yrs UNO			
8–40 MeV	740	170	7.8
Total	890	210	17

detected. Additionally, in the window 18 to 50 MeV, decay electrons from muons are a large background, so that the SK collaboration could not distinguish any DSNB events from the background. We will discuss the different backgrounds in detail in chapter 7.

6.4 Gadolinium Trichloride Detection

Since the detection of the DSNB is hindered by backgrounds, it seems desirable to investigate possibilities to reduce these backgrounds. Beacom and Vagins [13] have proposed a new detection technique which uses $GdCl_3$ as a neutron absorber. They point out that backgrounds which are not induced by neutrinos themselves could be drastically reduced with the $GdCl_3$ method.

It would be ideal if one were able to detect the neutron that emerges in $\bar{\nu}_e p \to n e^+$ in coincidence with the positron. One could then distinguish these coincident positrons from background electrons or positrons, which do not have a coincident neutron, like backgrounds from spallation or muon-decay electrons. Neutrons quickly lose energy in water, notably by collisions with free protons. They finally reach thermal energies and are captured by protons and nuclei. Beacom and Vagins [13] propose to add 0.2% gadolinium (100 t) to the water in SK in order to enable neutron capture on gadolinium. Gadolinium has a cross section of 49×10^3 barn for thermal neutron capture, compared with 0.3 barn on free protons. Thus, 90% of the neutron captures would be on Gd. After thermalization, the capture on Gd would occur in about 20 μs and about 4 cm, approximately 10 times faster than in pure water. Gadolinium produces an 8 MeV gamma cascade upon neutron capture, which could be detected via electrons that are Compton scattered by these relatively hard gammas. Beacom and Vagins [13] simulated the gamma emission and Compton scattering process and found that the corresponding electron energy peaks at about 5 MeV and ranges from 3 to 8 MeV. The successor of SK-II, SK-III will trigger down to 3 MeV would therefore be able to detect the Compton-scattered electrons. This upgrade is scheduled to begin operation in 2006. Neutron coincidence detection with Gd would be especially efficient since the time separation between the positron event and the gamma-cascade induced electrons, which is about the time the neutron diffuses before it is captured, 20 μs, is exceedingly small compared to typical time separations of events at SK.

However, one has to take into account neutrons from other sources which could simulate this coincidence reaction and would act as a background. Neutrons can emerge from muon-induced spallation and from antineutrinos with very low energies, so that the positron is below the Cherenkov threshold. These low-energy $\bar{\nu}_e$ can come from nuclear reactors or decays U/Th in the earth, so-called "geo neutrinos". Additionally, neutrons can emerge from neutral-current reactions of atmospheric neutrinos and also from the decay of the radio active ^{152}Gd, which induces O(α,n) reactions. Beacom and Vagins [13] estimate that the rate of muon-induced spallation neutrons is about 10^5 per day. They argue that these neutrons can be rejected by requiring a very small time separation between the positron and the neutron event, so that they should not cause a problem. The neutron rates of other sources are much lower, less than one per day from reactor $\bar{\nu}_e$, about 4 per day from U/Th decay, about 2 per day from atmospheric neutrinos and about one per day from ^{152}Gd. Since these rates are orders of magnitude lower than the neutron rate from spallation, they do not place any background to the coincidence signal.

Beacom and Vagins [13] estimate that backgrounds from cosmic rays, notably muon-induced spallation and muon-decay electrons, can be reduced by a factor ~ 5 with the $GdCl_3$ technique. They also point out that further reduction might be possible by requiring a small position separation between the neutron and the positron. While we cannot detect the DSNB with SK currently, because it is shielded by muon-decay electrons, $GdCl_3$ might reduce both spallation and decay electrons, such that the DSNB can become visible at energies between 10 and 30 MeV.

Chapter 7

Backgrounds

Searching for the DSNB is a background-dominated experiment. It is crucial to understand the backgrounds well if we want to infer the DSNB from measurements. We are limiting our discussion of backgrounds to water Cherenkov detectors since these are the method of choice to detect the DSNB.

Backgrounds that produce a Cherenkov ring are $e^{\pm}$ and $\mu^{\pm}$ from other sources than the DSNB. Electrons and positrons are scattered more often than muons on their way through the detector, because they are much lighter. Thus the Cherenkov ring looks more diffuse than for muons. Additionally, for small energies, the Cherenkov angle of muons is considerably smaller than that of $e^{\pm}$ of the same energy. For instance, $\mu^{\pm}$ with $E_{\mathrm{kin}} < 140$ MeV have a Cherenkov angle $\theta_{\mathrm{C}} < 34°$, whereas $e^{\pm}$ with $E_{\mathrm{kin}} > 18$ MeV have $\theta_{\mathrm{C}} \approx 42°$. This angular difference has been exploited by the recent study of the SK collaboration in order to obtain an upper limit on the DSNB [12]. Therefore, Cherenkov light that comes directly from muons does not place a serious background to e^+ events from the DSNB and we will reduce our discussion to Cherenkov light from $e^{\pm}$-events. It makes sense to distinguish between $e^{\pm}$ that are induced directly by neutrinos from other sources than the DSNB and $e^{\pm}$ that arise as decay products of different particles, notably muons and beta-unstable spallation products. We will see that the "direct" neutrino backgrounds will remain irreducible while we will argue that backgrounds which are not directly neutrino induced might be reduced via the $\mathrm{GdCl_3}$ detection technique.

7.1 Neutrino Backgrounds

7.1.1 Atmospheric Neutrinos

Atmospheric neutrinos and antineutrinos have been a very important tool for inferring neutrino properties, notably oscillation parameters for flavor oscillation between ν_μ and ν_τ [1]. However, for the detection of the DSNB the very-low-energy tail of the atmospheric neutrinos acts as a background, since fluxes become comparable at energies of about 30 MeV. Atmospheric neutrinos emerge from the decay of cosmic-ray induced particles in the atmosphere, notably muons, pions and kaons. From these decay processes, one expects about the same number of particles and antiparticles of one flavor, but about twice as many muon as electron neutrinos and antineutrinos. Fluxes on earth are usually calculated via Monte Carlo simulations, including various effects like the flux of the primary cosmic rays, solar modulation, the geomagnetic field and others. However, since experiments focusing on atmospheric neutrinos are usually interested in the higher energy flux $E > 100$ MeV, codes are optimized for this regime and only few studies give results for energies lower than 100 MeV [145, 146, 147, 148]. Uncertainties in the low energy regime can therefore be as large as 30% [12].

Notably Gaisser et al. [146] give fluxes down to energies as low as 2 MeV, therefore this study is often adopted for DSNB evaluations [6, 7]. Recently, results from the 3D Monte Carlo code FLUKA on very low energy atmospheric neutrinos have been reported and made accessible [145]. These flux calculations extend down to energies as low as 15 MeV and are therefore appropriate for our purposes. Moreover, the 3D calculations are more likely to give realistic results than the older 1D codes. Therefore we adopted the values of the FLUKA study for our calculations. Results have been given for the Kamioka site and solar minimum as well as maximum. Comparing the FLUKA $\bar{\nu}_e$-flux with the fluxes obtained by Gaisser et al. [146], Barr et al. [147] and Honda et al. [148], we find that differences do not exceed 30%. In order to calculate event rates at SK, we need to include the reactions $\nu_e{}^{16}\mathrm{O} \to \mathrm{X}e^-$ and $\bar{\nu}_e{}^{16}\mathrm{O} \to \mathrm{X}e^+$, since these are important at higher energies. The threshold for these reactions is about $E_\nu = 15$ MeV for $\nu_e{}^{16}\mathrm{O} \to \mathrm{X}e^-$ and about $E_\nu = 11$ MeV for $\bar{\nu}_e{}^{16}\mathrm{O} \to \mathrm{X}e^+$ absorption of ν_e and $\bar{\nu}_e$. For an accurate calculation of event rates, we would need the differential distribution of the final-state $e^\pm$. However, for simplicity, we assume that all $e^\pm$ have the energy $E_e = E_\nu - E_{\mathrm{th}}$, where E_{th} is about 15 and 11 MeV, respectively, for the two reactions. Figure 7.1 shows the fluxes obtained by the FLUKA code and our calculation of the event rate, using Eqs. (6.1)–(6.4). For the $\bar{\nu}_e$-flux, we take the mean of solar maximum and minimum, which differ by a few percent. For the ν_e event rates, we use the $\bar{\nu}_e$-flux, which is a valid approximation, since the ν_e and $\bar{\nu}_e$ fluxes differ by less than 5%. For simplicity, we assume full detection efficiencies. We see that at energies $E_e > 50$ MeV, absorption of ν_e on $^{16}\mathrm{O}$ dominates. For $E_e > 80$ MeV, absorption on $^{16}\mathrm{O}$ becomes the main process for $\bar{\nu}_e$ as well. We find that for 12 MeV $< E_e <$ 82 MeV, which is the analysis window of the SK-report [12], our calculations give about 13 events from atmospheric ν_e and $\bar{\nu}_e$ per year and 22.5 kt, of which about six are from $\nu_e{}^{16}\mathrm{O} \to \mathrm{X}e^-$, about four from $\bar{\nu}_e p \to n e^+$ and about three from $\bar{\nu}_e{}^{16}\mathrm{O} \to \mathrm{X}e^+$, where we

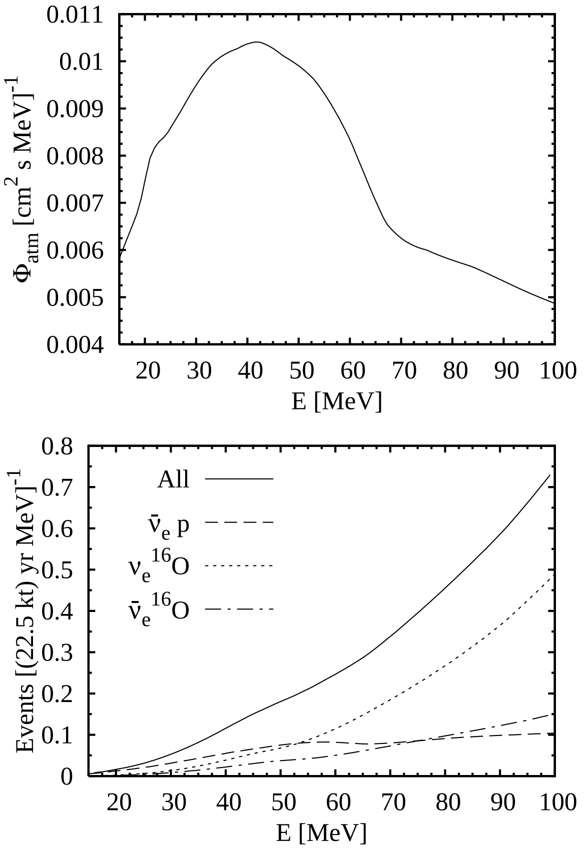

Figure 7.1: Atmospheric neutrinos. *Upper panel*: atmospheric $\bar{\nu}_e$-flux at the Kamioka site, mean of solar maximum and solar minimum. *Lower panel*: event rate from the indicated detection reactions at SK.

have assumed full efficiencies[1]. The atmospheric neutrino flux becomes comparable to our baseline case of the DSNB and dominates over 30 MeV. Thus, it is a serious background for the DSNB detection.

7.1.2 Reactor Antineutrinos

Reactor antineutrinos are produced in nuclear reactors due to the fission of radioactive uranium and its daughter products. The significant process is β-

[1]For the full exposure time of the SK search [12] of 1496 days, we obtain around 40 events from atmospheric neutrinos and antineutrinos, if we assume an efficiency of 47% below 34 MeV and 79% above. The SK-collaboration reports a best-fit to the data of 88 ± 12 events for the same exposure time and efficiencies. They also conducted a Monte Carlo analysis of expected events and found that they expect 75 ± 23 events. Thus there is a discrepancy of about a factor two in our results and the SK reports. The reasons for this are unknown and currently being discussed [149]. For consistency, we use our result.

decay. The fluxes from the different isotopes peak at very low energies, but for the DSNB, the reactor antineutrinos will be a background up to energies of 10–12 MeV or even higher. Vogel and Engel [150] have presented an analytic fit for the shapes of antineutrino spectra from the five relevant isotopes ^{235}U, ^{239}Pu, ^{238}U, ^{241}Pu and ^{252}Cf, normalized to $\bar{\nu}_e$/(MeV and fission). The fit describes the spectra well up to 8 MeV, but seriously overestimates them at energies higher than that. The only published study that has measured $\bar{\nu}_e$ spectra well above 8 MeV, until 12 MeV, is an experiment conducted by Tengblad et al. [151], determining the fluxes from ^{235}U, ^{238}U and ^{239}Pu. The contribution of the individual isotopes to the total power is dependent on how much time has passed since the start of the reactor period, since ^{235}U gets consumed and the daughter products ^{239}Pu and ^{241}Pu emerge. Ando and Sato [7] have claimed that a good mean value would be to assume $\sim$ 75% for ^{235}U, $\sim$ 15% for ^{239}Pu, $\sim$ 7% for ^{238}U and $\sim$ 3% for ^{241}Pu, while the contribution of ^{252}Cf is negligible. In reality, reactor antineutrinos originate from different reactors that are in different burning phases, so that there might be time-dependent variations in the antineutrino flux. These will not be very large though, since the spectra are very similar in shape. The total flux at the SK site has been estimated by Bemporad et al. [136] to be 1.34×10^6 $\bar{\nu}_e$ cm^{-2} s^{-1}.

Since the reactor neutrino spectra display a change at 8 MeV, we choose to fit them in two regimes, below and above 8 MeV. Below 8 MeV, we take Vogel and Engel's [150] analytic fit and normalize it to Bemporad's total flux, after weighing the individual isotopes. We do not take into account 6252Cf and ^{241}Pu since they do not contribute significantly to fission power. We fit the emerging sum to an exponential of a second order polynomial, obtaining

$$\Phi_{\mathrm{reactor,low}} = \exp(14.38 - 0.1708 E_{\bar{\nu}_e} - 0.09069 E_{\bar{\nu}_e}^2)\ \mathrm{cm}^{-2}\ \mathrm{s}^{-1}\ \mathrm{MeV}^{-1}, \quad (7.1)$$

where $E_{\bar{\nu}_e}$ is given in MeV. Above 8 MeV, we weigh Tengblad's fluxes to $\bar{\nu}_e$ per MeV and fission, using the total number of $\bar{\nu}_e$ per fission above 1.8 MeV according to Huber and Schwetz [152], since Tengblad et al. give their values normalized to unity. Huber and Schwetz obtain 1.92(±1.9%) $\bar{\nu}_e$ per fission for ^{235}U, 2.38(±2.0%) for ^{238}U and 1.45(±2.1%) for ^{239}Pu. Summing the fluxes from the three relevant isotopes, we normalize the sum to the total flux, using the full spectral shape of Tengblad's measurement. We fit the resulting spectrum to an exponential of a third order polynomial, obtaining

$$\Phi_{\mathrm{reactor,high}} = \exp(359.4 - 105.2 E_{\bar{\nu}_e} + 10.42 E_{\bar{\nu}_e}^2 - 0.3483 E_{\bar{\nu}_e}^3)\ \mathrm{cm}^{-2}\mathrm{s}^{-1}\mathrm{MeV}^{-1}, \quad (7.2)$$

where $E_{\bar{\nu}_e}$ is given in MeV. It turns out that the difference between Vogel and Engel's analytic fit and the measurements amounts to one order of magnitude above 8 MeV, and even more above 11.5 MeV, where the antineutrino flux

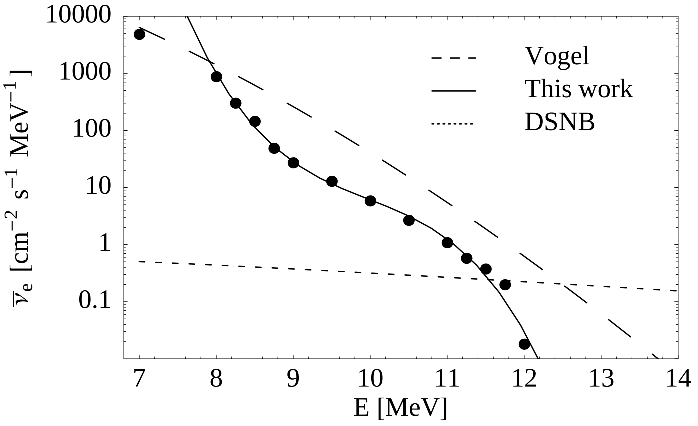

Figure 7.2: Reactor $\bar{\nu}_e$ flux at SK. The dashed line is Vogel and Engel's analytic fit [150], the solid line is our fit, the points are measurements from Tengblad et al. [151], the dotted line is the DSNB flux for our baseline model. Errors for Tenglad et al.'s measurement are in the range of 10–20% between 7 and 8 MeV and 40–50% above 8 MeV.

drops drastically, as can be seen in Fig. 7.2. Thus, if one uses Vogel's analytic fit, as has been done in the literature [7], one overestimates the influence of reactor $\bar{\nu}_e$. More specifically, the energy at which reactor $\bar{\nu}_e$ fluxes and the DSNB are equal is about one MeV higher with Vogel's fit than with Tengblad et al.'s experimental results.

In summary, we have analyzed the reactor $\bar{\nu}_e$ flux rather accurately. This is necessary because there are no detailed studies of this flux at such high energies, except for Tengblad et al.'s measurement. If $GdCl_3$ will finally enable us to detect the DSNB at energies as low as the reactor $\bar{\nu}_e$, we need precise information about this flux. We predict that at SK, reactor neutrinos will not cause a problem for the detection of the DSNB at energies as low as 11 or 12 MeV, which corresponds to positron energies of about 10 to 11 MeV. Moreover, since the reactor $\bar{\nu}_e$ flux depends strongly on the distance to the closest nuclear reactors, one might think about detector sites which are less affected by this background. Specifically, this would be the case if UNO was built in a region in the U.S. that is far from reactors, as are large parts of central North America. The distance from the Henderson mine in Colorado, which has been proposed as a future detector site for UNO, to the closest reactors is about a factor 4 or 5 larger than at the SK site. This would lower the $\bar{\nu}_e$ background by a factor of about 20, which in turn would enable us to detect the DSNB at positron energies of about 8 or 9 MeV. Of course, these considerations only apply if we are able to remove other backgrounds at low energies, notably spallation. However, there is hope that detection with $GdCl_3$ will finally be able to achieve this goal.

7.1.3 Solar Neutrinos

Solar neutrinos are a background to the DSNB at $E_\nu < 19$ MeV, notably from the *hep* and the ^{8}B process. The *hep* flux is three to four orders of magnitude higher than the DSNB below 19 MeV and the ^{8}B flux rises even higher than *hep* below 15 MeV, to fluxes of $\sim 10^5$ cm^{-2} s^{-1} MeV^{-1}. Even though the cross section for $\nu_e e^-$ scattering is two orders of magnitude lower, solar neutrinos will yield a much higher signal than the DSNB. However, recoil electrons from scattering with solar neutrinos are strongly peaked in the direction opposite to the sun so that it is easier to reduce this background. Currently, solar neutrinos are not a problematic background, since there is a different background that is much higher at $E_\nu < 19$ MeV, spallation products from cosmic-ray muons, which makes this energy range entirely inaccessible. If we are able to reduce spallation by $GdCl_3$ detection, we will also be able to reduce the solar neutrino background to some extent, since they do not produce neutrons which can be tagged by Gd. Therefore, the ability to remove this background depends on many factors, in the best case we might hope that it can be removed down to the reactor antineutrino threshold of $E_\nu \approx 11$ MeV. Ando et al. [133] point out that SK expects about 10^3 events from solar neutrinos per year. In addition, they claim that 99.98% of these background events can be removed if events within 25° from the sun are rejected. That would correspond to 0.2 remaining events per year which is lower than the expectations for the DSNB.

7.2 Other Backgrounds

7.2.1 Electrons and Positrons from Decaying Muons

Muons in general decay into electrons and positrons. Muons that originate from cosmic rays have kinetic energies above 140 MeV and produce a veto signal in the outer detector of SK, by which the corresponding decay event can be identified. However, atmospheric ν_μ can produce muons in the inner detector via charged current quasi elastic scattering ($\nu_\mu N \rightarrow \mu N'$). These low energy muons will stop in SK and produce a decay electron. If the decaying muon has a kinetic energy $E_{\mathrm{kin}} > 50$ MeV ($E_{\mathrm{total}} > 158$ MeV), it will produce a Cherenkov ring before decay and the Cherenkov light from muon and electron/positron will be found in the same event. Such events can be distinguished from pure electron/positron events and can be removed, as has been done by the SK collaboration in their search for the DSNB [12].

However, decay electrons/positrons from muons below the Cherenkov threshold $E_{\mathrm{kin}} < 50$ MeV are not distinguishable from genuine neutrino events, and are therefore an irreducible background at SK. It is possible to determine the expected event rate from such muons by taking into account the atmospheric ν_μ flux at low energies, oscillations into ν_τ, the cross section for charged current quasi elastic scattering on nuclei and finally the energy distribution of electrons from decaying muons at rest. Because of their low kinetic energies, they will stop in SK and lose practically all of their kinetic energy before decaying. The spectral shape of such a distribution is called Michel-spectrum [153] and reads

$$N' = \frac{G_\mathrm{F}^2}{12\pi^3} m_\mu^2 E_e^2 \left(3 - \frac{4E_e}{m_\mu}\right), \tag{7.3}$$

where G_F is the Fermi constant, m_μ the muon mass, E_e the electron energy, and the decay is assumed to be at rest, which is a good approximation, since these low-energy muons lose much of their kinetic energy while passing the detector. This equation is valid for $E_e < \frac{1}{2} m_\mu \approx 53$ MeV, the maximum energy of decay electrons. However, due to the finite energy resolution of SK, such events might be detected up to ~ 65 MeV as has been pointed out by the SK collaboration [12]. Therefore the decay $e^\pm$ spectrum will not end as sharply as expected from Eq. (7.3) and the cutoff at $\frac{1}{2} m_\mu$. The SK study of the DSNB upper limit has obtained a best fit of 174 ± 16 decay electron events in the energy range 18–82 MeV, for a time of 1496 days. This is consistent with their Monte Carlo study of the expected events, which yields 145 ± 43 events. An earlier report of the SK collaboration has estimated about 100 events in a time of 1258 days of data taking [133]. The experimental best fit, the Monte Carlo simulation and the earlier estimate based on different data are consistent with each other within uncertainties of about 30%. Thus, there are an order of magnitude more events in the energy range above 18 MeV from Michel electrons than are expected from the DSNB, hindering the detection. However, there is hope that detection with $GdCl_3$ will be able to reduce this background by a factor of at least ~ 5, as has been claimed by Beacom and Vagins [13]. In our analysis, we will use the shape of the Michel spectrum for decay electrons, normalized to SK's best fit.

7.2.2 Spallation Products from Muons

Another serious background is spallation by cosmic ray muons. These particles have energies that are sufficient to split nuclei, notably oxygen, whose daughter products are often unstable and emit $\beta^\pm$ radiation. According to Ando et al. [133], roughly 200,000 events are expected at SK per year. However, it is possible to reduce some of this background by using a likelihood function cut, as has been done in the search for solar neutrinos [154]. Moreover, one can reject events that occur within a fixed time after a cosmic ray muon in the outer detector, as has been done by the SK DSNB search for

0.15 μs. They found that there were no discernible spallation events left above 18 MeV, which determined the lower analysis threshold for this experiment. Spallation is in this respect perhaps the most serious background, since the ability to remove it defines the lowest energy for the data analysis. If at all, we will only be able to probe the high energy tail of the DSNB and thus a lower energy threshold will be crucial for the detection and can greatly enhance statistics.

It is hard to quantify the spallation events that cannot be removed currently, let alone find an analytic description. The SK collaboration does not present an analysis of the remaining events, thus an estimate is difficult to obtain. At most, we can hope that $GdCl_3$ will reduce backgrounds by the proposed factor 5. The Kamiokande-II collaboration has reported results for spallation events up to about 16 MeV in their search for solar neutrinos [155]. Considering the spectrum of possible spallation events that could not be rejected by the cuts, we find that this spectrum falls steeply by about two orders of magnitude from 10 to 16 MeV. Based on these results from Kamiokande-II, we can estimate that the $GdCl_3$ technique might enable the SK collaboration to set the analysis threshold from 18 MeV down to about 16 MeV or even lower. It is unlikely that this detection technique will be able to reduce spallation down to the reactor $\bar{\nu}_e$ threshold in the first years. However, it is possible that the technique will develop and this ultimate goal can be reached.

To summarize the discussion of this chapter, we display the event rates from the different backgrounds along with the DSNB in Fig. 7.3. We do not show the solar neutrinos and the spallation events since it is hard to quantify how many of these events would remain after reduction cuts. However, we show the current analysis threshold of 18 MeV, that SK has chosen due to spallation events. It is obvious that even for a high assumed DSNB, there is no detection window currently. There is hope that $GdCl_3$ might be able to open a detection window below 30 MeV, therefore we display this possibility in Fig. 7.4. We show the baseline and the maximum case for the DSNB, according to chapter 6.3. Moreover, we show the backgrounds as in Fig. 7.3, but with an event rate from sub-Cherenkov muons that is reduced by a factor five. It is hard to estimate how much the analysis threshold due to spallation can be pushed downwards by $GdCl_3$, but a rough estimate would be somewhere between 12 and 16 MeV. Assuming such a threshold, we can see that in the baseline case, we will already see some DSNB events that are not shielded by sub-Cherenkov muons. In the maximum case we would naturally see much more events.

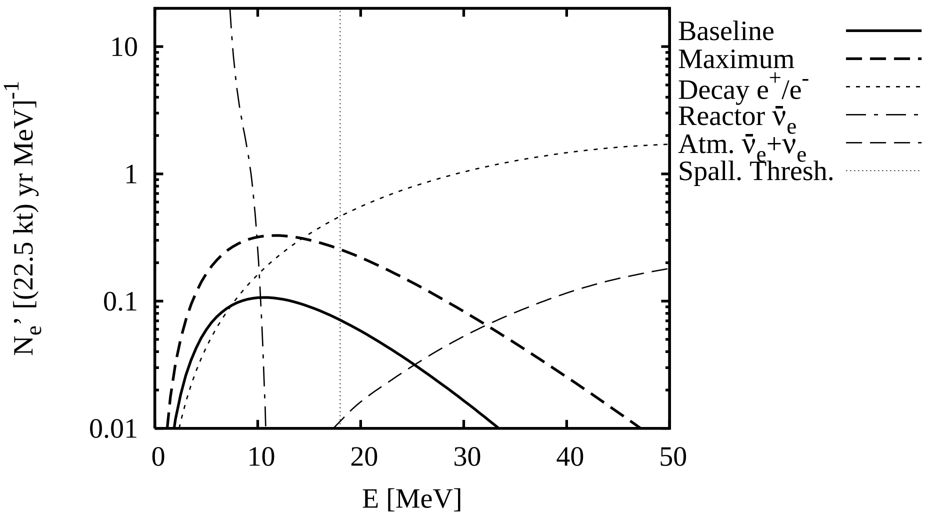

Figure 7.3: Event rates from the DSNB and backgrounds. For the DSNB, we show the baseline case and the maximum case from chapter 6.3. The analysis threshold set by the SK collaboration [12] is shown as a thin dotted line. Backrounds include decay $e^{\pm}$ from sub-Cherenkov muons and atmospheric as well as reactor neutrinos.

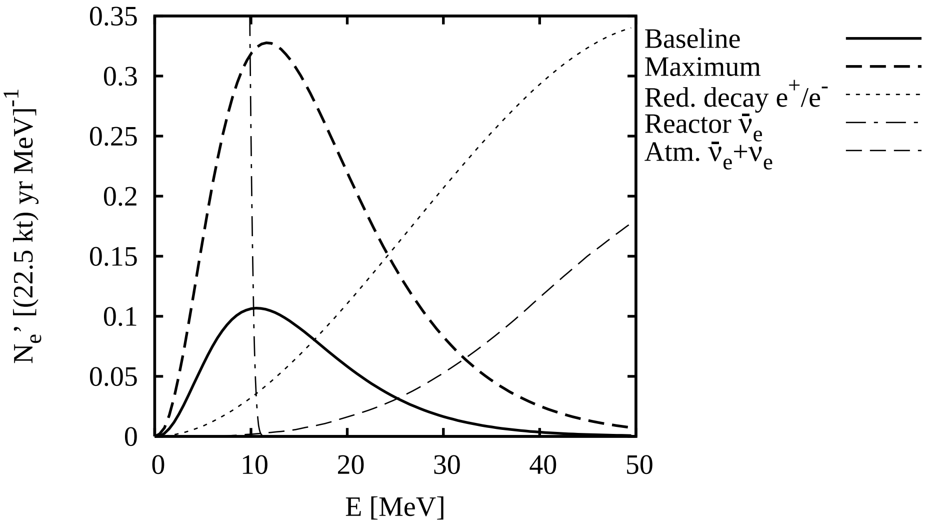

Figure 7.4: The background situation in the future. We show the backgrounds and DSNB cases from Fig. 7.3, except for the muon-induced decay $e^{\pm}$ which are reduced by a factor five to show the possible $GdCl_3$ performance.

Chapter 8

Results and Discussion

8.1 Constraining the Supernova History

We have discussed the detectability and analyzed in detail how input parameters will change the detectable DSNB. However, one can revert the point of view and ask what a possible detection of the DSNB might imply for the input parameters. Fukugita and Kawasaki [143] have placed constraints on the star formation history, using the DSNB upper limit of the SK collaboration [12]. Their limit corresponds to $R^0_{\rm SN} < 3.6 \times 10^{-4}$ yr^{-1} Mpc^{-3}. Ando and Sato [7] have analyzed the implication of the DSNB for the star formation history by conducting a Monte Carlo simulation for SK and megaton detectors. For 5 years of megaton detector performance, they predicted an accuracy of $\pm 0.4 \times 10^{-4}$ yr^{-1} Mpc^{-3} for $R^0_{\rm SN}$ if β is known exactly and ± 0.2 for β if $R^0_{\rm SN}$ is known. However, these predictions only apply if also the SN neutrino spectra are known very accurately and in reality, the situation is more complicated.

8.1.1 Local Supernova Rate

The influence of the local SN rate $R^0_{\rm SN}$ is degenerate with the recent SN history β and also the total neutrino luminosity $E^{\rm SN}_{\rm tot}$, as is displayed in Fig. 8.1. More specifically, $R^0_{\rm SN} = 0.4$ corresponds to Cappellaro's lower limit [83] and $R^0_{\rm SN} = 2.6$ is the assumed upper limit from Strolger [82] for large dust extinction. In the following Figs. 8.1–8.4, only the indicated parameter is varied, the others are fixed according to our baseline case Eq. (5.5). Backgrounds from reactor $\bar{\nu}_e$ and atmospheric ν_e and $\bar{\nu}_e$ are also shown. We treat $E^{\rm SN}_{\rm tot} \times R^0_{\rm SN}$ as a single parameter in Fig. 8.1. However, the extreme case of $E^{\rm SN}_{\rm tot} \times R^0_{\rm SN} = 100 \times 2.6$ is already excluded by SK's upper limit of 1.2 $\bar{\nu}_e$ cm^{-2} s-1 above 19.3 MeV [12], since this scenario would give a flux of 2.09 $\bar{\nu}_e$ cm^{-2} s^{-1} above 19.3 MeV. Therefore, we adopt values of $E^{\rm SN}_{\rm tot} \times R^0_{\rm SN} = 80 \times 1.8$ for our upper case, which gives a flux of 1.15 $\bar{\nu}_e$ cm^{-2} s^{-1}

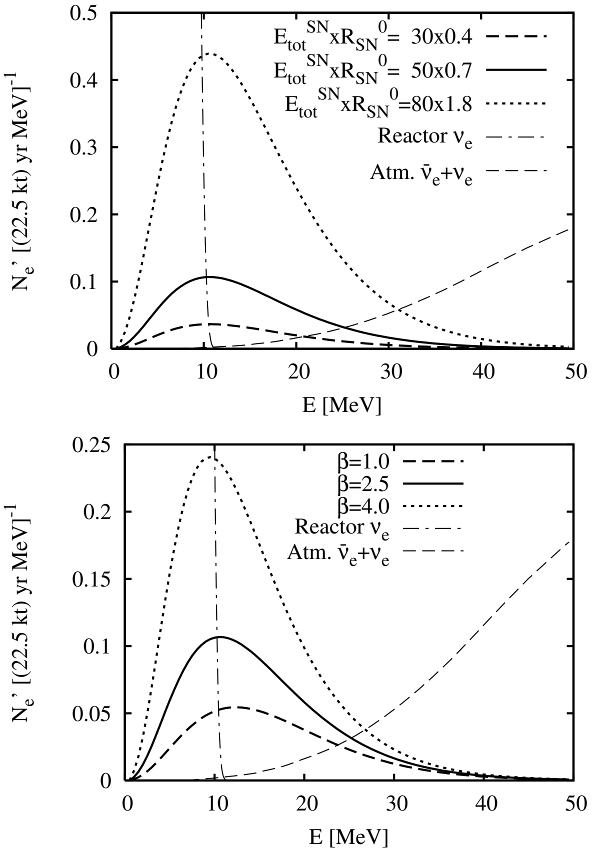

Figure 8.1: Event rates of the DSNB at SK for different parameters, the global influence of the local SN rate R^0_{SN} times the total neutrino energy $E^{\mathrm{SN}}_{\mathrm{tot}}$ (upper panel) and the recent SN history β (lower panel). Only the indicated parameters are varied, the others are fixed according to our baseline case. Backgrounds from reactor $\bar{\nu}_e$ (dash-dotted line) and atmospheric ν_e and $\bar{\nu}_e$ (long-dashed line) are also shown.

above 19.3 MeV and is consistent with the SK result. However, the choices of the other parameters are still consistent with the SK limit, if only one parameter is varied and the others kept fixed at the baseline case. From the total number of events in the detection window N_{w}, we will be able to constrain the values of R^0_{SN}, β and $E^{\mathrm{SN}}_{\mathrm{tot}}$ to a surface in the three-parameter space. The dependence of N_{w} on R^0_{SN} and $E^{\mathrm{SN}}_{\mathrm{tot}}$ is linear, whereas it is quadratic in β. Even if we have little knowledge about β and $E^{\mathrm{SN}}_{\mathrm{tot}}$, we will be able to place some upper and lower bound on R^0_{SN}. These bounds will possibly be able to exclude some extreme assumptions on R^0_{SN}. Notably for a low local SN rate as favored by Cappellaro et al. [83], we will be able to exclude $R^0_{\mathrm{SN}} > 5 \times 10^{-4}$ yr^{-1} Mpc^{-3}. With more knowledge of $E^{\mathrm{SN}}_{\mathrm{tot}}$, β or both of them, a more accurate determination of $R^0_{\rm SN}$ will be possible. A future galactic SN would provide us with a direct measurement of $E^{\rm SN}_{\rm tot}$ with very high statistics of about $10,000$ expected events at SK. The accuracy could well be in the range of 1–5%, and we would thus know $E^{\rm SN}_{\rm tot}$ far better than $R^0_{\rm SN}$ and β. In the absence of a galactic SN, information about $E^{\rm SN}_{\rm tot}$ will not be easy to obtain. Simulations could specify the ratio of total energies $E^0_{{\rm tot},\bar\nu_{\rm e}} : E^0_{{\rm tot},\bar\nu_{\rm x}}$ more exactly, insight about the equation of state inside a neutron star would place constraints on the total binding energy and determining the neutrino mass hierarchy as well as the mixing angle θ_{13} would be necessary to specify the influence of oscillations if luminosities are different between $\bar\nu_e$ and $\bar\nu_x$. Improved measurements of the SFR, notably using the cosmic spectrum will be able to constrain β, for which we assumed a fairly broad parameter range. Recent results point towards a more accurate determination of $\beta = 2$–3.5 [156, 157]. If we know $E^{\rm SN}_{\rm tot}$ exactly and β to $\sim 25\%$ accuracy, the DSNB will determine $R^0_{\rm SN}$ to $\sim 25\%$ accuracy, which is better than Cappellaro's determination and, more importantly, not affected by dust extinction. The fact that the DSNB is the only observable currently placing an *upper* bound on the star formation history makes it an indispensable alternative to other tracers.

8.1.2 Recent Supernova History

Naturally, similar considerations apply to the recent SN or star formation history β, also displayed in Fig. 8.1. Here, $\beta = 1.0$ corresponds to a shallow evolution of the SFR until $z = 1$, as favored by Lanzetta et al. [128] and $\beta = 4.0$ describes a steep evolution of the SFR, as proposed by Lilly et al. [108]. If we assume $\beta = 2.5$ and take into account uncertainties in $E^{\rm SN}_{\rm tot}$ and $R^0_{\rm SN}$, the DSNB detection will place a constraint of about $1 \lesssim \beta \lesssim 6$, confirming star formation and SN rate observations. The local SN rate might be determined more accurately by SN surveys, however, one always has to take into account corrections for dust extinction. If we assume that future observations will determine $R^0_{\rm SN}$ to an accuracy of $\sim 30\%$ and that a future galactic SN will provide us with knowledge about $E^{\rm SN}_{\rm tot}$, then the DSNB will also enable us to determine β with an accuracy of about 30% which is comparable with Hogg's assumed 1σ deviation of 2.7 ± 0.7. However, the caveat remains that determinations of $R^0_{\rm SN}$ have to deal with dust extinction and have to be treated as lower limits rather than exact measurements.

8.1.3 Early Supernova History

Contrary to what the previous literature has assumed [6, 7], the DSNB is not very sensitive to the early SN history α, as can be seen in Fig. 8.2. We display the case of a decline in the SFR at high redshifts, $\alpha = -1$, as favored

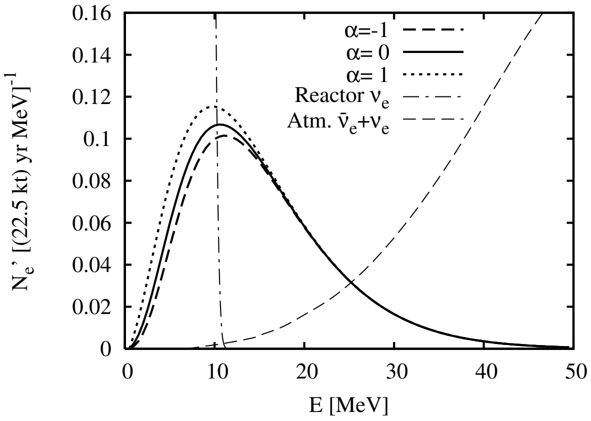

Figure 8.2: Event rates of the DSNB at SK for different values of α.

by the Madau-SFR [8]. Moreover, we display the possibility of a rising SFR at high redshifts $\alpha = 1$, as proposed by Lanzetta et al. [128]. We will not be able to infer α from its influence on $F_{\rm tot}$ or $\overline{E}$, since other parameters show a much stronger influence on these. However, α alters the pinching parameter a, which is only altered that strongly by the pinching parameter $a_{\rm SN}$ of the initial SN neutrino spectrum, and also by β to some extent. A significant determination of a will only be possible with high statistics, like 5-10 years of detection with a megaton water Cherenkov detector using $GdCl_3$. In this case, we will be able to place constraints on $a_{\rm SN}$, α and β in the form of a surface in the 3-parameter space, possibly confirming results for α from star formation rate observations. In the case of a galactic SN or progress in SN simulations, a might be known more accurately. If in addition, SFR observations or the DSNB itself place tighter constraints on β, we might well be able to infer the early star formation history α more accurately. More precisely if α is 0 and we know $\beta = 2$–3 and $a = 3.0 \pm 0.2$, then the DSNB will be able to place a constraint of about $-1 \lesssim \alpha \lesssim 1$, confirming SFR observations. However, due to the uncertainties in the other parameters and its small influence on the detectable DSNB, we conclude that the observation of α via the DSNB is actually not promising.

8.2 Constraining Supernova Neutrino Spectra

8.2.1 Total Neutrino Luminosity

The total energy $E_{\rm tot}^{\rm SN}$ is degenerate to β and $R_{\rm SN}^0$, shown in Fig. 8.1. The assumed lower limit of $E_{\rm tot}^0 = 30$ is shown, which corresponds to a low neutron star binding energy. The other extreme, $E_{\rm tot}^{\rm SN} = 100$ describes a large neutron star binding energy and is more in accord with SN 1987As preferred value of $E_{\rm tot}^{\rm SN} \sim 80$. If we have no additional information on β and $R_{\rm SN}^0$, the DSNB will still place a constraint of 10×10^{51} erg $\lesssim E_{\rm tot}^{\rm SN} \lesssim 700 \times 10^{51}$ erg, which is not significant compared to our knowledge from neutron star observations, SN 1987A and SN simulations. If we know β to $\sim 20\%$ from SFR observations and $R_{\rm SN}^0$ to $\sim 25\%$ as well from SN surveys, we can constrain $E_{\rm tot}^{\rm SN}$ to 30×10^{51} erg $\lesssim E_{\rm tot}^{\rm SN} \lesssim 90 \times 10^{51}$ erg, which is already a confirmation of previous observations and SN simulations. More accurate knowledge of the supernova rate will yield better constraints on $E_{\rm tot}^{\rm SN}$. However, due to dust-extinction uncertainties it does not seem likely that uncertainties get better than about 15%, which would not yield strong constraints on $E_{\rm tot}^{\rm SN}$. The luckier case will be a galactic supernova and the indirect inference of $R_{\rm SN}^0$ and β from this event and the DSNB combined.

8.2.2 Mean Energy

The mean energy of the SN neutrinos $\overline{E}_{\rm SN}$ leaves a very strong imprint on the mean energy of the DSNB $\overline{E}$, as can be seen from Fig. 8.3. One extreme case is represented by the SN 1987A implication $\overline{E}_{\rm SN} = 9$ MeV, the other limiting scenario corresponds to the findings of some simulations, $\overline{E}_{\rm SN} = 22$ MeV. The dependence is linear as discussed in chapter 5, displayed in Fig. 5.3. Only the recent star-formation history β has a comparable impact on $\overline{E}$, but by a factor of ~ 2 lower, being only slightly degenerate. Assuming $1 < \beta < 4$, and $\overline{E}_{\rm SN} = 17$ MeV, a statistically significant DSNB detection will determine $\overline{E}_{\rm SN}$ to 14 MeV $\lesssim \overline{E}_{\rm SN} \lesssim 20$ MeV, which would already exclude some extreme simulations and also the SN 1987A preferred value of 9 MeV. If SFR observations constrain $\beta \approx 2-3$, then the constraint on $\overline{E}_{\rm SN}$

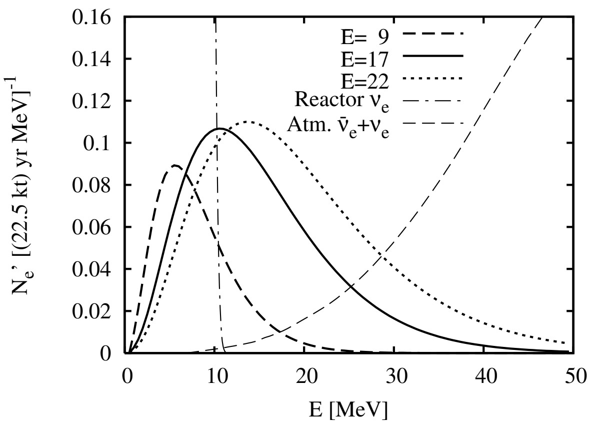

Figure 8.3: Event rates of the DSNB at SK for different values of $\overline{E}_{\rm SN}$.

would be tightened to 15 MeV $\lesssim \overline{E}_{\rm SN} \lesssim$ 19 MeV. Thus, the mean energy of SN neutrino spectra can be determined to a fairly good accuracy by the DSNB. Such a determination will be extremely useful if no galactic SN occurs in the near future and the knowledge of $\overline{E}_{\rm SN}$ might provide hints about the SN explosion mechanism, or at least present a probe for SN simulations. We conclude that in the absence of a future galactic SN, $\overline{E}_{\rm SN}$ will thus be the parameter that will be easiest to extract from the DSNB and also the parameter that we can put the most significant constraints on.

8.2.3 Spectral Pinching

The spectral pinching $a_{\rm SN}$ affects the DSNB little, as displayed in Fig. 8.4. A limiting case of no pinching would be a Maxwell-Boltzmann distribution with $a_{\rm SN} \approx 2$, more specifically, we chose $a_{\rm SN} = 1.9$. Pronounced pinching is displayed in the case $a_{\rm SN} = 4.3$ as is typically found for the $\bar{\nu}_e$-spectra in the Garching simulations [15]. The spectral pinching of the individual SN spectrum affects only the outcoming pinching of the DSNB a. As its influence on the DSNB pinching a is almost degenerate to the influence of the early star-formation history α, we would need to know α to a good accuracy in order to infer $a_{\rm SN}$ from the DSNB. Unfortunately determining the pinching a from the DSNB requires very high statistics, probably more than ten years of observation with a Gd megaton detector. Moreover, α is not very likely to be determined very accurately from future star formation rate observations, due to the problem of dust extinction. Thus we conclude that the determination of the individual SN pinching $a_{\rm SN}$ from the DSNB seems very unlikely, if at all possible.

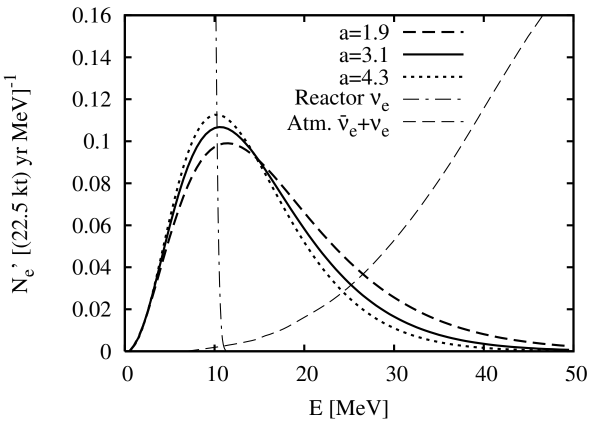

Figure 8.4: Event rates of the DSNB at SK for different choices of a.

8.3 Constraining the Neutrino Magnetic Dipole Moment

If neutrinos are Dirac-particles and there exist interactions which turn left-handed (l.h.) neutrinos into right-handed ones, then these right-handed (r.h.) neutrinos do not interact by the standard weak interactions and would hence not be trapped inside the core of an SN. We will only discuss right-handed neutrinos, but the same arguments also apply to left-handed antineutrinos, of course.

Notably spin-flip scattering of neutrinos with a magnetic dipole moment μ_ν will alter the detectable DSNB signal (Ref. [34], chapter 13). If μ_ν is large enough, the l.h. states that are produced will be scattered to r.h. states by spin-flip scattering, mostly on protons. These can escape freely and can rotate back into l.h. states by spin precession in the strong magnetic fields around the SN and in the galaxy. As they are more energetic than those from the neutrino sphere, one would expect high-energy events at detection.

If we assume the extreme case that all ν_L will be converted to ν_R inside the SN and half of them will rotate back outside the SN, then the mean energy of these neutrinos would be $3T$ for a Maxwell-Boltzman distribution which corresponds to 90 MeV for typical temperatures of 30 MeV in the inner core. To maximize the effect, let us further assume the largest flux that is compatible with the SK result, which would correspond to parameters of, say, $R^0_{\rm SN} = 1.5 \times 10^{-4}$ Mpc^{-3} yr^{-1}, $\beta = 4.0$, $\alpha = 1$, $E^{\rm SN}_{\rm tot} = 70 \times 10^{51}$ erg, where we have not taken into account oscillations. These would not change our consideration, since the difference between the flavors only arises due to different transport mechanisms, which do not apply here. Figure 8.5 shows how the event rate at SK would be distorted by the effect. We show the scenario for parameters according to our baseline case and for the discussed case of very large parameters. One can see from this simple approximation that a large magnetic moment can currently not be excluded by the SK results, because the corresponding effect cannot be distinguished from the backgrounds. However, gadolinium detection might reduce the backgrounds from Michel electrons by a factor of 5, then we would be able to detect possible high-energy DSNB events. Thus from a future non-observation of the DSNB in the high-energy range, one could put a constraint on μ_ν of the order $\sim 10^{-12}\mu_{\rm B}$ (Ref. [34], chapter 13). Additionally, the constraint would be dependent on parameter choices and only apply for large enough DSNB-parameters.

However, observations of the SN 1987A neutrino burst have already implied limits for several assumptions. The limits range from $\mu_\nu \lesssim 10^{-12}\mu_{\rm B}$ to $10^{-13}\mu_{\rm B}$ [158, 159, 160, 161]. By the time we obtain high statistics in the DSNB using megaton-detectors and Gadolinium Trichloride detection technique (~ 100 events/yr), we will be able to distinguish if there is an un-

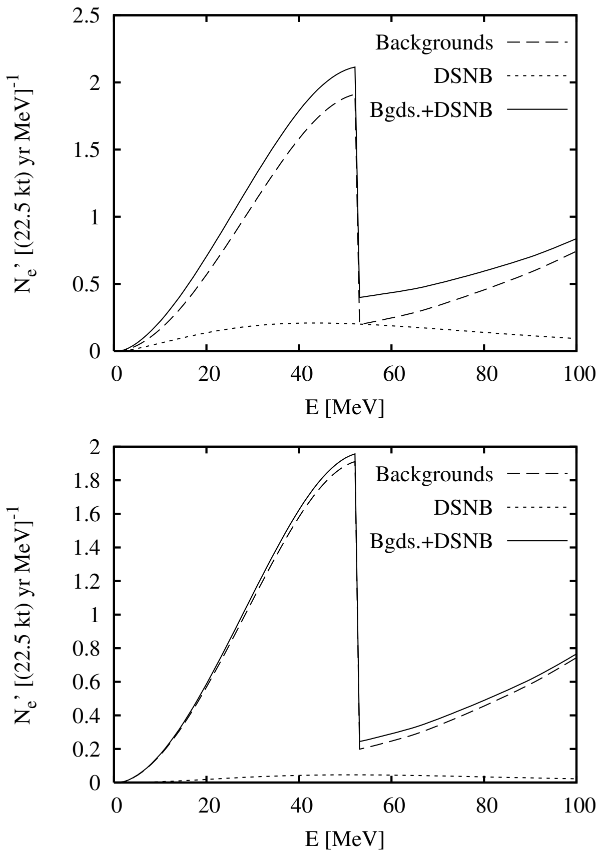

Figure 8.5: Distortion of the event rate of the DSNB at SK by a large μ_ν. The dashed line is the sum of the backgrounds from invisible muons and atmospheric ν_e and $\bar{\nu}_e$. The dotted line displays the distorted DSNB, the solid line the sum of the backgrounds and the distorted DSNB. The situation for an upper limit of the DSNB is shown in the upper panel, in the lower panel we display our baseline estimate.

expected high energy part of the neutrino spectrum. We might thus be able to independently confirm the limit that has been set by SN 1987A. Of course, these conclusions can be turned around in the sense that the SN 1987A limits on μ_ν imply that such high-energy events will not occur for the DSNB and that a possible magnetic moment will therefore not be an important effect in the interpretation of future DSNB measurements.

Chapter 9

Summary and Outlook

We have studied the properties and detectability of the DSNB. We have applied a novel strategy for our analysis of the DSNB. Whereas previous works adopted one or several fixed reference models for their SN rate and neutrino spectra, we chose to parameterize these inputs by essentially seven parameters. The SN history was parametrized by the local SN rate $R^0_{\rm SN}$, the recent SN history β, the early SN history α and the onset of stellar collapse $z_{\rm max}$. The effective $\bar{\nu}_e$ SN spectrum was parametrized by the total energy $E^{\rm SN}_{\rm tot}$ emitted in $\bar{\nu}_e$, the mean energy $\overline{E}_{\rm SN}$ and the pinching parameter $a_{\rm SN}$. This strategy seems to be appropriate to the problem, since the uncertainties in both the SN history as well as the SN neutrino spectra are large. In our analysis, we adopted rather broad ranges of these parameters in order to specify which bounds could actually be set on these by the detection of the DSNB. For our discussion of these parameters, we use a baseline case for each parameter.

We base our discussion of neutrino spectra on some recent works which have reported a change in the view of flavor-dependent neutrino spectra, notably through a more accurate treatment of ν_x transport inside the SN core. Whereas the former literature on SN simulations and likewise on the DSNB has assumed a strong flavor-dependent hierarchy of mean energies and an equipartition of luminosities, these works find a shallow hierarchy between $\bar{\nu}_e$ and ν_x, but possibly large differences in luminosities. This also changes the perception of the DSNB such that flavor oscillations and the type of neutrino mass hierarchy do not play a crucial role for the detectable neutrino signal and can be summarized in an effective parameterization of the $\bar{\nu}_e$-flux received at the detector. We also find that previous works on the DSNB do not allow for uncertainties in the neutrino spectra, except for one [7]. We find the uncertainties to be rather large, possibly allowing for the detectable DSNB to vary by at least one order of magnitude, depending on parameter choices. For the first time, we also included the implications of SN 1987A for a relatively low $\bar{\nu}_e$ mean energy of (~ 9 MeV).

Our analysis of the SN history takes into account observations both of the SN rate and of the closely related SFR. We include high-redshift SN observations, even though these currently suffer from low statistics. We explore a broad parameter range of the (β, α)-parameterization that is accessible by observation, only excluding some obvious outliers. We find that the conversion factor from the SFR to the SN rate implies more uncertainties than usually assumed in the literature on the DSNB and that it seems more appropriate to rely on direct SN observations for the determination of the local SN rate, rather than on indirect tracers of the SFR which has to be converted by a conversion factor with uncertainties as high as 50%.

We characterize the flux in the energy window 10–30 MeV by an a-fit and find that in this energy range, the fit works sufficiently well (less than 10% deviation from the event rate). Based on these fits, which are essentially a convolution of a 7-parameter space onto 3 parameters, we formulate an analytic description of the spectral dependence on the parameters. Our baseline case of the DSNB agrees well with previous works, but predicts a rather low flux. This is mainly due to the relatively low local SN rate that we have taken from Cappellaro et al. [83]. In particular, it predicts a total flux of $6.8\ \bar{\nu}_e\ \mathrm{cm}^{-2}\ \mathrm{s}^{-1}$. However, if we choose the important parameters to be large, notably R^0_{SN}, we get fluxes of $\sim 20\ \bar{\nu}_e\ \mathrm{cm}^{-2}\ \mathrm{s}^{-1}$. Perhaps our most interesting result is that we can reduce the discussion of the DSNB to essentially three parameters. One of them is obviously the global factor $R^0_{\mathrm{SN}} \times E^{\mathrm{SN}}_{\mathrm{tot}}$, the other two are β and $\overline{E}_{\mathrm{SN}}$. These parameters on their own account for most of the uncertainties connected to the DSNB. Contrarily, α and a_{SN} have little to no influence and will only play a role in far-future high-statistics observations.

We find that water Cherenkov detectors are the only means to obtain sufficient statistics of the DSNB. Scintillation detectors like KamLAND will not be able to see the DSNB at all. However, liquid argon detectors like ICARUS or its future enlarged successors might well be able to detect the ν_e part of the spectrum which will contribute an important complementary information to the $\bar{\nu}_e$-detection at water Cherenkov experiments. If the newly proposed Gadolinium Trichloride detection technique passes the research and development tests, then it will be an extremely promising tool for the DSNB detection, since now there is no detection window for the DSNB and SK is not able to probe the low-energy part of the flux within the foreseeable future. The $GdCl_3$ technique would enable us to reduce backgrounds drastically, allowing a statistically significant detection. Next-generation megaton water Cherenkov detectors, such as Hyper-Kamiokande, UNO and others, have the potential to enhance the statistics of the DSNB detection considerably, if used in combination with $GdCl_3$.

Analyzing backgrounds, we find that reactor $\bar{\nu}_e$ will be extremely important to understand if detection with Gadolinium is feasible and successful in reducing muon-induced spallation down to about 10 MeV, which has been claimed [13]. We present a detailed analysis of the spectral shape of this background [151] and find that the analytic expressions found in literature overestimate the reactor-$\bar{\nu}_e$ flux at low energies, so that according to our analysis, the DSNB and the reactor backgrounds at SK become comparable at energies of about 10 MeV, which is lower than other works imply [133]. We estimate that the background from reactor $\bar{\nu}_e$ could be further reduced up to a factor of ~ 20, if the proposed UNO detector is built far away from reactors, as some candidate sites imply.

We observe that a variation in the mean energy leaves a strong imprint on the mean energy of the event rate and conclude that this parameter will be the easiest to extract from an observation of the DSNB. In particular, the best-fit value of SN 1987A (9 MeV) can be tested. Concerning the SN history, we find that naturally, the local SN rate and the total neutrino luminosity have a completely degenerate impact on the event rate, altering only its normalization. The recent SN history has a similar effect, while also influencing the detectable mean energy and can be grouped together with the two parameters mentioned above. Thus we have essentially three degenerate parameters and the detection of the DSNB will give a surface in the three-parameter space. However, it is to be expected that observations in other fields, such as SFR observations, which already lean toward placing tighter constraints on β, or SN surveys, will contribute to pinning down one or two of these parameters, which would enable us to determine the remaining one or two. Contrary to what other works have stated, we find that the high redshift star formation affects the detectable DSNB only little. The same applies to the pinching parameter. However, they affect the pinching of the resulting event rate to some extent and with high statistics and sufficient constraints on the other parameters, we might be able to put some constraints on these two as well. We assume that nevertheless other observations, such as the SFR, or a galactic SN are more promising in constraining these.

We conclude that the detection of the DSNB will indeed be an important contribution to different fields of astroparticle physics. It will be especially important if no galactic SN occurs in the close future. The estimates on the SN rate of our galaxy and the Magellanic Clouds range from one to several per century, but even with a high assumed rate, we might have to wait a long time for the next galactic SN. The DSNB might be the only possibility to observe SN neutrinos in the foreseeable future, and we might be able to probe the spectral characteristics of these neutrinos, and even get information about the currently unknown details of the SN explosion mechanism.

However, even with the occurrence of a galactic SN, there are parameters that can only be probed by the observation of the DSNB. Neutrino decays can be constrained as has been pointed out by Fogli et al. [9], enabling the tightest constraint on neutrino lifetimes so far. Moreover, the DSNB is an ideal tool to probe the star formation history directly, since the usual problems with dust extinction in observing the SFR do not apply to neutrinos. Additionally, with sufficient knowledge of SN neutrino spectra, the DSNB probes the SN rate directly, while SFR observations have to use indirect observables. Thus, with the occurrence of a galactic SN or progress in SN simulations we will be able to constrain the local SN rate and the recent star-formation history and the additional knowledge of one of the two from other observations (e.g. R^0_{SN} from SN surveys) will determine the remaining one.

Whether or not we will be so lucky as to witness a galactic SN explosion in our lifetime, the DSNB will remain an attractive tool for both astrophysics and particle physics.

Bibliography

[1] M. Maltoni, T. Schwetz, M. A. Tortola, and J. W. F. Valle, "Status of global fits to neutrino oscillations", *New J. Phys.*, 6:122, 2004, hep-ph/0405172.

[2] R. M. Bionta et al., "Observation of a neutrino burst in coincidence with supernova SN1987A", *Phys. Rev. Lett.*, 58:1494, 1987.

[3] K. Hirata et al., "Observation of a neutrino burst from the supernova SN1987A", *Phys. Rev. Lett.*, 58:1490, 1987.

[4] L. M. Krauss, S. L. Glashow, and D. N. Schramm, "Antineutrino astronomy and geophysics", *Nature*, 310:191, 1984.

[5] G. S. Bisnovatyi-Kogan and Z. F. Seidov, "Supernovae, neutrino rest mass, and the middle-energy neutrino background in the universe", *Annals N. Y. Acad. Sci.*, 422:319, 1984.

[6] L. E. Strigari, M. Kaplinghat, G. Steigman, and T. P. Walker, "The supernova relic neutrino backgrounds at KamLAND and Super-Kamiokande", *JCAP*, 3:7, 2004.

[7] S. Ando and K. Sato, "Relic neutrino background from cosmological supernovae", *New J. Phys.*, 6:170, 2004.

[8] P. Madau, H. C. Ferguson, M. E. Dickinson, M. Giavalisco, C. C. Steidel, and A. Fruchter, "High-redshift galaxies in the Hubble Deep Field: colour selection and star formation history to z$\sim$4", *Mon. Not. Roy. Astron. Soc.*, 283:1388, 1996.

[9] G. L. Fogli, E. Lisi, A. Mirizzi, and D. Montanino, "Three-generation flavor transitions and decays of supernova relic neutrinos", *Phys. Rev.*, 70:013001, 2004.

[10] A. Dar, "Has a cosmological neutrino background from gravitational stellar collapse been detected?", *Phys. Rev. Lett.*, 55:1422, 1985.

[11] W. Zhang, E. W. Beier, L. Feldscher, E. D. Frank, and W. Frati, “Experimental limit on the flux of relic antineutrinos from past supernovae”, *Phys. Rev. Lett.*, 61:385, 1988.

[12] M. Malek et al., “Search for supernova relic neutrinos at Super-Kamiokande”, *Phys. Rev. Lett.*, 90:061101, 2003.

[13] J. F. Beacom and M. R. Vagins, “Antineutrino spectroscopy with large water Cherenkov detectors”, *Phys. Rev. Lett.*, 93:171101, 2004, hep-ph/0309300.

[14] M. Th. Keil. *Supernova Neutrino Spectra and Applications to Flavor Oscillations*. PhD thesis, Technische Universität München, 2003.

[15] M. T. Keil, G. G. Raffelt, and H. Janka, “Monte Carlo study of supernova neutrino spectra formation”, *Astrophys. J.*, 590:971, 2003.

[16] T. Dahlen et al., “High-redshift supernova rates”, *Astron. J.*, 613:189, 2004.

[17] E. W. Kolb and M. S. Turner. *The Early Universe*. Addison-Wesley, New York, 1990.

[18] R. M. Wald. *General Relativity*. Univ. Chicago Press, Chicago, 1984.

[19] D. N. Spergel et al., “First year Wilkinson Microwave Anisotropy Probe (WMAP) observations: Determination of cosmological parameters”, *Astrophys. J. Suppl. Ser.*, 148:175, 2003, astro-ph/0302209.

[20] C. L. Kuo et al., “High resolution observations of the CMB power spectrum with ACBAR”, *Astron. J.*, 600:32, 2002, astro-ph/0212289.

[21] T. J. Pearson et al., “The anisotropy of the microwave background to l = 3500: Mosaic observations with the Cosmic Background Imager”, *Astrophys. J.*, 556:591, 2003, astro-ph/0205388.

[22] W. J. Percival et al., “The 2dF Galaxy Redshift Survey: The power spectrum and the matter content of the universe”, *Mon. Not. Roy. Astron. Soc.*, 327:1297, 2001.

[23] L. Verde et al., “The 2dF Galaxy Redshift Survey: The bias of galaxies and the density of the Universe”, *Mon. Not. Roy. Astron. Soc.*, 432:335, 2002, astro-ph 0112161.

[24] R. A. C. Croft et al., “Towards a precise measurement of matter clustering: Lyman-alpha forest data at redshifts 2–4”, *Astron. J.*, 20:581, 2002, astro-ph/001232.

[25] N. Y. Gnedin and A. J. S. Hamilton, "Matter power spectrum from the Lyman-alpha forest: Myth or reality?", *Mon. Not. Roy. Astron. Soc.*, 334:107, 2002.

[26] P. M. Garnavich et al., "Supernova limits on the cosmic equation of state", *Astron. J.*, 74:509, 1998, astro-ph/9806396.

[27] A. G. Riess et al., "The farthest known supernova: Support for an accelerating universe and a glimpse of the epoch of deceleration", *Astrophys. J.*, 49:560, 2001, astro-ph/0104455.

[28] W. L. Freedman et al., "Final results from the Hubble Space Telescope Key Project to measure the Hubble constant", *Astrophys. J.*, 553:47, 2001.

[29] E. Cappellaro and M. Turatto. "Supernova types and rates". In *Proceedings of the Meeting "The Influence of Binaries on Stellar Population Studies", Brussels, Belgium, 21–25 August 2000*, volume 264 of *Astrophysics and Space Science Library*, page 199, 2001.

[30] A. Kim, A. Goobar, and S. Perlmutter, "A generalized K correction for type Ia supernovae: comparing R-band photometry beyond $z = 0.2$ with B, V, and R-band nearby photometry", *Publications of the Astronomical Society of the Pacific*, 108:190, 1996, astro-ph/9505024.

[31] John L. Tonry et al., "Cosmological results from high-z supernovae", *Astron. J.*, 594:1, 2003, astro-ph/0305008.

[32] Robert A. Knop et al., "New constraints on Ω_m, Ω_Λ, and w from an independent set of eleven high-redshift supernovae observed with HST", *Astron. J.*, 598:102, 2003, astro-ph/0309368.

[33] W. Hillebrandt, J. C. Niemeyer, M. Reinecke, and C. Travaglio, "The physics and astrophysics of type Ia supernova explosions", *Memorie della Societa Astronomica Italiana*, 74:942, 2003.

[34] Georg G. Raffelt. *Stars as Laboratories for Fundamental Physics.* Univ. of Chicago Press, Chicago, 1996.

[35] H. A. Bethe and J. R. Wilson, "Revival of a stalled supernova shock by neutrino heating", *Astrophys. J.*, 295:14, 1985.

[36] R. Buras, H. Janka, M. T. Keil, G. G. Raffelt, and M. Rampp, "Electron neutrino pair annihilation: A new source for muon and tau neutrinos in supernovae", *Astrophys. J.*, 587:320, 2003.

[37] M. Liebendörfer, A. Mezzacappa, F. Thielemann, O. E. Messer, W. R. Hix, and S. W. Bruenn, "Probing the gravitational well: No supernova explosion in spherical symmetry with general relativistic Boltzmann neutrino transport", *Phys. Rev.*, D 63:103004, 2001.

[38] A. Mezzacappa, M. Liebendörfer, O. E. Messer, W. R. Hix, F. Thielemann, and S. W. Bruenn, "Simulation of the spherically symmetric stellar core collapse, bounce, and postbounce evolution of a star of 13 solar masses with Boltzmann neutrino transport, and its implications for the supernova mechanism", *Phys. Rev. Lett.*, 86:1935, 2001.

[39] M. Rampp and H.-T. Janka, "Spherically symmetric simulation with Boltzmann neutrino transport of core collapse and postbounce evolution of a 15 M_{solar} star", *Astrophys. J.*, 539:L33, 2000.

[40] Todd A. Thompson, Adam Burrows, and Philip A. Pinto, "Shock breakout in core-collapse supernovae and its neutrino signature", *Astron. J.*, 592:434, 2003, astro-ph/0211194.

[41] J. F. Beacom, R. N. Boyd, and A. Mezzacappa, "Black hole formation in core-collapse supernovae and time-of-flight measurements of the neutrino masses", *Phys. Rev.*, D 63:073011, 2001.

[42] T. Totani, K. Sato, H. E. Dalhed, and J. R. Wilson, "Future detection of supernova neutrino burst and explosion mechanism", *Astrophys. J.*, 496:216, 1998.

[43] A. Burrows, "Convection and the mechanism of type II supernovae", *Astrophys. J.*, 318:L57, 1987.

[44] S. W. Bruenn, A. Mezzacappa, and T. Dineva, "Dynamic and diffusive instabilities in core collapse supernovae", *Phys. Rep.*, 256:69, 1995.

[45] W. Keil, H.-T. Janka, and E. Mueller, "Ledoux convection in protoneutron stars—a clue to supernova nucleosynthesis?", *Astrophys. J.*, 473:L111, 1996.

[46] A. Mezzacappa, A. C. Calder, S. W. Bruenn, J. M. Blondin, M. W. Guidry, M. R. Strayer, and A. S. Umar, "The interplay between protoneutron star convection and neutrino Transport in core-collapse supernovae", *Astrophys. J.*, 493:848, 1998.

[47] J. A. Pons, S. Reddy, M. Prakash, J. M. Lattimer, and J. A. Miralles, "Evolution of protoneutron stars", *Astrophys. J.*, 513:780, 1999, astro-ph/9807040.

[48] R. Buras, M. Rampp, H.-T. Janka, and K. Kifonidis, “Improved models of stellar core collapse and still no explosions: What is missing?”, *Phys. Rev. Lett.*, 90:241101, 2003.

[49] H.-T. Janka. “Neutrinos from type-II supernovae and the neutrino-driven supernova mechanism”. In *Frontier Objects in Astrophysics and Particle Physics. Proceedings of the Vulcano Workshop 1992, Italy, 18–23 May*, page 345, 1993.

[50] H.-T. Janka, R. Buras, K. Kifonidis, T. Plewa, and M. Rampp. “Core collapse and then? The route to massive star explosions”. In *From Twilight to Highlight: The Physics of Supernovae. Proceedings of the ESO/MPA/MPE Workshop, Garching, Germany, 29-31 July*, page 39, 2003.

[51] A. Burrows, T. Young, P. Pinto, R. Eastman, and T. A. Thompson, “A new algorithm for supernova neutrino transport and some applications”, *Astrophys. J.*, 539:865, 2000.

[52] S. W. Bruenn, K. R. De Nisco, and A. Mezzacappa, “General relativistic effects in the core collapse supernova mechanism”, *Astrophys. J.*, 560:326, 2001.

[53] S. Yamada, H. Janka, and H. Suzuki, “Neutrino transport in type II supernovae: Boltzmann solver vs. Monte Carlo method”, *Astron. Astrophys.*, 344:533, 1999.

[54] Georg G. Raffelt, Mathias Th. Keil, Robert Buras, Hans-Thomas Janka, and Markus Rampp. “Supernova neutrinos: Flavor-dependent fluxes and spectra”. In *Proceedings of NOON 03, Kanazawa, Japan, 10–14 Feb*, 2003.

[55] H.-T. Janka and W. Hillebrandt, “Neutrino emission from type II supernova—an analysis of the spectra”, *Astron. Astrophys.*, 224:49, 1989.

[56] R. Mayle, J. R. Wilson, and D. N. Schramm, “Neutrinos from gravitational collapse”, *Astrophys. J.*, 318:288, 1987.

[57] S. W. Bruenn, “Neutrinos from SN1987A and current models of stellar-core collapse”, *Phys. Rev. Lett.*, 59:938, 1987.

[58] E. S. Myra and A. Burrows, “Neutrinos from type II supernovae—The first 100 milliseconds”, *Astrophys. J.*, 364:222, 1990.

[59] H.-T. Janka and W. Hillebrandt, "Monte Carlo simulations of neutrino transport in type II supernovae", *Astron. Astrophys. Suppl. Ser.*, 78:375, 1989.

[60] H. Suzuki, "Neutrino emission from protoneutron star with modified URCA and nucleon bremsstrahlung processes", *Num. Astrophys. Japan*, 2:267, 1991.

[61] H. Suzuki, "Supernova neutrinos: Multigroup simulations of neutrinos from protoneutron star", 1993, Prepared for International Symposium on Neutrino Astrophysics, Takayama / Kamioka, Japan, 19-22 Oct 1992.

[62] H. Suzuki. *Neutrino Burst from Supernova Explosion and Proto Neutron Star Cooling.* PhD thesis, University of Tokyo, 1989.

[63] J. R. Wilson and R. W. Mayle, "Convection in core collapse supernovae", *Phys. Rep.*, 163:63, 1988.

[64] J. R. Wilson and R. W. Mayle, "Report on the progress of supernova research by the Livermore group", *Phys. Rep.*, 227:97, 1993.

[65] R. W. Mayle. *Physical Processes in Collapse Driven Supernova.* PhD thesis, University of Michigan, 1985.

[66] J. R. Wilson, R. Mayle, S. E. Woosley, and T. Weaver, "Stellar core collapse and supernova", *Annals N. Y. Acad. Sci.*, 470:267, 1986.

[67] S. E. Woosley, A. Heger, and T. A. Weaver, "The evolution and explosion of massive stars", *Rev. Mod. Phys.*, 74:1015, 2002.

[68] S. Fukuda et al., "Determination of solar neutrino oscillation parameters using 1496 days of Super-Kamiokande-I data", *Phys. Lett. B*, 539:179, 2002, hep-ex/0205075.

[69] S. N. Ahmed et al., "Measurement of the total active ^{8}B solar neutrino flux at the Sudbury Neutrino Observatory with enhanced neutral current sensitivity", *Phys. Rev. Lett.*, 92:181301, 2004.

[70] Y. Fukuda et al., "Measurement of the flux and zenith-angle distribution of upward throughgoing muons by Super-Kamiokande", *Phys. Rev. Lett.*, 82:2644, 1999.

[71] K. Eguchi et al., "First results from KamLAND: Evidence for reactor antineutrino disappearance", *Phys. Rev. Lett.*, 90:021802, 2003.

[72] M. Apollonio and A. Baldini, "Limits on neutrino oscillations from the CHOOZ experiment", *Phys. Lett. B*, 466:415, 1999.

[73] Amol S. Dighe and Alexei Yu. Smirnov, "Identifying the neutrino mass spectrum from the neutrino burst from a supernova", *Phys. Rev.*, D62:033007, 2000, hep-ph/9907423.

[74] E. N. Alekseev, L. N. Alekseeva, V. I. Volchenko, and I. V. Krivosheina, "Possible detection of a neutrino signal on February 23, 1987 with the Baksan underground scintillation telescope of the Nuclear Research Institute of the Soviet Academy of Sciences", *Pis'ma Zh. Eksp. Teor. Fiz.* , 45:461, 1987.

[75] T. J. Loredo and D. Q. Lamb, "Neutrinos from SN 1987A - Implications for cooling of the nascent neutron star and the mass of the electron antineutrino", *Annals N. Y. Acad. Sci.*, 571:601, 1989.

[76] Th. J. Loredo and D. Q. Lamb, "Bayesian analysis of neutrinos observed from supernova SN 1987A", *Phys. Rev.*, D65:063002, 2002, astro-ph/0107260.

[77] E. Cappellaro, R. Barbon, and M. Turatto. "Supernova statistics". In *Supernovae: 10 Years of 1993J. Proceedings of the IAU Colloquium 192, Valencia, Spain, 22–26 April 2003*, 2003.

[78] R. Barbon, V. Buondí, E. Cappellaro, and M. Turatto, "The Asiago Supernova Catalogue - 10 years after", *Astron. Astrophys. Suppl. Ser.*, 139:531, 1999.

[79] E. Cappellaro, M. Turatto, D. Y. Tsvetkov, O. S. Bartunov, C. Pollas, R. Evans, and M. Hamuy, "The rate of supernovae from the combined sample of five searches.", *Astron. Astrophys.*, 322:431, 1997, astro-ph/9611191.

[80] J. Leaman, W. Li, and A. Filippenko, "The Supernova Rate in nearby galaxies determined from the Lick Observatory Supernova Search", *American Astronomical Society Meeting Abstracts*, 205:7102, 2004.

[81] W. M. Wood-Vasey and SNfactory, "Supernova rates from the Nearby Supernova Factory Prototype Search", *American Astronomical Society Meeting Abstracts*, 205:4003, 2004.

[82] L. Strolger. *The Nearby Galaxies Supernova Search project: The Rate of Supernovae in the Local Universe.* PhD thesis, University of Michigan, 2003.

[83] E. Cappellaro, R. Evans, and M. Turatto, "A new determination of supernova rates and a comparison with indicators for galactic star formation", *Astron. Astrophys.*, 351:459, 1999.

[84] G. A. Tammann, "On the frequency of supernovae as a function of the integral properties of inter mediate and late type spiral galaxies", *Astron. Astrophys.*, 8:458, 1970.

[85] A.-L. Melchior, F. Combes, and C. Pennypacker, "Supernova rates and host galaxies properties in the local universe", *New Astronomy Review*, 48:591, 2004.

[86] S. van den Bergh and G. A. Tammann, "Galactic and extragalactic supernova rates", *Annu. Rev. Astron. Astrophys.*, 29:363, 1991.

[87] E. Cappellaro et al., "Death rate of massive stars at redshift $\sim$0.3", *Astron. Astrophys.*, 430:833, 2005.

[88] S. L. Shapiro and S. S. Teukolsky. *Black Holes, White Dwarfs, and Neutron Stars: The Physics of Compact Objects*. John Wiley and Sons, New York, 1986.

[89] J. Scalo. "The IMF revisited: A case for variations". In *The Stellar Initial Mass Function. Proceedings of the 38th Herstmonceux Conference*, volume 142 of *Astronomical Society of the Pacific Conference Series*, page 201, 1998.

[90] R. C. Kennicutt, "Star formation in galaxies along the Hubble sequence", *Annu. Rev. Astron. Astrophys.*, 36:189, 1998.

[91] C. C. Steidel, K. L. Adelberger, M. Giavalisco, M. Dickinson, and M. Pettini, "Lyman-break galaxies at $z \gtrsim 4$ and the evolution of the ultraviolet luminosity density at high redshift", *Astrophys. J.*, 519:1, 1999.

[92] A. J. Bunker, E. R. Stanway, R. S. Ellis, and R. G. McMahon, "The star formation rate of the universe at z$\sim$6 from the Hubble Ultra-Deep Field", *Mon. Not. Roy. Astron. Soc.*, 355:374, 2004.

[93] R. J. Bouwens et al., "Star formation at $z \sim$6: The Hubble ultra deep parallel fields", *Astrophys. J.*, 606:L25, 2004.

[94] S. Charlot et al., "Star formation, metallicity and dust properties derived from the Stromlo-APM galaxy survey spectra", *Mon. Not. Roy. Astron. Soc.*, 330:876, 2002, astro-ph/0111289.

[95] M. Sullivan, B. Mobasher, B. Chan, L. Cram, R. Ellis, M. Treyer, and A. Hopkins, "A comparison of independent star formation diagnostics for an Ultraviolet-selected sample of nearby galaxies", *Astrophys. J.*, 558:72–80, 2001, astro-ph/0104425.

[96] A. M. Hopkins, A. J. Connolly, D. B. Haarsma, and L. E. Cram, "Towards a resolution of the discrepancy between different estimators of star formation rate", *Astron. J.*, 122:288, 2001, astro-ph/0103253.

[97] J. J. Condon, "Radio emission from normal galaxies", *Annu. Rev. Astron. Astrophys.*, 30:575, 1992.

[98] R. B. Larson and B. M. Tinsley, "Star formation rates in normal and peculiar galaxies", *Astrophys. J.*, 219:46, 1978.

[99] G. D. Coleman, C.-C. Wu, and D. W. Weedman, "Colors and magnitudes predicted for high redshift galaxies", *Astrophys. J. Suppl. Ser.*, 43:393, 1980.

[100] M. Rowan-Robinson et al., "Observations of the Hubble Deep Field with the Infrared Space Observatory—V. Spectral energy distributions, starburst models and star formation history", *Mon. Not. Roy. Astron. Soc.*, 289:490, 1997.

[101] R. C. Kennicutt, "A spectrophotometric atlas of galaxies", *Astrophys. J. Suppl. Ser.*, 79:255, 1992.

[102] P. Madau, L. Pozzetti, and M. Dickinson, "The star formation history of field galaxies", *Astrophys. J.*, 498:106, 1998.

[103] D. Calzetti, A. L. Kinney, and T. Storchi-Bergmann, "Dust extinction of the stellar continua in starburst galaxies: The ultraviolet and optical extinction law", *Astrophys. J.*, 429:582, 1994.

[104] P. Ghosh and N. E. White, "X-Ray probes of cosmic star formation history", *Astrophys. J.*, 559:L97, 2001.

[105] W. N. Brandt et al., "The Chandra Deep Field North survey. V. 1 Ms source catalogs", *Astron. J.*, 122:2810, 2001.

[106] K. Nandra et al., "X-ray properties of lyman break galaxies in the Hubble Deep Field-North Region", *Astrophys. J.*, 576:625, 2002.

[107] K. M. Lanzetta, A. M. Wolfe, and D. A. Turnshek, "The IUE Survey for damped Lyman-alpha and Lyman-limit absorption systems: Evolution of the gaseous content of the universe", *Astrophys. J.*, 440:435, 1995.

[108] S. J. Lilly, O. Le Fevre, F. Hammer, and D. Crampton, "The Canada-France Redshift Survey: The luminosity density and star formation history of the universe to z approximately 1", *Astrophys. J.*, 460:L1, 1996.

[109] L. L. Cowie, A. Songaila, E. M. Hu, and J. G. Cohen, "New insight on galaxy formation and evolution from Keck spectroscopy of the Hawaii deep fields", *Astron. J.*, 112:839, 1996.

[110] A. J. Connolly, A. S. Szalay, M. Dickinson, M. U. Subbarao, and R. J. Brunner, "The evolution of the global star formation history as measured from the Hubble Deep Field", *Astrophys. J.*, 486:L11, 1997.

[111] M. J. Sawicki, H. Lin, and H. K. C. Yee, "Evolution of the galaxy population based on photometric redshifts in the Hubble Deep Field", *Astron. J.*, 113:1, 1997.

[112] M. A. Treyer, R. S. Ellis, B. Milliard, J. Donas, and T. J. Bridges, "An ultraviolet-selected galaxy redshift survey: New estimates of the local star formation rate", *Mon. Not. Roy. Astron. Soc.*, 300:303, 1998.

[113] S. M. Pascarelle, K. M. Lanzetta, and A. Fernández-Soto, "The ultraviolet luminosity density of the universe from photometric redshifts of galaxies in the Hubble Deep Field", *Astrophys. J.*, 508:L1, 1998.

[114] D. H. Hughes et al., "High-redshift star formation in the Hubble Deep Field revealed by a submillimetre-wavelength survey.", *Nature*, 394:241, 1998.

[115] H. Flores et al., "15 Micron Infrared Space Observatory observations of the 1415+52 Canada-France Redshift Survey field: The cosmic star formation rate as derived from deep ultraviolet, optical, mid-infrared, and radio photometry", *Astrophys. J.*, 517:148, 1999.

[116] J. Gallego, J. Zamorano, A. Aragon-Salamanca, and M. Rego, "The current star formation rate of the local universe", *Astrophys. J.*, 455:L1, 1995.

[117] C. Gronwall. "The star formation rate density of the local universe from the KPNO International Spectroscopic Survey". In *After the Dark Ages: When Galaxies were Young (the Universe at* $2 < z < 5$*). 9th Annual October Astrophysics Conference in Maryland, College Park, 12-14 October 1998*, volume 470 of *American Institute of Physics Conference Proceedings*, page 335, 1999.

[118] L. Tresse and S. J. Maddox, "The H alpha luminosity function and star formation rate at z approximately 0.2", *Astrophys. J.*, 495:691, 1998.

[119] K. Glazebrook, C. Blake, F. Economou, S. Lilly, and M. Colless, "Measurement of the star formation rate from Hα in field galaxies at $z = 1$", *Mon. Not. Roy. Astron. Soc.*, 306:843, 1999.

[120] D. W. Hogg, "A meta-analysis of cosmic star-formation history", 2001, Submitted to PASP, astro-ph/0105280.

[121] I. K. Baldry et al., "The 2dF Galaxy Redshift Survey: Constraints on cosmic star formation history from the cosmic spectrum", *Astrophys. J.*, 569:582, 2002.

[122] F. Hammer et al., "Canada-France Redshift Survey. XIV. Spectral properties of field galaxies up to $z = 1$", *Astrophys. J.*, 481:49, 1997.

[123] D. W. Hogg, J. G. Cohen, R. Blandford, and M. A. Pahre, "The O II luminosity density of the universe", *Astrophys. J.*, 504:622, 1998.

[124] L. L. Cowie, A. Songaila, and A. J. Barger, "Evidence for a gradual decline in the universal rest-frame ultraviolet luminosity density for $z < 1$", *Astron. J.*, 118:603, 1999.

[125] B. Mobasher, L. Cram, A. Georgakakis, and A. Hopkins, "The 1.4-GHz and Hα luminosity functions and star formation rates from faint radio galaxies", *Mon. Not. Roy. Astron. Soc.*, 308:45, 1999.

[126] D. B. Haarsma, R. B. Partridge, R. A. Windhorst, and E. A. Richards, "Faint radio sources and star formation history", *Astrophys. J.*, 544:641, 2000.

[127] D. H. Jones and J. Bland-Hawthorn, "The Taurus Tunable Filter Field Galaxy Survey: Sample selection and narrowband number counts", *Astrophys. J.*, 550:593, 2001.

[128] K. M. Lanzetta, N. Yahata, S. Pascarelle, H. Chen, and A. Fernández-Soto, "The star formation rate intensity distribution function: Implications for the cosmic star formation rate history of the universe", *Astrophys. J.*, 570:492, 2002.

[129] K. Glazebrook et al., "The Sloan Digital Sky Survey: The cosmic spectrum and star formation history", *Astrophys. J.*, 587:55, 2003.

[130] I. K. Baldry and K. Glazebrook, "Constraints on a universal stellar initial mass function from ultraviolet to near-infrared galaxy luminosity densities", *Astrophys. J.*, 593:258, 2003.

[131] C. Chiosi, G. Bertelli, and A. Bressan, "New developments in understanding the HR diagram", *Annu. Rev. Astron. Astrophys.*, 30:235, 1992.

[132] K. Nomoto, "Evolution of 8-10 solar mass stars toward electron capture supernovae. I—Formation of electron-degenerate O+Ne+Mg cores", *Astrophys. J.*, 277:791, 1984.

[133] S. Ando, K. Sato, and T. Totani, "Detectability of the supernova relic neutrinos and neutrino oscillation", *Astropart. Phys.*, 18:307, 2003.

[134] A. G. Cocco, A. Ereditato, G. Fiorillo, G. Mangano, and V. Pettorino, "Supernova relic neutrinos in liquid argon detectors", *JCAP*, 12:2, 2004.

[135] Alessandro Strumia and Francesco Vissani, "Precise quasielastic neutrino nucleon cross section", *Phys. Lett.*, B564:42, 2003, astro-ph/0302055.

[136] C. Bemporad, G. Gratta, and P. Vogel, "Reactor-based neutrino oscillation experiments", *Rev. Mod. Phys.*, 74:297, 2002.

[137] E. Kolbe, K. Langanke, and P. Vogel, "Estimates of weak and electromagnetic nuclear decay signatures for neutrino reactions in Super-Kamiokande", *Phys. Rev.*, D66:013007, 2002.

[138] R. Tomas, D. Semikoz, G. G. Raffelt, M. Kachelriess, and A. S. Dighe, "Supernova pointing with low- and high-energy neutrino detectors", *Phys. Rev.*, D68:093013, 2003, hep-ph/0307050.

[139] A. Mirizzi, private communication.

[140] M. Shiozawa. "Hyper-Kamiokande project", talk at the International Workshop on a Next Generation Long-Baseline Neutrino Oscillation Experiment, Tsukuba, Japan, May 2001; http:/neutrino.kek.jp/jhfnu/workshop2/ohp.html.

[141] "Expression of Interest of the UNO Collaboration, 2004, http://ale.physics.sunysb.edu/uno/publications/EOI.pdf".

[142] L. Mosca. "Project of a Large International Underground Laboratory at Frejús", talk at Physics with a Multi-MW Proton Source, CERN, Geneva, May 25-27, 2004, http://physicsatmwatt.web.cern.ch/physicsatmwatt/Presentations/MW-Mosca.pdf.

[143] M. Fukugita and M. Kawasaki, "Constraints on the star formation rate from supernova relic neutrino observations", *Mon. Not. Roy. Astron. Soc.*, 340:L7, 2003.

[144] L. E. Strigari, J. F. Beacom, T. P. Walker, and P. Zhang, "The concordance cosmic star formation rate: Implications from and for the supernova neutrino and gamma ray backgrounds", 2005, astro-ph/0502150.

[145] G. Battistoni, A. Ferrari, P. Sala, and T. Montaruli, INFN FLUKA group, fluxes can be found at http://www.mi.infn.it/~battist/neutrino.html, low energy fluxes were added in 2004.

[146] T. K. Gaisser, T. Stanev, and G. Barr, "Cosmic-ray neutrinos in the atmosphere", *Phys. Rev.*, 1988.

[147] G. Barr, T. K. Gaisser, and T. Stanev, "Flux of atmospheric neutrinos", *Phys. Rev.*, 1989.

[148] M. Honda, T. Kajita, K. Kasahara, and S. Midorikawa, "Calculation of the flux of atmospheric neutrinos", *Phys. Rev.*, 1995.

[149] M. Vagins and M. Malek, private correspondence.

[150] P. Vogel and J. Engel, "Neutrino electromagnetic form-factors", *Phys. Rev.*, D39:3378, 1989.

[151] O. Tengblad, K. Aleklett, R. von Dincklage, E. Lund, G. Nyman, and G. Rudstam, "Integral $\bar{\nu}$-spectra derived from experimental β-spectra of individual fission products", *Nuclear Physics A*, 503:136, 1989.

[152] P. Huber and T. Schwetz, "Precision spectroscopy with reactor antineutrinos", *Phys. Rev.*, D70:053011, 2004.

[153] L. Michel, "Weak interactions between "old" particles and beta decay", *Rev. Mod. Phys.*, 29:223, 1957.

[154] S. Fukuda et al., "Solar B-8 and hep neutrino measurements from 1258 days of Super-Kamiokande data", *Phys. Rev. Lett.*, 86:5651, 2001, hep-ex/0103032.

[155] K. S. Hirata et al., "Observation of B-8 solar neutrinos in the Kamiokande-II detector", *Phys. Rev. Lett.*, 63:16, 1989.

[156] D. Schiminovich et al., "The GALEX-VVDS measurement of the evolution of the far-ultraviolet luminosity density and the cosmic star formation rate", *Astrophys. J.*, 619:L47, 2005.

[157] D. Christopher Martin et al., "The Galaxy Evolution Explorer: A space ultraviolet survey mission", *Astrophys. J.*, 619, 2005.

[158] I. Goldman, Y. Aharonov, G. Alexander, and S. Nussinov, "Implications of the supernova SN 1987A neutrino signals", *Phys. Rev. Lett.*, 60:181789, 1988.

[159] D. Nötzold, “New bounds on neutrino magnetic moments from stellar collapse”, *Phys. Rev.*, 38:61658, 1988.

[160] J. Lattimer and J. Cooperstein, “Limits on neutrino magnetic moment from SN 1987A”, *Phys. Rev. Lett.*, 61:123, 1988.

[161] R. Barbieri and R. N. Mohapatra, “Limit on the magnetic moment of the neutrino from supernova 1987A observations”, *Phys. Rev. Lett.*, 61:127, 1988.

Danksagung

Ganz besonders möchte ich Georg Raffelt für die hervorragende Betreuung der Diplomarbeit danken. Obwohl durch viele Verpflichtungen gebunden, war seine Tür immer offen und er immer zu Diskussionen bereit. Vor allen Dingen in der Endphase tat er alles Mögliche um der Arbeit zu einem guten Abschluss zu verhelfen.

Bei Michael Altmann, Alessandro Mirizzi, Pasquale Serpico, Fabio Iocco und Michael Kachelrieß möchte ich mich für wichtige Diskussion über Neutrino- und Astrophysik bedanken. Bei Michael Schmidt, Federico Buersgens, Pasquale Serpico und Jessica Nipp möchte ich mich für das Korrekturlesen bedanken. Ferner möchte ich mich bei Michael Rauch, Christoph Reißer, Thomas Fritzsche und Thomas Hahn für Hilfe bei Software- und Hardwareproblemen bedanken. Mein Dank gilt ebenfalls meinen Zimmergenossen Cailin Farrell, Maximilian Stahlhofen, Martin Fürst, Michael Fickinger, Jurgis Pasukonis, Philip Brandt und Jo Bovy für die gute Arbeitsatmosphäre in unserem vollen Raum. Sie trugen dazu bei, dass es auch in einem Zimmer mit sechs Leuten (und sechs Rechnern) möglich war zu arbeiten, ohne einen Nervenzusammenbruch zu erleiden. Der ganzen Theorie-Gruppe des MPI danke ich für die gute Atmosphäre, besonders der TribüHne-Gruppe beim Mittagessen und den üblichen Verdächtigen beim Kaffeetrinken. Dem Fußball-Team und dem Beachvolleyball-Team des MPI möchte ich für sportliche Betätigung in der Arbeitszeit danken. Heidi Rzehak möchte ich für die engagierte Organisation des Doktoranden- und Diplomandenkolloquiums danken.

Schlussendlich möchte ich meiner Familie und meinen Eltern danken, die mich immer und in jeglicher Hinsicht unterstützt haben.